Downloaded from orbit.dtu.dk on: May 05, 2023

DTU Library

Quantum information processing with mesoscopic photonic states

Madsen, Lars Skovgaard

Publication date:
2012

Document Version
Publisher's PDF, also known as Version of record

Link back to DTU Orbit

Citation (APA):
Madsen, L. S. (2012). *Quantum information processing with mesoscopic photonic states*. Technical University of Denmark.

General rights
Copyright and moral rights for the publications made accessible in the public portal are retained by the authors and/or other copyright owners and it is a condition of accessing publications that users recognise and abide by the legal requirements associated with these rights.

- Users may download and print one copy of any publication from the public portal for the purpose of private study or research.
- You may not further distribute the material or use it for any profit-making activity or commercial gain
- You may freely distribute the URL identifying the publication in the public portal

If you believe that this document breaches copyright please contact us providing details, and we will remove access to the work immediately and investigate your claim.

Quantum information processing with mesoscopic photonic states

Lars Skovgaard Madsen

A thesis submitted for the degree
Doctor of Philosophy in Physics

Supervisor
Professor Ulrik L. Andersen
Quantum Information group
Department of Physics
Technical University of Denmark
July 2012

Acknowledgments

First I would like to thank the members of the QUIN group at the DTU for the (ongoing) discussions, cakes and company. In particular I would like to thank both the old and the new group members who I have worked closely with, who have helped me with advise, cheers and discussions.

A thank you to the external researchers that I have had the pleasure of collaborating with Vladislav Usenko, Radim Filip and Christian Müller.

A thank you to our secretary Dorte Glass without whom not much work would be done.

A special thanks to my supervisor Ulrik L. Andersen for giving me the opportunity to work at the front edge of research. For the advise, encouragement, discussion and freedom to explore quantum optics and information.

Finally I would like to thank my friends and family for their support and love.

Resumé

I kvantemekanikken gælder andre spilleregler end vi kender fra vores klassiske hverdag. Disse spilleregler kommer både i form af nye muligheder og nye begrænsninger. Begrænsningerne bunder primært i Heisenbergs ubestemthedsrelation der siger at det ikke er muligt samtidigt at måle to konjugerede variable som fx fasen og amplituden af et lys-felt, uden at tilføje støj. Mulighederne er oftest forbundene med kvanternes evne til at være i superpositioner af tilstande. Disse to grundlæggende egenskaber ændrer måden vi kan måle, kommunikere og processerer information på.

I denne afhandling bruger vi laserlys (1064 nm) som bærer for kvantetilstande. Selve tilstandene ligger på et sidebånd nogle få megahertz fra bærer frekvensen. Laserlys har mange fordele der gør det ideelt til at undersøge kvantefænomener. Først og fremmest kan alt gøres ved stuetemperatur, fordi laserens frekvens er meget højere end frekvenserne af den termiske baggrundstråling. Tilstande kan genereres og omformes med linear optik og de kan måles med høj effektivitet og lav støj.

I afhandlingen støder vi på et nyt mål for kvantekorrelationer kaldet kvanteuoverensstemmelse (Quantum discord). Målet kvantificere hvor meget information der går tabt ved måling af en del af en kvantetilstand både hvis tilstandene er kvante-sammenfiltrede og hvis de er separable. Vi har lavet et af de første eksperimenter der viser hvordan dette tab af information afhænger af tilstandene og hvordan det udvikler sig ved disspation. Vi viser bl.a. at kvanteuoverensstemmelsen kan skabes med klassiske korrelationer og at den kan vokse ved lokale operationer.

Vi har lavet et forsøg med kvantenøgledeling (Quantum key distribution). Vi har i samarbejde med teoretikere fra Olomouc udviklet en avanceret kvantenøgle protokol som benytter sig af kvante-sammenfiltring til garantere sikker kommunikation over større afstande. Vi viser at den grundlæggende ressource er kvante-sammenpresning (eng. squeezing) og vi viser at vi kan gøre det bedre end nogen tilsvarende protokol som ikke benytter kvante-sammenpresning.

Polarisation bliver brugt i bred udstrækning til at manipulere kvantetilstande. Tilgæld er definitionerne af polarisationen for kvantetilstande mangelfulde, både begrund af at kvantetilstande ikke har et veldefineret foton tal og fordi kvantetilstande ofte er kendetegnet ved der varians mere end deres middelværdi. Vi har taget del i illustrationen af et nyt mål der inkluderer variansen i et polarisations mål. Derefter har vi udviklet to nye mål der opløser polarisationen for hvert foton antal, et mål for middelværdien og et mål for variansen. Med disse i bagagen undersøger vi polarisationen i regimet mellem enkelt foton tilstande og tilstande med en klassisk komponent og finder bl.a. tilstande med skjult polarisation.

List of Puplications

Articles

I Mikael Lassen, Lars S. Madsen, Metin Sabuncu, Radim Filip and Ulrik L. Andersen. Experimental demonstration of squeezed-state quantum averaging. Phys. Rev. A 82, 021801 (2010)

II A. B. Klimov, G. Bjork, J. Soderholm, L. S. Madsen, M. Lassen, U. L. Andersen, J. Heersink, R. Dong, Ch. Marquardt, G. Leuchs, L. L. Sanchez-Soto. Assessing the Polarization of a Quantum Field from Stokes Fluctuation. Phys. Rev. Lett. 105, 153602 (2010)

III Lars S. Madsen, Adriano Berni, Mikael Lassen and Ulrik L. Andersen. Experimental Investigation of the Evolution of Gaussian Quantum Discord in an Open System. Phys. Rev. Lett. 109, 030402 (2012)

IV Lars S. Madsen, Vladyslav C. Usenko, Mikael Lassen, Radim Filip and Ulrik L. Andersen. Continuous variable quantum key distribution with two-mode squeezed states. Submitted to Nat. Commun., arXiv:1110.5522

V Christian Kothe, Lars S. Madsen, Ulrik L. Andersen, Gunnar Björk. Experimental determination of the degree of quantum polarisation of continuous variable states., Submitted to Phys. Rev. Lett., arXiv:1207.6366

Posters

I Quantum Averaging. Mikael Lassen, Lars Skovgaard Madsen, Metin Sabuncu, Radim Filip and Ulrik L. Andersen. Continuous variable workshop, Herrsching and QNLO Summer school.

II Experimental characterization of Gaussian quantum discord. Lars S. Madsen, Adriano Berni, Mikael Lassen and Ulrik L. Andersen. CVQIP'12 and QCMC 2012.

III Continuous variable quantum key distribution with coherently modulated entangled states. Lars S. Madsen, Vladyslav C. Usenko, Mikael Lassen, Radim Filip and Ulrik L. Andersen. QCMC 2012.

List of Projects

Apart from the projects mentioned in articles there are:

I Sensing the vibrations of a micro-toroid with squeezed light. Ulrich B. Hoff, Hugo Kerdoncuff, Mikael Lassen, Lars S. Madsen and Ulrik L. Andersen. Status: Experiment under development, first measurements completed.

II Passive phase estimation with squeezed states. Emanuele Distante, Miroslav Jezek, Christian Kothe, Lars S. Madsen and Ulrik L. Andersen. Status: Experiment completed. Data analysis in progress.

III Adaptive phase estimation with squeezed states. Mario A. Usuga Castaneda, Bo Melholt Nielsen, Lars S. Madsen, Mikael Lassen and Ulrik L. Andersen. Status: Experiments running.

IV Quantum Error Code Correction for Protecting Continuous-Variable Quantum States in a Noisy non-Markovian Environment. Mikael Lassen, Lars S. Madsen, Radim Filip and Ulrik L. Andersen. Status: Draft close to submission.

V Reconciliation robust quantum key distribution with squeezed states. Vladislav C. Usenko, Lars S. Madsen, Ulrik L. Andersen and Radim Filip. Status: First experiments completed. Data analysis in progress.

VI Hidden polarization and the quantum transition from discrete to continuous variable polarization states. Lars S. Madsen, Christian R. Müller and Ulrik L. Andersen. Draft in progress.

Contents

1 Introduction **3**
- 1.0.1 Motivation . . . 4
- 1.0.2 Overview . . . 4

2 Introduction to quantum optics **7**
- 2.0.3 State representation . . . 8
- 2.0.4 Single mode operations . . . 9
- 2.0.5 Two-mode operations . . . 10
- 2.0.6 The thermal state and irreversible operations . . . 12
- 2.0.7 The covariance matrix and the symplectic formalism . . . 12
- 2.0.8 Detection . . . 13
- 2.0.9 Transformations between the different representations . . . 15

2.1 Introduction to quantum information theory . . . 17
- 2.1.1 Entropy and information . . . 17
- 2.1.2 Quantum information of Gaussian states . . . 19
- 2.1.3 Entanglement measures . . . 20

2.2 Introduction to the experiments . . . 21
- 2.2.1 Mode matching . . . 21
- 2.2.2 Locks . . . 22
- 2.2.3 Cavities . . . 23
- 2.2.4 Displacements and mixtures of coherent states . . . 24
- 2.2.5 Optical parametric amplifiers . . . 25
- 2.2.6 Detection . . . 27
- 2.2.7 Single mode states . . . 28
- 2.2.8 Two mode states . . . 30

3 Gaussian quantum discord **33**

3.1 Introduction . . . 33

3.2 Theory of the Gaussian discord . . . 34

3.3 Experimental characterization . . . 35
- 3.3.1 Entangled states . . . 35
- 3.3.2 Mixtures of coherent states . . . 36

3.4 Simulations of Gaussian discord . . . 39
- 3.4.1 The robustness of discord . . . 39
- 3.4.2 The reverse discord . . . 40
- 3.4.3 Phase conjugation . . . 40
- 3.4.4 Modulated EPR states . . . 41
- 3.4.5 Single-mode squeezing . . . 42

3.5 Summary and outlook 42

4 Quantum key distribution **45**
4.1 CV-QKD with modulated entangled states 46
4.1.1 Secret Key 47
4.1.2 Theoretical results 48
4.1.3 Experimental setup 50
4.1.4 Data analysis and results 50
4.1.5 Discussion 52
4.2 β robust protocol 54
4.2.1 Experiment 55
4.2.2 Data analysis 56
4.2.3 Results 56
4.2.4 Further analysis 56
4.3 Concluding remarks 57
4.3.1 Measures in QKD 57
4.3.2 Summary 58
4.3.3 Outlook 58

5 Quantum polarization **61**
5.1 Introduction 61
5.1.1 Poincaré sphere 62
5.1.2 The unpolarized states and $\mathbb{P}_1^{\mathrm{sc}}$ 62
5.1.3 An alternative measuring strategy 63
5.2 Defining and illustrating $\mathbb{P}_1^{\mathrm{res}}$ 63
5.2.1 Theoretical investigation of $\mathbb{P}_1^{\mathrm{res}}$ 64
5.2.2 Experimental investigation of $\mathbb{P}_1^{\mathrm{res}}$ 66
5.3 Defining and illustrating $\mathbb{P}_2$ 68
5.3.1 First experiment for $\mathbb{P}_2$ 69
5.4 Defining and illustrating $\mathbb{P}_2^{\mathrm{res}}$ 69
5.4.1 Comparison of the $\mathbb{P}$'s 70
5.4.2 Hidden polarization 71
5.4.3 SU_2 Wigner functions 72

6 Concluding remarks **79**
6.1 Summary 79
6.2 Outlook 80

Chapter 1

Introduction

Quantum states obey a different set of rules than we are used to in our macroscopic world. These rules come both with possibilities and restrictions. The first restriction is the impossibility of perfectly extracting two conjugate observables such as both the amplitude and the phase of a light field simultaneously. It is formulated in Heisenberg's uncertainty principle, stating that the product of the uncertainties is greater than or equal to $\hbar$. The possibilities are most often rooted in the quantum state's ability to be in superpositions of eigenstates. The superpositions can be between physically separated states which entangle them so that they contain more information about each other than classically possible. However, if kept separate the Heisenberg's uncertainty principle limits the extractable information. Bringing them togther these superpositions allow us to squeeze the uncertainty of one observable below the limit set by the minimal symmetric uncertainty allowed by the Heisenberg's uncertainty principle and thereby measure more precisely than otherwise possible. This comes at the expense of antisqueezing the conjugate observable so the state still fulfill the Heisenberg's uncertainty principle. These quantum phenomena lead to fundamental differences in the measurements, communication protocols and information processing which can be performed using quantum states.

The research field of quantum optics is one of the most developed when it comes to observing quantum phenomena. The light produced by lasers can have outstanding properties when it comes to generating simple quantum states of light. Laser light is coherent, meaning that it stays in phase with itself, for several kilometers. The light travels with minimal loss through air and high quality optics makes it possible to steer and reshape the quantum modes. The most important state of a quantum system is the ground or vacuum state. For light near the visible wavelengths the ground state is the natural state at room temperatures. This state is so important because it serves as the initial state when preparing a quantum state. Linear optics makes it possible to displace, rotate and couple the quantum states. Low loss non-linear interaction allows for the generation of exotic squeezed and entangled states. Finally the generated states can be measured and characterized with high efficiency and low electronic and thermal noise.

The research field is divided between two formalisms depending on the type of measurements employed. When measuring on the light with photon counting detectors the discrete photon numbers are observed giving a discrete variable

formalism. When measuring with homodyne detectors where the faint quantum state beats with a strong local oscillator the continuous phase and amplitude quadratures are observed giving a continuous variable formalism. Each formalism have their advantages and disadvantages which can be roughly summarized as the discrete variables working perfectly but conditionally, while the continuous variables work every time but imperfect. We will focus on the continuous variables in this thesis.

To utilize squeezing and entanglement to surpass the classical boundaries is a challenging task, partly due to their fragile nature where loss and noise quickly degenerates the states and partly due to the challenge of extracting the information. Entangled states have been used as a resource for teleportation, dense coding, cryptography and several other quantum information protocols, for reviews see for example refs. [1–3]. In teleportation a quantum state is physically transferred to a distant ancilla state through a classical channel, using preestablished entanglement, local operations and classical information. Dense coding uses preestablished entanglement to double the classical information capacity of a quantum channel. We will return to the topic of quantum cryptography and how entanglement and squeezing can be used at a later stage.

1.0.1 Motivation

For me the prime motivation for working with quantum optics is the ability to explore quantum mechanics in a table-top experiment. It is possible for a few persons to get a nice idea, make simulations and perform the experiment, thereby taking part in the whole process. At the same time the ideas developed and the results gained have the potential of making a real impact on how quantum mechanics is applied in future technology.

1.0.2 Overview

In this thesis we will see quantum information protocols, quantum meteorology as well as fundamental studies of quantum phenomena. The various topics are connected by the experimental methods employed.

The thesis is built up as follows:

- In chapter 2 we will start with an intro to quantum optics theory, the covariance matrix formalism and the theory of quantum information. Then we will go through an intro to the experimental methods we use to observe these phenomena.
- In chapter 3 we will dive into the fundamentals of quantum correlations and information by applying a new measure 'Gaussian quantum discord' to various states. The measure quantifies the loss of information when measuring part of quantum state thereby revealing quantum inference in a more general form than the measures of entanglement.
- In chapter 4 we show how the limitations in quantum mechanics can be turned to our advantage. The rules of extractable information can be used to restrict an eavesdropper. We will demonstrate how 'quantum key distribution' can be improved by using squeezing and entanglement combined with coherent modulation.

- Chapter 5 is on the topic of quantum polarization. Polarization is well known in the classic world and is highly used in quantum optics to perform single- and two-mode rotations. Even though the polarization rotations work well on quantum states, it is non-trivial to quantify how polarized a state is. We shall see several attempts to improve our definitions of quantum polarization. Further we will look at quantum effects leading to hidden polarization and study the transition between quantum and classic polarization.
- Finally we will conclude the thesis in chapter 6.

Chapter 2

Introduction to quantum optics

The electromagnetic field can be quantized as a harmonic oscillator (see e.g. [4, 5]). We will express the properties of a single quantum mode of the light field using the bosonic annihilation $\hat{a}$ and creation $\hat{a}^\dagger$ operators also known as the ladder operators. They have the commutation relation

$$\left[\hat{a}, \hat{a}^\dagger\right] = 1 \tag{2.1}$$

where $\hat{}$ symbolize that we are dealing with operators. We will set Plancks constant $\hbar = 2$ which corresponds to setting the variance of vacuum to one and thereby counting everything in shot-noise units [1, 6]. The eigenstates are the coherent states $\hat{a}|\alpha\rangle = \alpha|\alpha\rangle$ where α is a complex number. These operators are not hermitian and hence cannot be measured directly. We can however make hermitian combinations that can be measured. We define the amplitude and the phase quadrature operators from the addition as

$$\begin{aligned} \hat{x} &= \hat{a}^\dagger + \hat{a} \\ \hat{p} &= i\left(\hat{a}^\dagger - \hat{a}\right) \end{aligned} \tag{2.2}$$

and in general

$$\hat{q}(\theta) = \hat{a}^\dagger e^{i\theta} + \hat{a}e^{-i\theta}. \tag{2.3}$$

The operators $\hat{x}$ and $\hat{p}$ are called the canonical quadrature operators because they have the same commutation relation as the position and momentum operators of a particle namely

$$[\hat{x}, \hat{p}] = 2i. \tag{2.4}$$

With a commutation relation for two observables also comes a Heisenberg's uncertainty relation (see e.g [7] §1.4). For $\hat{x}$ and $\hat{p}$ this relation states that

$$\mathrm{var}(\hat{x})\mathrm{var}(\hat{p}) \geq 1 \tag{2.5}$$

where var is the variance calculated as $\langle\hat{o}^2\rangle - \langle\hat{o}\rangle^2$ and $\langle\hat{o}\rangle$ is the expectation value of $\hat{o}$. This uncertainty relation means that if we by some means measure

or squeeze one quadrature so that the variance is reduced, then we must at the same time increase the variance of the conjugate quadrature. The eigenstates of the quadrature operators are the infinitely squeezed states $\hat{q}|q\rangle = q|q\rangle$ meaning they have zero variance in the respective quadrature. At first these states look very interesting, however they are somewhat unphysical as they also have infinite anti-squeezing and correspondingly infinite energy.

Rather than summing the ladder operators we can also take the product, obtaining the number operator

$$\hat{n} = \hat{a}^\dagger \hat{a}. \tag{2.6}$$

The eigenstates $\hat{n}|n\rangle = n|n\rangle$ are called the Fock-states. As the quadrature eigenstates these states are infinitely squeezed. However unlike quadrature eigenstates the anti-squeezing is in the phase, that is, the phase is completely undefined. The Fock states are orthogonal and complete like the infinitely squeezed states. They are countable which simply means that you can count them as 1,2,3,... in contrast to $|q\rangle$ which are continuous. These properties make the Fock states a common choice for spanning the Hilbert space of the quantum modes.

2.0.3 State representation

All the states that we have considered so far have the property that they can be written as a single vector $|\psi\rangle$. If we consider an ensemble described by a statistical mixture of states this is no longer possible. Instead mixed states can be expressed with density operators. Such an operator can in turn be written in terms of the Fock states

$$\hat{\rho} = \sum_{n,m=0}^{\infty} |n\rangle\langle n|\hat{\rho}|m\rangle\langle m| = \sum_{n,m=0}^{\infty} \rho_{mn}|m\rangle\langle n|, \tag{2.7}$$

where the (complex) numbers ρ_{mn} form the density matrix ρ in the Fock basis. Knowing the density operator we can calculate expectation of values any operator as

$$\langle\hat{o}\rangle = \text{trace}(\hat{\rho}\hat{o}). \tag{2.8}$$

One special expectation value is that of the density operator itself, $\gamma = \text{trace}(\rho^2)$. It is known as the purity and the state is said to be pure if $\rho^2 = \rho$ ($\gamma = 1$) and mixed otherwise.

Alternatively we can express a state in phase space in terms of the quasi-probability distribution called the Wigner function. The prefix "quasi" originates from the fact that Wigner functions can be negative unlike classical probability distributions. The marginal distributions of the Wigner function gives the classic probability distributions of the quadratures and there is a one to one correspondence between the Wigner function and the density matrix (see Sec. 2.0.9). For these reasons the Wigner function is often used to illustrate states.

The states which have Gaussian Wigner functions are called the Gaussian states. These states can be described in a particularly simple and useful way using the covariance matrix formalism [1, 6]. The Gaussian states are fully described by their mean value and their covariance matrix σ. Hence instead of using the infinite dimensional Hilbert space we are left with 5 real parameters,

namely the mean and the variance of $\hat{x}$ and of $\hat{p}$ and the covariance between $\hat{x}$ and $\hat{p}$. Note that since we have chosen $\hbar = 2$ the covariance matrices corresponding to the vacuum state will be the identity matrix.

2.0.4 Single mode operations

In general, a unitary operator $\hat{U}$ transforms the density operator $\hat{\rho}$ to a new density operator $\hat{\rho}'$ according to

$$\rho' = \hat{U}\hat{\rho}\hat{U}^{\dagger}. \tag{2.9}$$

We have already encountered the coherent states as the eigenstates of the ladder operators. The unitary operator which creates these states is called the displacement operator and is given by

$$\hat{D}(\alpha) = \mathrm{e}^{\alpha\hat{a}^{\dagger} - \alpha^{*}\hat{a}}. \tag{2.10}$$

Operating on the vacuum state we get

$$\hat{D}(\alpha)|0\rangle = e^{-\frac{1}{2}|\alpha|^2} \sum_{n=0}^{\infty} \frac{\alpha}{\sqrt{n!}}|n\rangle = |\alpha\rangle. \tag{2.11}$$

The mean value of $\hat{x}$ and $\hat{p}$ gives the real and complex part of α while the variance stays the same as for the vacuum state. Hence we consider the coherent states as displaced vacuum states.

Finitely squeezed states can be generated from vacuum using the quadrature squeezing operator. This unitary operator is defined as

$$\hat{S}(z) = \mathrm{e}^{\frac{1}{2}(z^{*}\hat{a}^{2} - z\hat{a}^{\dagger 2})}, \tag{2.12}$$

where $z = re^{i2\theta}$, r is the squeezing parameter and $\theta \in [0; \pi[$ is the squeezing phase. We see that the ladder operators are squared which signify that the operator is non-linear. Operating on a vacuum state we get

$$\hat{S}(z)|0\rangle = \frac{1}{\sqrt{\cosh(z)}} \sum_{n=0}^{\infty} \frac{\sqrt{(2n)!}\tanh(z^n)}{2^n n!}|2n\rangle, \tag{2.13}$$

from which we see that only every second photon number is excited. The variance has changed so that

$$\mathrm{var}\left(\hat{q}(\theta)\right) = \mathrm{e}^{-2r} \tag{2.14}$$

while

$$\mathrm{var}\left(\hat{q}(\theta + \frac{\pi}{2})\right) = \mathrm{e}^{2r}. \tag{2.15}$$

From the variances we see that the distribution of the noise has been shifted from one quadrature to the other. However the uncertainty relation between the conjugate quadratures is conserved. We note that the squeezing operator does not commute with the displacement operator.

Finally we can also rotate the states in phase-space with the operator

$$\hat{R}(\theta) = e^{-i\theta\hat{n}}, \tag{2.16}$$

which simply changes the phase of the state.

In the covariance formalism we can express the displacement as a vector

$$\hat{D} = \begin{pmatrix} d_1 \\ d_2 \end{pmatrix}, \tag{2.17}$$

the rotation as a rotation matrix

$$\hat{R}(\theta) = \begin{pmatrix} \cos(\theta) & \sin\theta \\ -\sin\theta & \cos(\theta) \end{pmatrix} \tag{2.18}$$

and the amplitude squeezing as

$$\hat{S}(r) = \begin{pmatrix} e^{-r} & 0 \\ 0 & e^{r} \end{pmatrix}. \tag{2.19}$$

Writing the quadratures as a vector, $\hat{\mathbf{x}}$, the displacement only changes the mean value by simple addition. In a general unitary transformation the mean value changes as

$$\hat{\mathbf{x}}' = \hat{R}(\phi)\hat{S}(r)\hat{R}(\theta)\hat{\mathbf{x}} + \hat{D}, \tag{2.20}$$

and the covariance matrix changes as

$$\hat{\sigma}' = \hat{R}(\phi)\hat{S}(r)\hat{R}(\theta)\hat{\sigma}\left(\hat{R}(\phi)\hat{S}(r)\hat{R}(\theta)\right)^T. \tag{2.21}$$

All single mode Gaussian unitary operations can be decomposed into rotations, displacement and squeezing.

2.0.5 Two-mode operations

All the operations we have considered so far have been single mode operations. A beamsplitter couples two modes together and can be considered as a two-mode rotation. The classic beamsplitter splits a single beam into two modes. In quantum mechanics all modes have to be considered so we have to include the vacuum entering the beamsplitter. Given input modes $\hat{a}$ and $\hat{b}$, the phase free beamsplitter can be described by a unitary operator

$$\hat{U}_{bs}(\theta) = e^{\theta(\hat{a}^\dagger\hat{b} - \hat{a}\hat{b}^\dagger)} \tag{2.22}$$

where $\theta = \cos^{-1}(\sqrt{\mathrm{T}})$ and T is the transmission. θ is used to stress that the beamsplitter operation can be considered as a two-mode rotation. Two-mode rotations can also be performed with the polarization rotations. The Stokes operators are used to describe these. We define them in the horizontal-vertical basis as

$$\begin{aligned} \hat{S}_0 &= \hat{a}_H^\dagger\hat{a}_H + \hat{a}_V^\dagger\hat{a}_V \quad & \hat{S}_1 &= \hat{a}_H^\dagger\hat{a}_H - \hat{a}_V^\dagger\hat{a}_V \\ \hat{S}_2 &= \hat{a}_H^\dagger\hat{a}_V + \hat{a}_V^\dagger\hat{a}_H \quad & \hat{S}_3 &= i(\hat{a}_V^\dagger\hat{a}_H - \hat{a}_H^\dagger\hat{a}_V), \end{aligned}$$

where $\hat{S}_0$ is the total number of photons, $\hat{S}_1, \hat{S}_2, \hat{S}_3$ are the difference between the horizontally and vertically polarized photons, the difference between the 45°

and $-45°$ polarized photons and the difference between left-hand and right-hand circularly polarized photons, respectively. [1]

All the Stokes operators commute with $\hat{S}_0$, while the others fulfill the commutation relation

$$\left[\hat{S}_1, \hat{S}_2\right] = 2i\hat{S}_3 \tag{2.23}$$

and cyclic permutations hereof.

The polarization rotations are then given by

$$\hat{U}_{pol}(\hat{S}_i, \theta) = e^{i\theta\hat{S}_i}, \quad i \in \{0, 1, 2, 3\}. \tag{2.24}$$

The $\hat{U}_{pol}(\hat{S}_0)$ gives a global phase rotations while $\hat{U}_{pol}(\hat{S}_1), \hat{U}_{pol}(\hat{S}_2), \hat{U}_{pol}(\hat{S}_3)$ corresponds to beamsplitter rotations with phase rotations between the two modes. Using these operators together with polarization beamsplitters allow the construction of beamsplitters with arbitrary phase.

These operators work on two-mode states. A two-mode state can be represented by a two-mode density operator by taking the Kronecker product $\bigotimes$ of two single mode density operators. The $\bigotimes$ is often hidden to ease the reading and rather the involved modes are specified e.g in the expression for $\hat{S}_1$ it should say $\hat{a}_H^\dagger \hat{a}_H \bigotimes \mathbb{I}_V - \mathbb{I}_H \bigotimes \hat{a}_V^\dagger \hat{a}_V$, instead we have used H and V to symbolize the different quantum modes. If using the covariance matrix formalism the modes are added with the direct sum $\bigoplus$.

In itself turning two single-mode matrices into a two-mode matrix does not change the single mode states. We can still perform single mode operations by taking the product of of the single-mode operator with the identity. However once we perform a two-mode rotation the states might not be separable any more. That means that we can no longer write the two-mode state as a product of two single-mode states and the state is said to be entangled. The simplest example of such a state is a single photon and vacuum state mixed on a 50/50 beamsplitter. For this state each of the single mode states will be a mixture of vacuum and a single photon. However the two-mode state is not a mixed state, rather it is a superposition of the photon being in the one mode and in the other.

In this thesis the resource for generating entanglement is to couple two single mode squeezed states with a $\frac{\pi}{2}$ phase shift on a 50/50 beamsplitter. This state resembles the state first imagined by Einstein, Podolsky and Rosen in their famous objection to quantum mechanics and hence it is often called an EPR-state [8]. The state is characterized by each single mode being a thermal state, while the two-mode state is pure. If the two modes are allowed to interfere again on a 50/50 beamsplitter the two squeezed states reappear.

The two-mode squeezing operator which generates entanglement between two modes can be written as

$$\hat{S}_2(r) = e^{\frac{r}{2}(\hat{a}\hat{b} - \hat{a}^\dagger\hat{b}^\dagger)}. \tag{2.25}$$

The operation resembles that of a beamsplitter, but, like the single mode squeezing operation, it does not conserve the photon number. We note that this two-

[1] We note that there are some disagreements in literature as to which operator should be S_1/S_x, we choose the difference between the horizontal and the vertical modes, but sometimes the difference between the diagonal and the anti-diagonal is chosen. As long as the cyclic order of the operators is preserved it is just rotation.

mode squeezing operation can be realized by squeezing both modes, rotating one of them by $\frac{\pi}{2}$ and then coupling them on a beamsplitter.

2.0.6 The thermal state and irreversible operations

Both the coherent and the squeezed states considered so far have been pure. The simplest mixed state is called a thermal state. The density matrix is characterized by a Lorentzian distribution of photons on the diagonal and there are no coherences between the different photon numbers. For a state with N_{th} thermal photons we can write the non-zero elements of density matrix as

$$\rho_{n,n}(N_{th}) = \frac{1}{1+N_{th}} \left(\frac{N_{th}}{1+N_{th}} \right)^n \tag{2.26}$$

and represented in the covariance formalism, the mean is zero and the covariance matrix is

$$\sigma(N_{th}) = \begin{bmatrix} 1+2N_{th} & 0 \\ 0 & 1+2N_{th} \end{bmatrix}. \tag{2.27}$$

Together with the squeezing, rotation and displacement operators the thermal state makes it possible to simulate any single mode Gaussian state.

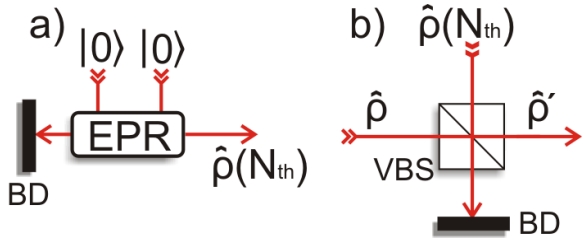

Figure 2.1: a) Model for generation of a thermal state. The partial trace is symbolized with the beam dump, BD. b) Model for thermal lossy channel with a variable beamsplitter (VBS).

The thermal state can be generated by making a Gaussian mixture of coherent states or by tracing out one mode of an EPR-state as shown in Fig. 2.1 a). The second method has the advantage that it accounts for all modes, but it requires the partial trace. Given the two modes A and B and their two-mode density matrix ρ_{AB} we write

$$\rho_A = \text{trace}_B(\rho_{AB}), \tag{2.28}$$

where trace_B works as the identity on system A, but traces out system B and all correlations between the two systems. Using this trace we can model irreversible loss and noise addition by coupling the state to a vacuum state or a thermal state on a variable beamsplitter as shown on Fig. 2.1 b).

2.0.7 The covariance matrix and the symplectic formalism

We have already seen how Gaussian states can be represented with covariance matrices and mean values and how these transform. These operations can be

represented in a compact formalism [1,9]. For a N mode state we have the $2N$ mean values in a vector $\hat{\mathbf{x}}$ and the $2N \times 2N$ covariance matrix σ. The Heisenberg uncertainty principle is formulated as

$$\sigma + \Omega \geq 0, \tag{2.29}$$

where Ω is the symplectic form

$$\Omega = \bigoplus_{1}^{N} \omega, \quad \omega = \begin{pmatrix} 0 & 1 \\ -1 & 0 \end{pmatrix}. \tag{2.30}$$

The transformations Eq. 2.20 and Eq. 2.21 are straightforwardly generalized to work on one of the N modes and the two-mode rotations can also be applied to two of the N modes.

2.0.8 Detection

In quantum mechanics the type of measurement is as important as the states measured. There can be several types of detectors that approximate the same hermitian operator. In general, a measurement with the outcome m on one mode of a multi-mode density matrix can be formulated as [10] (§2.4.2)

$$\rho_m = \frac{\hat{M}_m^\dagger \rho \hat{M}_m}{\text{trace}(\hat{M}_m^\dagger \hat{M}_m \rho)}. \tag{2.31}$$

Here we have written the measurement as operators. The most general class of measurement operators are the positive operator-valued measure (POVM). They are required to fulfill the completeness relation $\sum_m \hat{E}_m = 1$, where $\hat{E}_m = \hat{M}_m^\dagger \hat{M}_m$. If furthermore $\hat{M}_m^2 = \hat{M}_m$ the measurements are said to be projective. In terms of Eq. 2.31 subsequent measurement with a projective operator is seen to give the same result, which is not the case if $\hat{M}_m^2 \neq \hat{M}_m$. In this sense the relation between projective measurements and POVMs is like the relation between pure states and the density matrix.

The most important detector in this thesis is the homodyne detector.

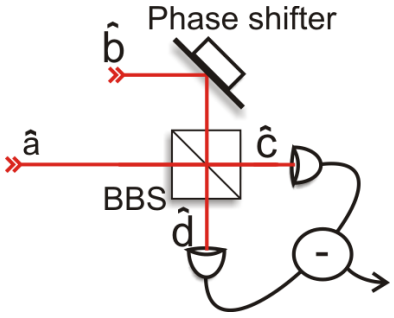

Figure 2.2: Theoretical homodyne detector. BBS balanced beam splitter (50/50).

Imagine that two light fields described by the lowering operators $\hat{a}$ and $\hat{b}$ impinge on a balanced beamsplitter, see Fig. 2.2. Naming the modes clockwise

we can describe the output fields with lowering operators $\hat{c}$ and $\hat{d}$. The output modes of the beamsplitter can be written as:

$$\hat{c} = \frac{\hat{a} + \hat{b}}{\sqrt{2}} \tag{2.32}$$

$$\hat{d} = \frac{\hat{b} - \hat{a}}{\sqrt{2}} \tag{2.33}$$

and hence the output intensities become:

$$\begin{aligned} \hat{n}_c = \hat{c}^\dagger \hat{c} &= \frac{\hat{a}^\dagger \hat{a} + \hat{b}^\dagger \hat{b} + \hat{a}^\dagger \hat{b} + \hat{b}^\dagger \hat{a}}{2} \\ \hat{n}_d = \hat{d}^\dagger \hat{d} &= \frac{\hat{b}^\dagger \hat{b} + \hat{a}^\dagger \hat{a} - \left(\hat{b}^\dagger \hat{a} + \hat{a}^\dagger \hat{b}\right)}{2}. \end{aligned} \tag{2.34}$$

Now we can look at the sums and the difference of the two outputs:

$$\hat{n}_c + \hat{n}_d = \hat{a}^\dagger \hat{a} + \hat{b}^\dagger \hat{b} \tag{2.35}$$

$$\hat{n}_c - \hat{n}_d = \hat{a}^\dagger \hat{b} + \hat{b}^\dagger \hat{a}, \tag{2.36}$$

where we see that the sum simply gives the total number of photons and the difference gives information about the cross terms.

Assuming the input in port b to be an intense coherent state, much brighter than that of port a we can make an expansion $\hat{b} = (\langle b \rangle + \delta\hat{b})e^{i\theta}$ where $\langle b \rangle$ is the classical amplitude of the coherent state and θ is its phase. Both $\hat{n}_c$ and $\hat{n}_d$ will be dominated by the amplitude of the coherent state from the b port, so we write them as classical intensities I_c and I_d respectively. Inserting this in Eq. 2.36) we get

$$I_c - I_d = i\langle b \rangle \left(\hat{a}^\dagger e^{i\theta} + \hat{a} e^{-i\theta}\right) + O(\delta\hat{b}\hat{a}) \approx \langle b \rangle \hat{q}\left(\theta\right). \tag{2.37}$$

Hence by measuring and subtracting the intensities I_c and I_d and controlling the phase of the coherent state in the b port we can get information about any quadrature of the a-field.

Seen in the general picture of POVM's the homodyne measurements of e.g. $\hat{x}$ have the completeness relation written as an integral over the infinitely squeezed states multiplied with the corresponding delta-function eigenvalues $1 = \int \delta(x, x')|x\rangle\langle x|dx$. The eigenstates are pure and orthogonal so they fulfill the criteria for being projective operators. The implementation using the homodyne detector destroys the state in the process of measurement and hence subsequent measurement on the same state is not possible. This can be modeled by a projective measurement followed by a partial trace.

Another Gaussian measurement is the heterodyne detector. It can be considered as the projection onto the coherent states, simultaneously measuring both $\hat{x}$ and $\hat{p}$ with the minimal noise penalty. The coherent states are not orthogonal, so the heterodyne detection is not projective. The detection can be realized in several ways, e.g. by splitting the state on a balanced beamsplitter (coupling it to a vacuum ancilla) and performing a $\hat{x}$ and a $\hat{p}$ homodyne detection on the two modes.

Both the homodyne and the heterodyne measurements are called Gaussian as they preserve the Gaussianity of Gaussian states. Such measurements can

be characterized with a covariance matrix corresponding to the Gaussian state which they project on to. For a multi-mode state consisting of subsystems A and B with the covariances C, the partial measurement of B can be written as

$$\sigma_{Am} = A - C(B + \sigma_m)^{-1}C^T, \tag{2.38}$$

where σ_m is the covariance matrix of the measurement. At the same time the mean value change according to

$$X_m = X^T(B + \sigma_m)^{-1}C^T. \tag{2.39}$$

2.0.9 Transformations between the different representations

For Gaussian states going between the different representations is particularly simple. Given the density matrix, the covariance and mean are calculated as the expectation values of the corresponding operators. On the other hand given the covariance matrix and mean values, the density matrix can be calculated in the following way: rotate the covariance matrix into diagonal form with the smallest variance in the x- direction corresponding to a phase shift θ. The variances are parameterized by the number of thermal photons and the squeezing and fulfill the relation

$$\mathrm{var}(\hat{x}) = (1 + 2N_{th})e^{-2r} \tag{2.40}$$

and

$$\mathrm{var}(\hat{p}) = (1 + 2N_{th})e^{2r}, \tag{2.41}$$

from which it can be seen that

$$\begin{aligned} N_{th} &= \frac{\sqrt{\mathrm{var}(\hat{x})\mathrm{var}(\hat{p})} - 1}{2} \\ r &= \frac{1}{4}\ln\left(\frac{\mathrm{var}(\hat{p})}{\mathrm{var}(\hat{x})}\right). \end{aligned} \tag{2.42}$$

Hence to generate the density matrix we generate a thermal state with N_{th} photons, squeeze it with the parameter r, rotate it with θ and finally displace it with the mean values using Eq. 2.26), Eq. 2.12) and Eq. 2.10).

The connection to the Wigner function is also straightforward,

$$W(\mathbf{x}) = \frac{1}{2\pi\sqrt{\det(\sigma)}}e^{\frac{1}{2}(\mathbf{x}-\bar{\mathbf{x}})^T\sigma^{-1}(\mathbf{x}-\bar{\mathbf{x}})}, \tag{2.43}$$

where we have written the coordinates and the expectation values as vectors. In Fig. 2.3 we show these three representations of a squeezed state. Even though the Wigner function and the density matrix have clear symmetries they are somewhat complicated, while the means are zero and the covariance matrix only has two non-zero entries.

In the more general case without the Gaussian assumption and by rewriting x and p as $x = r\cos(\phi)$ and $p = r\sin(\phi)$, we can compute the Wigner function as [5]

$$W(x,p) = \sum_{k=-M}^{M} w(r,k)e^{-ik\phi} \tag{2.44}$$

with

$$w(r,k) = \begin{cases} \sum_{n=0}^{M-k} w_n(r,k)\rho_{n+k,n} & \text{for } k \geq 0 \\ w(r,-k)^* & \text{for } k < 0 \end{cases}$$

$$w_n(r,k) = \frac{(-1)^n}{\pi}\sqrt{\frac{n!}{(n+k)!}}e^{-r^2}\left(r\sqrt{2}\right)^k L_n^k\left(2r^2\right) \tag{2.45}$$

where L_n^k are the generalized Laguerre polynomials. To go from the Wigner function to the density matrix, the density matrix elements are given by

$$\rho_{nm} = 2\pi \iint_{-\infty}^{\infty} W(x,p)w(r,n-m)e^{-i(n-m)\theta}dxdp. \tag{2.46}$$

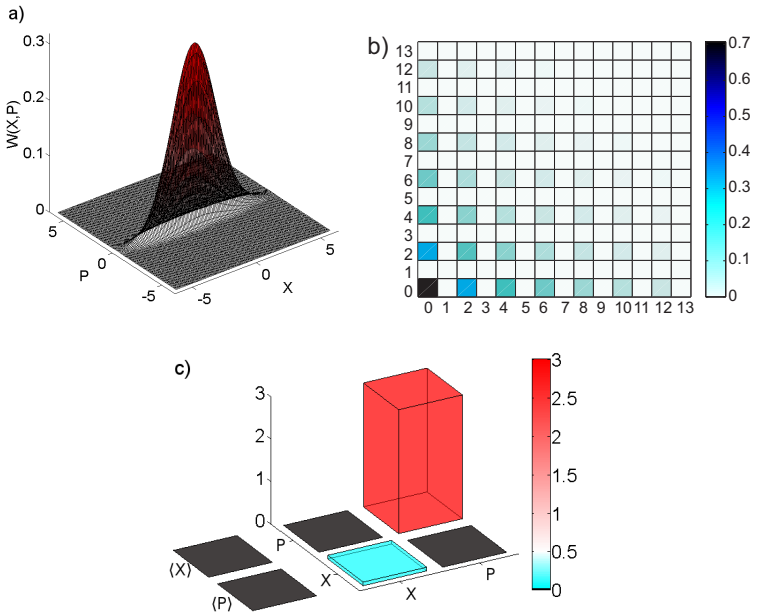

Figure 2.3: Representations of a squeezed state with 1 photon on average ($z = \sinh(\sqrt{1})$. a) The Wigner function. b) The absolute value of the corresponding density matrix. c) The mean values and covariance matrix.

2.1 Introduction to quantum information theory

In this section we will define the information of quantum states and show how it differs from the information of a classical system. We will start with the basics of classical information theory and then see how it translates into quantum information theory. Then we will see how we can calculate the different types of quantum information from the covariance matrices. Finally we will look at some of the measures of entanglement applicable to Gaussian states.

2.1.1 Entropy and information

The entropy of a system quantifies how much uncertainty or unknown information is present in it. If we are able to measure exactly what state the system is in, then we have gained an amount of information corresponding to the entropy. In this way the entropy and the information are two sides of the same story- the entropy is the information present in a system before measurement.

Imagine a person, Alice, having a systems A, we can write the Shannon (classical) entropy [10]

$$H(\mathrm{A}) = -\sum_x p(x) \log p(x), \tag{2.47}$$

where A has the outcomes x each with a probability $p(x)$ and $\sum_x p(x) = 1$. If we now imagine another person, Bob, with a system B we can quantify how much information Alice and Bob share (see Fig. 2.4). The joint entropy of the total system is given by

$$H(\mathrm{A},\mathrm{B}) = -\sum_{x,y} p(x,y) \log p(x,y), \tag{2.48}$$

where y are the possible outcomes of measurements on system B. This joint entropy is smaller than or equal to the sum of entropies of A and B and the equality holds if and only if A and B are independent. The difference is called the mutual information

$$H(\mathrm{A}:\mathrm{B}) = H(\mathrm{A}) + H(\mathrm{B}) - H(\mathrm{A},\mathrm{B}) \tag{2.49}$$

and it quantifies how much information A and B share. Further the conditional entropies of A given B can be defined as

$$H(\mathrm{A}|\mathrm{B}) = H(\mathrm{A},\mathrm{B}) - H(\mathrm{B}) \tag{2.50}$$

and vice versa for B conditioned on A. The conditional entropy quantifies how much information B is missing in order to know all of A.

Some of the properties of the Shannon entropies can be summarized as

1. Joint entropy and mutual information are symmetric: $H(\mathrm{A},\mathrm{B}) = H(\mathrm{B},\mathrm{A})$, $H(\mathrm{A}:\mathrm{B}) = H(\mathrm{B}:\mathrm{A})$
2. Conditional entropy is positive: $0 \leq H(\mathrm{A}|\mathrm{B}) \leq H(\mathrm{A})$.
3. Mutual information is positive: $0 \leq H(\mathrm{A}:\mathrm{B}) \leq H(\mathrm{A})$.

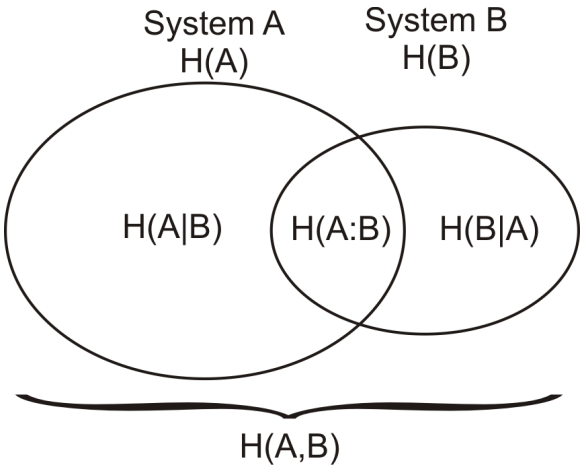

Figure 2.4: Overview of the classical entropy of a two-mode system.

4. Strong subadditivity: $H(\mathrm{A},\mathrm{B},\mathrm{C}) + H(\mathrm{B}) \leq H(\mathrm{A},\mathrm{B}) + H(\mathrm{B},\mathrm{C})$.

For a quantum state the von Neumann (quantum) entropy is defined from the density matrix as

$$S(\rho_A) = -\mathrm{trace}(\rho_A \log_2(\rho_A)) = -\sum_x \lambda_i \log_2(\lambda_i), \tag{2.51}$$

with λ_i being the eigenvalues of ρ_A and $0 \log_2 0 = 0$. The entropy is zero if and only if the state is pure, so in this sense single mode pure states contain zero information.

We can define the quantum joint entropy, conditional entropy and mutual information as we did for the classical quantities, only with the classical entropies replaced by the corresponding von Neumann entropies. However the intuitive picture in Fig. 2.4 will be misleading for quantum states, e.g the entangled states we saw in Sec. 2.0.5 were pure while their submodes were in mixed states. This means that in contrast to the classical entropy, the joint entropy $S(\rho_{AB})$ is not always bigger than the entropies of the submodes $S(\rho_A)$, so that the conditional information $S(\rho_B|\rho_A)$ is not always positive. In fact for a pure entangled state $S(\rho_{AB}) = 0$ while $0 < S(\rho_A) = S(\rho_B)$ and the quantum mutual information is twice that of each mode $S(\rho_A : \rho_B) = 2S(\rho_A)$.

The classical information is scale free in the sense that the outcomes are always orthogonal, which again means that all information can be extracted. This is not the case in quantum mechanics. The extractable information will be limited by the Heisenberg's uncertainty principle if the states are non-orthogonal. This is formulated in the Holevo bound which sets the upper limit to the extractable information. Suppose A prepares a state $\rho_A = \sum_i p_i \rho_i$ and then send it to B. If B performs a measurement on ρ_A described by a POVM, then the mutual information after measurement will be bounded

$$H(A : B) \leq S(\rho) - \sum_i p_i S(\rho_i), \tag{2.52}$$

which only depends on the prepared state.

Furthermore since [10] (§11.3.6)

$$S(\rho) - \sum_i p_i S(\rho_i) \leq H(A), \tag{2.53}$$

the extractable information is always smaller than or equal to the entropy of the prepared state. For the example with the pure entangled state this means that even though the quantum mutual information between A and B is $2S(\rho_A)$, if both A and B measure on their modes the extractable information is smaller than or equal to $H(A)$. This example shows the ambiguity of quantum information- on the one hand there is the power of entanglement (superpositions of correlations), but on the other hand the Heisenberg's uncertainty principle limits the information we can extract from a system.

2.1.2 Quantum information of Gaussian states

The infinite dimensionality of the Gaussian states at first seem staggering, however the symmetries of the states reduces the complexity to a few independent variables. This makes calculation of the quantum information quantities and optimizations much easier [1].

First we note that the mean value of the state does not have influence on the entropy of the state. Hence for Gaussian states all information is in the covariance matrix σ. Second we note that unitary transformations do not change the entropy. For the single mode state this means that if we produce the state by rotating a squeezed thermal state, then only the thermal state matters

$$S(\sigma_A) = f(1 + 2N_{th}), \tag{2.54}$$

where $f(x) = \frac{x+1}{2}\log(\frac{x+1}{2}) - \frac{x-1}{2}\log(\frac{x-1}{2})$. This result can be generalized to multi-mode Gaussian states by addition of $f(1+2N_{th,i})$ for each of the i modes. However this does not give the mutual information between two modes as it can be affected by two-mode unitary transformations. By only considering local unitary transformations the 4×4 covariance matrix of a two-mode state can be put into the standard form

$$\sigma_{AB} = \begin{pmatrix} \alpha & \gamma \\ \gamma & \beta \end{pmatrix}, \tag{2.55}$$

where the sub-matrices $\alpha = \mathrm{diag}(a, a)$, $\beta = \mathrm{diag}(b, b)$ and $\gamma = \mathrm{diag}(c_1, c_2)$. The determinants of these sub-matrices are invariant under local unitary transformations and are know as the local symplectic invariants. It is always possible to locally rotate and squeeze a covariance matrix into standard form and since these operations do not change the entropy one can always use the standard form for calculations. The entropy of the full system is still given by the two thermal contributions

$$S(\sigma_{AB}) = f(\nu_-) + f(\nu_+), \tag{2.56}$$

which can be calculated as $\nu_\pm = \sqrt{\frac{\Delta \pm \sqrt{\Delta^2 - 4\det(\sigma_{AB})}}{2}}$ where $\Delta = a^2 + b^2 + 2c_1c_2$. The ν's are also known as the symplectic eigenvalues. The von Neumann mutual information is then given by [11]:

$$S(\sigma_A : \sigma_B) = f(a) + f(b) - f(\nu_-) - f(\nu_+) \tag{2.57}$$

and the Holevo bound when Alice sends a state σ_B to Bob and Bob measures it is given by

$$\chi(\sigma_B) = S(\sigma_B) - S(\sigma_{B|a}) \tag{2.58}$$

where $\sigma_{B|a}$ is the state Bob receives conditioned on the information of Alice. To use this equation we describe the state that Alice send to Bob as part of a two-mode covariance matrix where Alice holds the remaining part herself. If Alice's data is classical then she measures her mode and Bob's conditional state can be calculated from Eq. 2.0.8.

2.1.3 Entanglement measures

Entanglement is a resource for several quantum information protocols. In principle it can be distilled and used to generate other entangled states, however it is not possible to distill entanglement from Gaussian states using Gaussian operations. For mixed states the entanglement of formation and the distillable entanglement are hard to calculate.

A more experimentally friendly approach to entanglement can be taken by using the Duan- Simon inseparability criterion

$$\mathrm{var}(\hat{x}_A - \hat{x}_B) + \mathrm{var}(\hat{p}_A + \hat{p}_B) < 4. \tag{2.59}$$

For symmetric Gaussian states the Duan- Simon criterion serves as a direct operational measure.

Mixed or asymmetric states can also contain entanglement. A measure which compromises being stringent, possible to calculate and working for all states is the logarithmic negativity. The basic idea is that if taking the transpose of one subsystem (partial transpose) on a separable state, then the state stays physical and obey the Heisenberg's inequality. The degree of violation then measures the entanglement, the only restriction that either Alice or Bob should only have one mode. The measure is defined as

$$E_N(\hat{\rho}) = \log ||\hat{\rho}^{T_B}||_1, \tag{2.60}$$

and for Gaussian states it can be calculated as

$$E_N(\sigma) = \sum_k F(\tilde{\nu}_k), \tag{2.61}$$

where $F(x) = -log(x)$ for x smaller than 1 and 0 otherwise and the $\tilde{\nu}_k$ are the eigenvalues of the partial transpose covariance matrix.

2.2 Introduction to the experiments

In this section we will go through some of the techniques and equipment used to generate, manipulate and measure the quantum states of light.

The starting point is the laser. We use a Diabolo Nd:YAG laser from Innolight. The main source of light is at 1064 nm, but it also has an internal second harmonic generator giving light at 532 nm. It is placed on an optical table where we guide the light around using lenses and mirrors.

In order to start the experiments with a vacuum state we use the sideband frequencies rather than center frequency to carry the quantum information. Most of our quantum states will be residing on the 4.9 MHz $\pm$ 90 kHz sideband frequency of the laser beam. The different sideband frequencies can be separated after measurement, hence we can have a bright center frequency (DC-component), relaxation noise of the laser at 1-3 MHz, several control modulations on e.g 12 MHz and 22 MHz frequency sidebands and still have e.g. a vacuum state on the 4.9 MHz sideband.

2.2.1 Mode matching

The first and most used technique we discuss is how to make two quantum modes overlap. In essence the technique is classical, however for a quantum mode imperfection directly leads to loss. Hence even though the ideas are very simple, they are all crucial for the successful implementation of an experiment. For two freely propagating laser beams meeting on a beamsplitter the light must be in the same mode in the following sense: same frequency, same Transverse ElectroMagnetic (TEM) mode, same polarization, same beam waist position and waist size and finally they must meet in the same point and have the same direction. The frequency is taken care of by using the same laser for the two beams. The polarization can be rotated with quarter- and half-wave plates and hence does not either pose a problem. The TEM mode does require precautions. Most often we use the TEM_{00} (a simple Gaussian beam profile), however to keep it that way ellipticity of the cavities, quality of optics (e.g. the crystals in the modulators) and of course avoiding unwanted stuff in the beam path, should be considered. Finally the actual alignment of the beams have to be perfected.

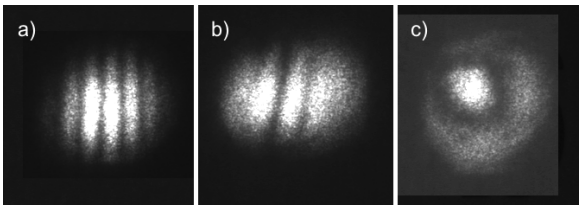

Figure 2.5: Misaligned overlaps. See text for description.

On Fig. 2.5 we show the most common alignment problems. In a) the beams are overlapping in the point where the picture is taken, but they are not going in the same direction giving phase interference ripples. In b) the opposite is the case and interference is only visible where they overlap. In c) they do not have the same focus giving different phase relations in the radial direction.

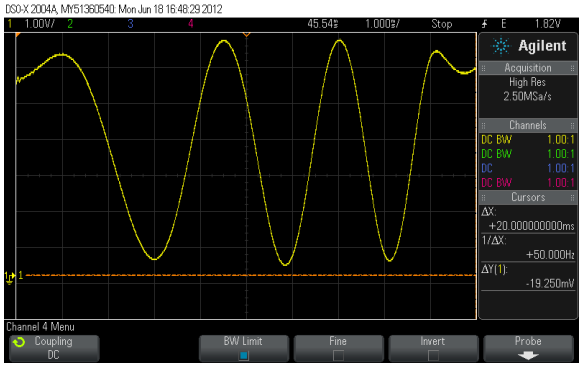

Figure 2.6: Visibility fringes of two equally powered beams, when scanning with a saw-tooth (linear scan). The minimum and maximum can be read of, possible DC offset of the detector should be taken into account. Here around 90% visibility in the middle and bit lower both to the left and right (due to tilting of the mirror). All the way to the left and to the right there are the turning points of the piezo.

Making these parameters match is a craft called mode matching. In principle this problem can be solved by ray tracing, giving the right position and direction of the beams, and using the ABCD formalism to get the right beam waist and position [12]. However to make it work in practice requires a bit of effort. Two steering mirrors are needed to control both direction and position. One can decouple these two degrees of freedom by placing one mirror far away from the beamsplitter to steer the position and one mirror close to the interference point to steer the direction of the beam. The two degrees of freedom will newer be completely decoupled, but by repeatingly over-steering with the one mirror and then with the other will allow to beam walk the beam to the right position and direction. A similar technique is used to control the position and size of the beam waist using proper lenses.

We quantify the mode matching between two beams by their visibility $\mathcal{V}$. By scanning the relative phase between the two beams using a piezo mounted mirror and detecting the intensity, visibility fringes can be observed on an oscilloscope, see Fig. 2.6. When the two beams have the same intensity the visibility is calculated from the maximum and minimum as

$$\mathcal{V} = \frac{I_{max} - I_{min}}{I_{max} + I_{min}}. \tag{2.62}$$

2.2.2 Locks

Once the overlap is aligned, we often want to stabilize the relative phase between the two beams. A feedback system is needed to compensate for acoustic vibrations and thermal drifts. To make such a feedback loop a signal is needed telling what the relative phase between the two beams is. This signal is called the error-signal as it tells the distance to the lock point. In essence, a good error-signal must have a sufficient bandwidth, a steep slope and a high signal to noise ratio.

If we want to lock the two beams out of phase, the most simple solution is to use the DC-component itself. A normal beamsplitter gives a π phase shift of the visibility fringes between two beams, hence subtracting the two output signals gives an error-signal which is insensitive to power fluctuations. If the power of one beam drifts, both signals are affected, but the subtraction cancels the drift and the lock holds the phase. If it is needed that both beams propagate after the interference a small part of each can be tapped of, e.g. using a 99/1 beamsplitter, and measured with a high-gain DC detector.

To lock two beams in phase with each other several techniques can be used depending on the exact application. AC-locking can be performed by placing a phase modulation on a sideband frequency as shown on Fig. 2.7. By measuring this modulated beam after the interference and mixing it down to DC, an error-signal which is phase shifted with $\frac{\pi}{2}$ is obtained. The $\frac{\pi}{2}$ phase shift means the slope is steepest on the minimum and maximum of the DC-interference and hence it can be used to lock to these. An alternative is to to make a DC-lock using polarization optics to control the phase of the beamsplitter called a Stokes based DC-lock.

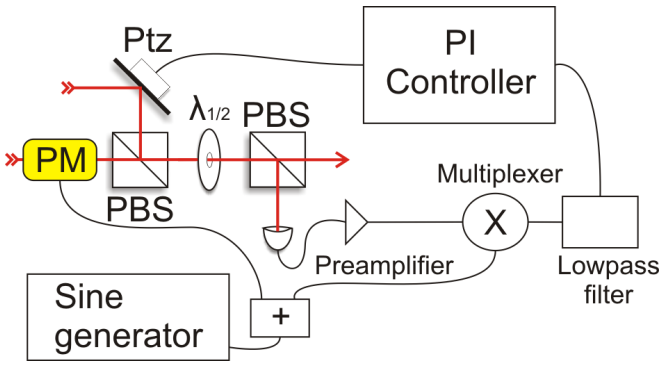

Figure 2.7: An AC feedback loop. Abbreviations: Phase Modulator PM, Polarization Beamsplitter PBS, Half-wave plate $\lambda_{1/2}$, Proportional Integral PI, Piezo mounted mirror Ptz. Together the two PBSs and the half-wave plate form a variable beamsplitter, hence the loss associated with locking the phase of the two beam can be distributed. Alternatively if both modes are needed with low loss, a small part one or each of the output beams can be measured.

The error-signal is fed to a proportional-integral (PI) amplifier, which gives an output which is partly proportional and partly the running integral of the error-signal. This output signal can then be amplified further or directly fed back to a piezo-mounted mirror in one of the two beams.

2.2.3 Cavities

A cavity defines a resonant optical mode and it has a limited bandwidth, hence we use cavities to define optical modes, low-pass high frequency noise and to locally enhance an optical mode. All the cavities have a piezo-mounted mirror, which can be used to control the length of the cavity. The cavities are

characterized by their finesse

$$\mathcal{F} = \frac{2\pi}{1-R} = \frac{FSR}{\gamma}, \tag{2.63}$$

where R is the roundtrip loss, FSR is the free spectral range and γ is the full with half maximum of the transmission peaks. The ratio can be measured directly by scanning the length of a cavity with the piezo-mounted mirror. The measured finesse can be compared to the expected from the length of the cavity and the reflectance of the mirrors, as well as to compare the day to day results. The cavities are locked to resonance using Pound-Drever-Hall (PDH) like locking technique [13] similar to the above mentioned AC-lock Fig. 2.7.

The procedure to align a cavity depends on the cavity geometry and where it is possible to access the beam. The first step is to prepare the seed to have the right waist position and size, compared to the optical mode of the cavity. This can be calculated with the ABCD formalism. The beam should be traced around the first roundtrip of the cavity making sure it hits the mirrors in the centers. When this is done at least two or more faint spots should be visible on the output, corresponding to the first and second roundtrip. The cavity mirrors or the steering mirrors are then used to beam walk the spots closer. When the spots close up they should start to have unstable brightness caused by the growing interference. Now by slowly scanning the length of the cavity (less than 1 hz) the spot should be blinking. The spot can now be sent on to a detector connected to an oscilloscope synchronized with the scan and the scan speed set to e.g. 30 hz. Most likely there will be "a forest" of modes, further mode matching allows to align the cavity to have the TEM_{00} highly dominant. By again scanning slowly and looking at the output modes any other resonant modes can be identified. To test the alignment the Hermite-Gauss TEM_{01} and TEM_{10} modes can be excited. By comparing the symmetry one can check that there is room on all sides of the beam path inside the cavity as these modes have larger and asymmetrical spatial profiles and hence they can tell if the beam is slightly cutting and in which plane.

2.2.4 Displacements and mixtures of coherent states

Displaced vacuum states can be generated by sending a seed through a phase or an amplitude modulator driven by a sine (function) generator. To avoid dephasing the sine generator should be synchronized with the sine generator from the measurement. We use commercially available electro-optical modulators (EOM) from Linos and New Focus and the operation simply requires that the light is sent through. They work by applying an electric field to a LiNbO3, MgO:LiNbO3 or KTP crystal which change its refractive index thereby changing the length of the optical path. The phase modulators can work with a single crystal and the change in optical path length directly gives the modulation (the Linos ones have several crystals for enhanced temperature stability). The amplitude modulators have two crystals oriented 90° relative to each other. If the light is polarized along the crystals it gives phase modulation. If the light has a 45° or circular polarization relative to the two crystals the two polarization modes form a polarization Mach-Zehnder interferometer. Each mode of the interferometer is phase modulated and by interfering them on a PBS afterwards

amplitude modulation is generated. Any intermediate modulation can be generated by the polarization. Overall this works very efficiently and basically any desired displacement can be realized as a pure state.

Thermal states are also easily generated using these modulators. By driving a pair of phase and amplitude modulators with independent white noise sources, a wide range of thermal states can be realized.

For some of the experiments we want to store the information of the white noise modulation so that the thermal states are conditional vacuum states. This is a little more complicated. If we simply mix down the white noise from the source, the signal to noise ratio is limited to 15-18 dB by a weak but complex transfer function in the modulator. To circumvent this we can measure a part of the modulated light directly, with a much greater signal to noise ratio than the signal to noise ratio in the final seed. If the detector has the same transfer function as the ones used for detection in the end of the protocol, then the signal to noise ratio will only be limited by the phase locks or the dynamical range of the detectors.

The modulators are not lossless, however displacements are only attenuated by loss. So if we want to displace a fragile quantum state we can make an ancilla state with a modulation 100 times bigger than wanted, couple the two on a 99/1 beamsplitter and lock their relative phase which then only results in a small loss to the fragile quantum state.

2.2.5 Optical parametric amplifiers

To generate squeezed states we use the χ_2 non-linear coefficient of a 10 mm long type 1 periodically poled potassium titanyl phosphate (PPKTP) crystal for parametric down-conversion. The crystal is designed to generate squeezing at 1064 nm when it is pumped with a 532 nm pump beam. The crystals are anti-reflection coated (R $\sim 0.5\%$, recently changed to new R $\sim 0.2\%$) to reduce the back-reflection and the associated loss. The effective χ_2 coefficient is too low in free space, so to enhance the efficiency of the down-conversion process we place the crystal in a cavity resonant for 1064 nm, while the 532 nm pump beam is single passed. The cavity is a bow-tie shaped cavity which is designed to have a 25 cm round trip length and a beam waist in the crystal fulfilling the Boyd-Kleinman criterion [14]. The crystal is placed on a Peltier element which heats it up to around 30° C. The cavity with the crystal inside is called an optical parametric amplifier (OPA) when operated below threshold and we have two of these on the optical table, see Fig. 2.8. We need a seed (some light) on the center frequency of the squeezed mode which can be used as a phase reference for locking later in the experiment. The seed is coupled into the cavity with an incoupling mirror with high reflection ($\sim 99.8\%$) while the outcoupling mirror is 92% in OPA1 and 90% in OPA2. This highly asymmetrical coupling, together with the other losses in the cavity, gives a finesse of ~ 55 corresponding to an outcoupling efficiency of around 90% and a bandwidth between 20 and 25 MHz.

The cavity is locked with a counter-propagating lock beam. A small part of this lock beam is back reflected by the crystal. This can cause instabilities in the seed intensity when the interference drifts. In front of OPA1 we have placed an acousto-optical modulator in the lock beam which moves the frequency of the light so that the Hermite-Gauss TEM_{10} resonance overlaps with the TEM_{00} of the seed beam. Since the two beams are in different spatial modes even after

back-reflection they do not interfere and the intensity instabilities are avoided. In the other OPA the crystal is slightly tilted which reduces the back reflection significantly.

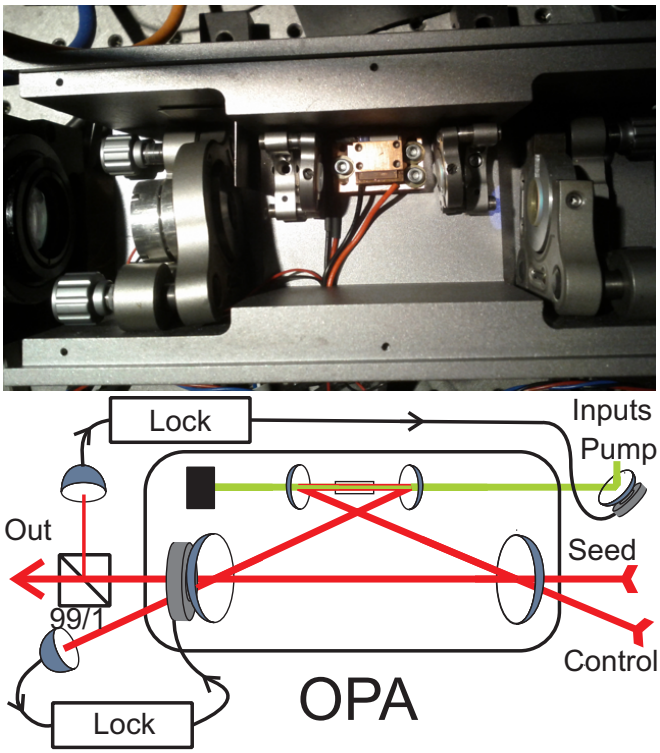

Figure 2.8: Upper: Picture of OPA1. To the left on the big mirror mount is the outcoupling mirror which is mounted on a piezo. In the middle we have the crystal which is placed on the oven (with the black and red wires). The pump enters to the right through a slit in the mirror mount and both the seed and the lock beam enters through this big mirror. Lower: Sketch of an OPA with locking loops and control beams. The locks consist of the above mentioned AC-locking system, a proportional integral amplifier and a high-voltage amplifier. Note that the input beams are much more intense and that most of them are reflected.

Aligning the pump beam is a little tricky as the overlap between it and the seed only is visible when the parametric amplification gain is working. Furthermore the beams are only overlapping inside the cavity and the green beam is blocked before exiting. Hence we use an IR beam sent backwards into the cavity through the outcoupling mirror to generate some green light (using the OPA as a second harmonic generator) and align it back to the green mode-cleaning cavity. This procedure gives some gain, which can be optimized with normal beam walking.

The r parameter of the theoretical squeezing operator is proportional to the non-linear coefficient of the crystal, the cavity finesse and the pump power. The nonlinear coefficient of the crystal (including the poling structure) can be

optimized by controlling the temperature. Changing the cavity finesse can be done by changing the outcoupling mirror. This is however a trade-off because increasing the finesse decreases the outcoupling efficiency. Furthermore it would decrease the bandwidth which for the 4.9 MHz would slightly decrease the transmission and more importantly increase the coupling between the quadratures. Considering lower frequency sidebands where these effects are smaller would require that the laser was shot noise limited at that frequency. The pump power also has an optimum, because the increased antisqueezing and the coupling between squeezing and anti-squeezing at some point degrades the squeezing. The trade-off between the cavity finesse and the pump power are coupled, however by increasing the pump power and decreasing the finesse (by increasing the outcoupling) should give higher outcoupling efficiency and thereby more squeezing.

The phase of the squeezing is given by the phase of the pump relative to the seed. There is a 12 MHz phase modulation on the green light from the laser. After the OPA we tap off a small part of the squeezed seed to perform an AC lock as shown in Fig. 2.8, which can lock to either phase or amplitude squeezing. Both lock points are possible with the same error-signal due to the π symmetry of the squeezing phase. The size of this error-signal sets the lower limit on the r parameter, as the locking becomes unstable when turning down the pump power. It is however always possible to attenuate the squeezed beam, thereby lowering the degree of squeezing and it is also possible to increase the antisqueezing by white noise modulation.

Comparing with state of the art squeezing [15, 16] our main limitations are in the phase stability of the OPAs, the outcoupling and detection efficiency (see next section), but further we always have a relative long path to the detection including the phase lock of the pump phase and the coupling of the two OPAs.

2.2.6 Detection

All our detectors are basically amplified pin-diodes. For locking, we have resonant detectors which give a higher signal to noise ratio at the cost of bandwidth. For homodyne detection, we mostly use broad band detectors with a bandwidth above 20 MHz and low electronic noise. Some of the detectors amplify everything equally and some split the AC and DC components allowing different gains.

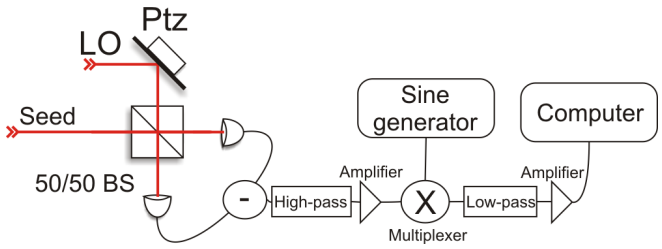

Figure 2.9: Sketch of data acquisition.

To set up a homodyne detector two detectors are needed, see Fig. 2.9; The seed and the local oscillator are overlapped on a 50/50 beamsplitter, the perfection of the overlap and the beamsplitting ratio being equally important.

The output beams are focused onto each of the detector diodes. The size of the electronic outputs should be balanced. This is done by placing a white-noise modulation on the seed or on the local oscillator and blocking the other beam. The single detector output can be compared with the subtraction of the two detectors on a electronic spectrum analyzer. We refer to this subtraction as the common mode rejection and it should be in the order of 30 dB within the measurement bandwidth. Once balanced, the electronic output of the two detectors is subtracted to obtain the quadrature as in Eq. 2.37. We have one set of broadband homodyne detectors with an estimated detection efficiency of $94\% \pm 2\%$ and a few sets with $90\% \pm 2\%$. The phase of the local oscillator can either be scanned or locked depending on the purpose of the measurement.

One way to check whether the measurements are shot noise limited is to vary the optical power and check the linearity. An alternative way is to check that the addition and subtraction of the balanced detectors give the same signal. Furthermore the clearance to the dark/electronic noise of the detectors should be measured; typically it is 20 dB. Finally the DC component of the seed should be much fainter than the local oscillator to validate the approximation in Eq. (2.37). Comparing with that equation there is an extra frequency of 4.9 MHz on our measured quadrature. Hence we need to mix it down before low-passing it. The low-pass filter sets the bandwidth of the data and in most of the experiments we use a 90 kHz second order filter. Finally the data is sent to the computer where it is sampled at 500 kHz by an analog to digital converter. The converter has 4 inputs, 14 bit depth and a sampling rate up to 100 MHz.

2.2.7 Single mode states

With a homodyne detector the vacuum state (shot noise) can be measured and the result of such a measurement is shown in Fig. 2.10. Whenever making a measurement series, several shot noise measurements are taken to check the power stability of the local oscillator. The standard deviation of one of these data sets is used to normalize the other measurements, corresponding to setting $\hbar = 2$. The vacuum state is symmetric so we cannot see if we are scanning the local oscillator or have it locked to a given quadrature.

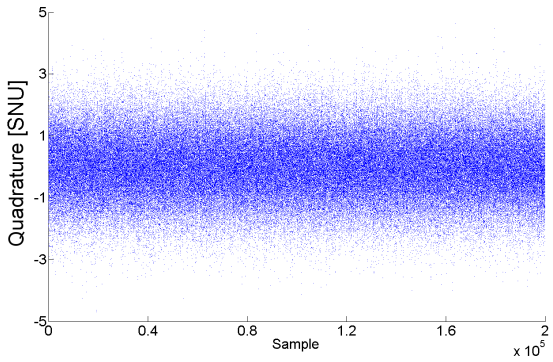

Figure 2.10: Data of a vacuum state (normalized).

If we now turn on an OPA, scan the phase of the local oscillator and measure, we see that at some phases the data points are more centered while at other phases they are more wide spread, shown in upper part of Fig. 2.11. When scanning the phase of the local oscillator, time resolved measurements gives different phases. Hence samples in the figures corresponds to phase of the state. The focusing and spreading of the data could also be measured on a state with one noisy quadrature. The difference is that for the squeezed state the points are more centered than for the vacuum state. This can be seen by binning the points (here 1k per bin), calculating the variance and comparing it with the shot noise as done in the lower part of Fig. 2.11 (showing 4.5 dB of squeezing and 8 dB of antisqueezing). In a similar fashion we can measure a coherent state, the result of which is shown in the upper part of Fig. 2.12.

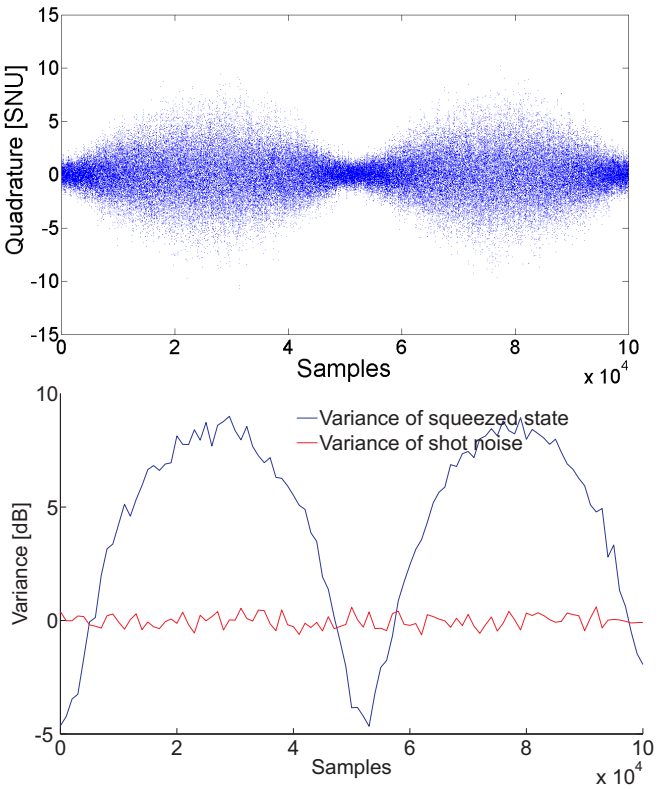

Figure 2.11: Phase scan of an amplitude squeezed state. Upper figure: raw data. Lower figure: running variance of the data compared with shot noise

If we both squeeze and displace, the relative phase between the two matters as shown in the middle and lower part of Fig. 2.12. We see that if we squeeze along the displament, the amplitude of the coherent state becomes better defined and when squeezing orthogonally to the displacement the phase (the position of the steepest slope) of the state becomes better defined.

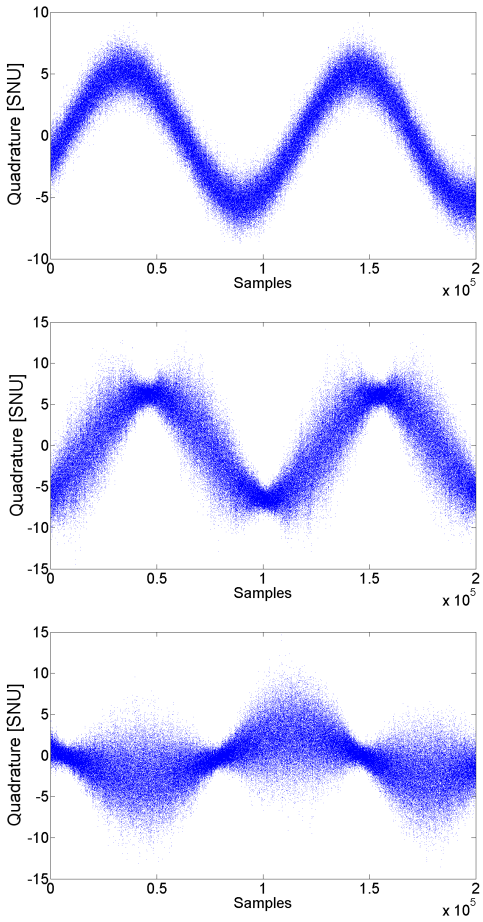

Figure 2.12: Upper: Phase scan of a phase quadrature displaced coherent state. Middle figure: squeezing and displacing the same quadrature. Lower figure: squeezing out of phase with the displacement.

2.2.8 Two mode states

To measure two-mode states we need two sets of detectors. We commonly refer to the one set of detectors as belonging to Alice or A and the other set to belong to Bob or B. The two sets of detectors need to be synchronized, which is done by splitting a strong thermal seed, blocking one detector from each set of detectors and subtracting the signals from the two other. It is not essential that they have the same gain as each set will be normalized to their respective shotnoise, but they have to be perfectly in phase with each other. By turning on our two OPAs and locking the two seeds with a $\frac{\pi}{2}$ phase shift (e.g. amplitude squeezing from both OPAs and a tap off DC-lock), we can generate the entangled state shown in Fig. 2.13. We see that even though each of the modes are in symmetric noisy (thermal) states, 3 dB of two-mode squeezing is observed between difference of the one quadrature and the sum of the other quadrature witnessing entanglement with the Duan- Simon criterion.

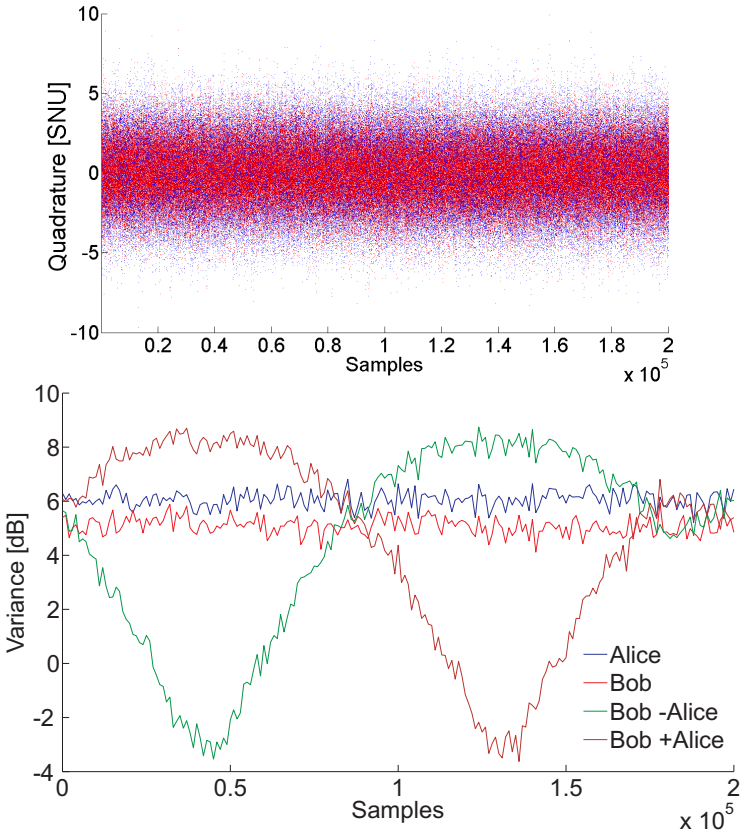

Figure 2.13: Homodyne measurement of an entangled state. The phase of the homodyne detector at Alice (blue points) is locked while the phase of the homodyne detector at Bob (blue points) is scanned. The data sets are first normalized to their individual shot noise, and the sum/difference is divided by two. Upper figure: raw data. Lower figure: the variance of Alice, Bob, their sum and their difference.

Chapter 3

Gaussian quantum discord

3.1 Introduction

Entanglement is undoubtedly a key resource in quantum information science and it has become synonymous with different nonclassical tasks such as quantum teleportation, dense coding and quantum computation [10]. However, despite its obvious importance for such tasks, the exact need of entanglement in some other non-classical tasks has remained enigmatic. It has for example been shown that some quantum computational tasks based on a single qubit (the socalled DQC1 model) can be carried out by separable (that is, non-entangled) states that nonetheless carries non-classical correlations [17–20]. Another quantum task requiring the use of quantum correlations but not entanglement is quantum key distribution [21, 22]. This indicates that there exist genuine quantum correlations different from entanglement, which allow for information processing that is intractable by classical means.

In Sec. 2.1.1 we saw that we can define the quantum mutual information which gives a measure of all the correlations between two modes of a quantum state. If measuring one mode of a two-mode quantum system with correlations, the mutual information is most often reduced. When performing the measurement which extracts the most of the total information, the reduction quantifies the quantum correlations of the system and is called the quantum discord [23, 24].

The quest of understanding the possible use of quantum discord for quantum tasks has fueled an explosion in the research of discord spanning from the investigations of its evolution in noisy Markovian [25–29] and non-Markovian [30,31] channels to its role in thermodynamics [32] and phase transitions in spin systems [33]. This measure has been given an operational interpretation in terms of the required resource for enabling quantum state merging [34, 35] and local broadcasting [36].

Most work on quantum discord has been focused on finite dimensional systems including qubits and qudits but recently the discussion has been extended to infinite dimensional systems also known as continuous variable systems [37–39]. This extension has mainly been restricted to the set of Gaussian states and Gaussian measurements [37,38], partly due to the associated reduced mathematical complexity of the problem and partly due to their immense im-

portance for quantum information processing and their simplistic generation [2]: Gaussian states can be efficiently prepared [40] and allow for secure quantum communication [22], near-optimal cloning [41] and teleportation [42].

The robustness of non-classical states against noise and loss is of high importance as real-world quantum information protocols will inevitably consist of noisy and lossy operations. Entanglement is known to be a fragile resource which is difficult to generate and the optimal use of it would require complex purification and distillation protocols. On the contrary, it has been shown theoretically that quantum discord of some states is robust against Markovian decoherence, and in fact discord can increase through dissipation both for discrete [25,27,28] and for continuous [26] variable systems.

Most studies of discord so far have been theoretical, however recently two other experimental investigations of Gaussian discord have appeared [43, 44].

This chapter is structured as follows: First we formalize the closed formulas for calculating the Gaussian discord. We experimentally characterize the Gaussian quantum discord of EPR-states and separable two-mode mixtures of coherent states. We investigate the evolution of the Gaussian quantum discord in an open quantum system described by local Markovian decoherence in the form of Gaussian noise addition corresponding to a classical noise channel and pure attenuation. We then turn our attention to a broader range of simulations and discuss the robustness of the discord and which states that would be suitable for testing operational interpretations of the discord.

3.2 Theory of the Gaussian discord

The entropy of a Gaussian two-mode state is fully characterized by the covariance matrices which can be experimentally accessed from homodyne measurements. Up to local unitaries the 4×4 covariance matrix for the state ρ_{AB} can be written as

$$\sigma_{AB} = \begin{pmatrix} \alpha & \gamma \\ \gamma^T & \beta \end{pmatrix} \tag{3.1}$$

where the sub-matrices $\alpha = \mathrm{diag}\,[\mathrm{var}(x_A), \mathrm{var}(p_A)]$, $\beta = \mathrm{diag}\,[\mathrm{var}(x_B), \mathrm{var}(p_B)]$ and $\gamma = \mathrm{diag}\,[\mathrm{cov}(x_A, x_B), \mathrm{cov}(p_A, p_B)]$. This form is called the standard form as each sub-matrix is diagonal.

In the following we formalize the Gaussian quantum discord [37, 38]. In a bipartite system, the total amount of correlations (classical and quantum) is given by the von Neumann mutual information $I(\rho_{AB}) = S(\rho_A) + S(\rho_B) - S(\rho_{AB})$ where $S(\rho)$ is the von Neumann entropy and $\rho_{A(B)}$ is the reduced density matrix of the A (B) subsystem. Another measure of mutual information that only quantifies the one-way classical correlations extractable by a Gaussian measurement is $J_A(\rho_{AB}) = S(\rho_A) - \inf_{\sigma_M} S(\rho_{A|\sigma_M})$ where σ_M is the covariance matrix of the measurement on mode B. In other words, J is the mutual information of a two-mode quantum state after an measurement of mode B optimized to extract the most of the correlations.

As it only captures the one-way classical correlations, the difference, $\mathcal{D}_A = I(\rho_{AB}) - J_A(\rho_{AB})$, is a measure of Gaussian quantum correlation that is coined Gaussian quantum discord. An explicit expression for this discord of all Gaussian states has been found [37]:

$$\mathcal{D}(\sigma_{AB}) = \mathfrak{f}(\sqrt{I_2}) - \mathfrak{f}(\nu_-) - \mathfrak{f}(\nu_+) + \mathfrak{f}(\sqrt{E^{min}}) \tag{3.2}$$

where $\mathfrak{f}(x) = (\frac{x+1}{2})\log\frac{x+1}{2} - (\frac{x-1}{2})\log\frac{x-1}{2}$ and

$$E^{min} = \begin{cases} \frac{2I_3^2+(I_2-1)(I_4-I_1)+2|I_3|\sqrt{I_3^2+(I_2-1)(I_4-I_1)}}{(I_2-1)^2} & \text{a)} \\ \frac{I_1I_2-I_3^2+I_4-\sqrt{I_3^4+(I_4-I_1I_2)^2-2C^2(I_4+I_1I_2)}}{2I_2} & \text{b)} \end{cases} \tag{3.3}$$

where a) applies if $(I_4 - I_1I_2)^2 \leq I_3^2(I_2+1)(I_1+I_4)$ and b) applies otherwise. $I_1 = \det\alpha$, $I_2 = \det\beta$, $I_3 = \det\gamma$, $I_4 = \det\sigma_{AB}$ are the symplectic invariants and $\nu_\pm^2 = \frac{1}{2}(\delta \pm \sqrt{\delta^2 - 4I_4})$, with $\delta = I_1+I_2+2I_3$, are the symplectic eigenvalues. Most of the states we will discuss fulfill the criterion a), which corresponds to a heterodyne detection.

3.3 Experimental characterization

Figure 3.1 shows the experimental setup that was used to generate quantum correlated Gaussian states. A pair of optical parametric amplifiers (OPAs) based on type I quasi-phase-matched periodically poled KTP cystals placed inside bow-tie shaped cavities were used to generate two independent amplitude squeezed beams at 1064 nm. The OPAs were seeded with dim laser beams at 1064 nm to facilitate the locking of the cavities and several phases of the experiment. Both OPA outputs had 3.2 $\pm$0.2 dB of squeezing and 6.7 $\pm$0.2 dB of anti-squeezing which was measured with a homodyne detector with a total efficiency of $85\pm5\%$ and electronic noise contribution of -20 dB relative to shot noise. The measurements were performed at the sideband frequency of 4.9 MHz with a bandwidth of 90 kHz. In order to generate correlations in addition to those produced in the OPAs, one of the seed beams was symmetrically modulated with two electro-optic modulators - an amplitude and a phase modulator - that were driven by independent electronic noise generators. We interfered the two squeezed beams on a symmetric beam splitter with a relative phase locked at $\pi/2$ to produce a pair of quadrature entangled beams. One of the output beams propagated through a dissipative channel which was implemented by a beam splitter with a variable transmittivity. This setup can hence generate and characterize a variety of two-mode Gaussian states.

3.3.1 Entangled states

Using the experimentally obtained covariance matrix of the two-mode squeezed state, we calculate the Gaussian discord for different attenuations of mode B. The results for the mutual information are shown in figure 3.2 a) and the discord in figure 3.2 b). As usually expected for quantum correlations in a dissipative channel, we see a monotonic decrease of the Gaussian discord with increasing dissipation. A similar behavior is expected and observed for the entanglement of the state as shown in the inset of figure 3.2 where the logarithmic negativity is plotted against attenuation [45]. We thus conclude that for this particular two-mode squeezed state, dissipation has a degrading influence on both entanglement and discord. However, it is well-known that entangled states are not the only

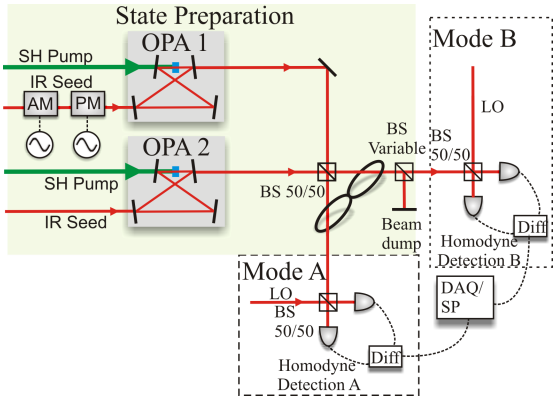

Figure 3.1: Experimental setup. See main text for description. Abbreviations: IR: infrared (1064 nm), SH: second harmonic (532 nm), PM and AM: phase and amplitude modulator, OPA: optical parametric amplifier, BS: beamsplitter, LO: local oscillator. DAQ/SP data acquisition/ signal processing

ones containing Gaussian discord. A two-mode mixed separable state may also contain Gaussian discord as we shall see in the following.

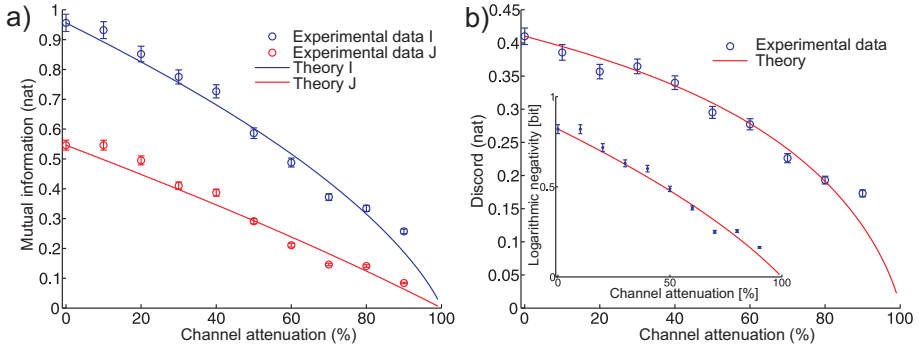

Figure 3.2: a) Mutual information for the two-mode squeezed state with the circles representing the I information (blue) and the J information (red), measured with the natural logarithm as base (nat). The curves correspond to theoretical curves fitted to the first data point. b) Quantum discord and logaritmic negativity (inset) for the two-mode state as a function of attenuation. The experimental data (circles) show the discord and logaritmic negativity calculated from the measured covariance matrices and the solid lines are theoretical predictions from the first measurement point (with no attenuation).

3.3.2 Mixtures of coherent states

In the experiment we generate a separable mixed state by enabling the electronic noise generators and disabling the OPA's (see Fig. 3.1). This corresponds to the splitting of a thermal state on a symmetric beam splitter and thus the

generation of a two-mode mixture of coherent states with correlations between the amplitude quadratures and the phase quadratures of the two modes. For this state, we measure the covariance matrix for different modulation depths of the modulators and subsequently calculate the discord with the results shown in Fig. 3.3 (green circles). The theoretically expected behavior of the discord for the mixed state is represented by the solid red line which is monotonically increasing, eventually saturating for large modulations. We see that the experimentally obtained values of the discord decrease for very large modulations thus deviating from the theoretically predicted behavior. This discrepancy is simply due to finite balancing between the two homodyne detectors which we measured to have a common mode rejection ratio of 27 dB. Such an imperfection of our detection system leads to the measurement of uncorrelated events which directly simulate a classically noisy channel where the amount of noise scales with the modulation depth. Since we are interested in simulating the effect of classical noise on the discord, we decided to reduce the common mode rejection ratio of the two detectors to 15 dB. The results for the discord are shown by the red circles in Fig. 3.3 a), and the constituents - the mutual information I and J - are presented in Fig. 3.3 b). We thus observe the transition from a quantum regime with non-zero discord to a classical regime with near zero discord characterized by having a high energy but finite signal to noise ratio in the correlations.

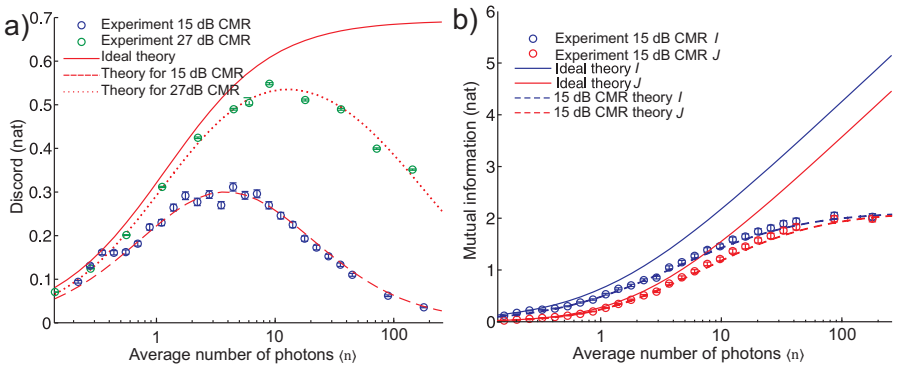

Figure 3.3: a) Quantum discord as a function of the modulation depth. The circles represent the experimentally obtained data for discord with 27 dB (green) and 15 dB (blue) common-mode-rejection (CMR) between the homodyne detector at A and the homodyne detecor at B. b) Mutual information I and J as a function of the modulation depth. The circles represent the experimentally obtained data. Solid lines result from theory with perfect detectors (corresponding to a noise-free channel) whereas the dashed and dot-dashed curves are the results of the theory including CMR and electronic noise. The error bars are given by the statistical uncertainties.

In the next step we investigate the effect of dissipation on the mixtures of coherent states. The results are shown in figure 3.4 for different amounts of modulation (partially resulting in classically noisy channels). From these measurements we see, interestingly, that the discord increases as a function of local and Markovian dissipation. We do not only observe an extreme robustness of discord associated with the separable state but also a clear rise of quantum cor-

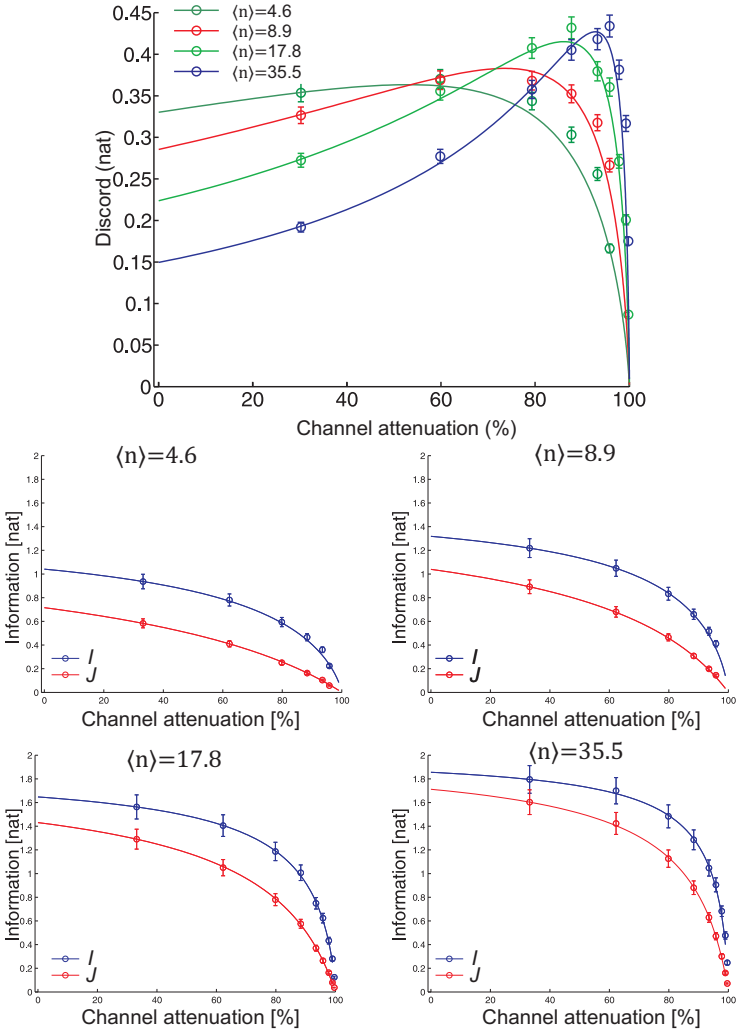

Figure 3.4: Upper: The discord of four mixed states from figure 3.3 with different average photon numbers $\langle n \rangle$ as a function of attenuation of mode B. The error-bars are given by the statistical uncertainty. The solid lines are theoretical estimations, fitted to the first data point associated with zero attenuation. Lower: the corresponding mutual information (blue lines) and one-way classical information (red lines)

relations during dissipative dynamics. This is in stark contrast to entanglement which cannot increase under any local (unitary or non-unitary) transformations [46]. Ultimately, it is possible to observe the complete death of discord through classical noise addition and its subsequent revival through dissipation as partially demonstrated in figure 3.3 (near death) and figure 3.4 (revival).

We interestingly note that the discord of the classically noisy state investigated above can be revived after death even if the state at A has been measured, stored in a classical memory and subsequently recreated.

The revival of the discord as a result of dissipation can be understood from two effects. The first one is the attenuation of the uncorrelated classical noise in mode B, which is responsible for the near death of the discord in figure 3.3. This effect is hence the main contributor to the revival of the discord when uncorrelated noise above shot noise is present. The second effect that leads to a further increase in the discord results from the relatively higher amplitude of mode A. This makes the inevitable noise contribution of a measurement on mode B more significant and thereby increase the difference between the information obtainable by quantum and classical means.

3.4 Simulations of Gaussian discord

3.4.1 The robustness of discord

Although the Gaussian discord of our experimentally obtained separable states is more resilient to losses than that of the entangled states, it is important to point out that for the same amount of energy of the two types of states, the entangled state will for any amount of Markovian loss exhibit the highest discord. This is illustrated in figure 3.5 where the discord of pure entangled and separable states with mean photon numbers between 1 and 100 (1 and 10 photons corresponding to 5.7 dB and 13.4 dB of two-mode squeezing) is plotted against attenuation (in dB). Needless to say, such pure entangled states are much more difficult to produce than the more robust two-mode mixed coherent state with 100 photons (green curve in Fig. 3.5) which is straightforwardly produced with electro-optical modulators.

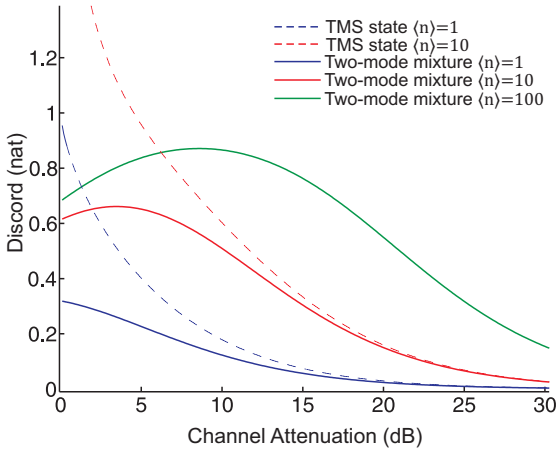

Figure 3.5: Theoretical simulations of the evolution of Gaussian discord in an attenuating channel for pure two-mode squeezed (TMS) EPR-states and two-mode mixtures of coherent states.

3.4.2 The reverse discord

So far we have only considered the discord when measuring mode B. Instead we now consider measuring mode A still sending mode B through an attenuating channel. We have made simulations showing that the discord D_B then monotonically degrades as shown in Fig. 3.6.

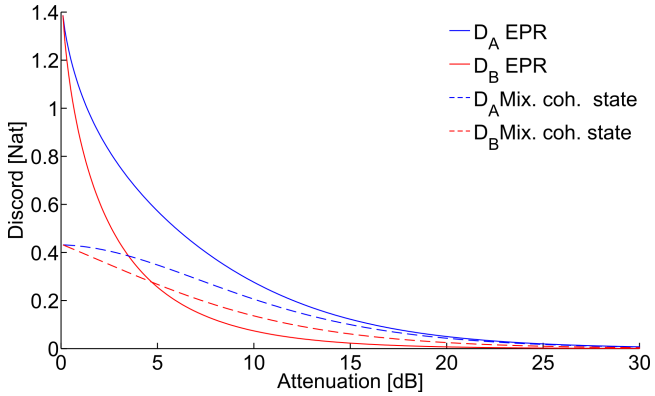

Figure 3.6: Theoretical comparison of the evolution of Gaussian discord when mode B is in an attenuating channel for pure two-mode squeezed (EPR) states and two-mode mixtures of coherent states (Mix. coh.) for the discord measuring mode A and measuring mode B. All the states have 2 photons on average.

3.4.3 Phase conjugation

We have looked at entangled states for which the correlations contained in the sub-matrix γ have the opposite sign, corresponding to $\det(\gamma) < 0$ (the x-quadratures are correlated and the p- quadratures are anticorrelated). Secondly we looked at mixtures of coherent states where the corresponding correlations have the same sign, corresponding to $\det(\gamma) > 0$. For the entangled states it is not possible to switch the sign as it would violate the Heisenberg's uncertainty principle. However, for the mixture of coherent states it is possible to generate states with $\det(\gamma) > 0$ and states with $\det(\gamma) < 0$. Instead of interfering a thermal state and a vacuum state on the beamsplitter we could interfere states modulated in one quadrature only and lock them with a $\frac{\pi}{2}$ phase shift. After the beamsplitter the single mode states would be identical to the ones where both quadratures are correlated, however as for the EPR states they would have anti-correlated p-quadratures. We simulate how these states perform in an attenuating channel in Fig 3.7. We see that the two states carry the same classical information. This makes intuitive sense since phase conjugation does not change the entropy of classical states. Surprisingly we see that the quantum mutual information is very different for the two states, giving rise to a significant difference in the discord.

These two types of mixtures of coherent state have all the same properties, same energy, same single mode entropy, same classical information and no entanglement. This means that they will perform equally in any protocol which rely on these parameters, but not if the protocol rely on quantum discord. In

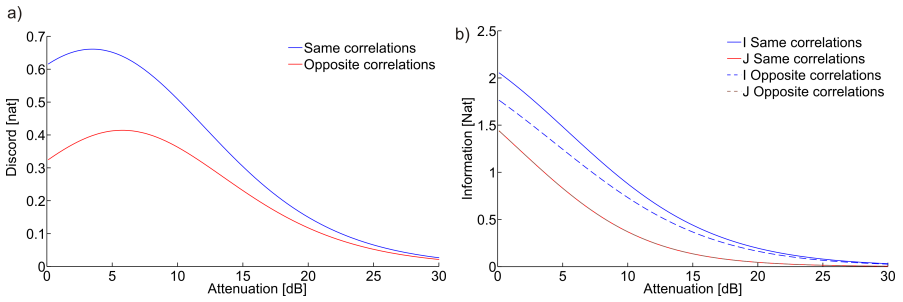

Figure 3.7: Theoretical comparison of the discord a) and informations I and J b) for phase conjugate mixtures of coherent states in an attenuating channel. Same/opposite correlations means that $\det(\gamma)$ is positive/negative. All the states have 10 photons on average.

this way the states are ideal test states when searching for operational interpretations of Gaussian quantum discord.

3.4.4 Modulated EPR states

Next we look at how the Gaussian discord of EPR-states perform when adding coherent modulation to the states. We have performed simulations by adding coherent modulation with $\det(\gamma) < 0$ to already entangled states. If applied symmetrically to both modes the behavior shown in Fig. 3.8 a) is observed. We see that the discord depends on the initial squeezing. Initially a slow drop in discord is observed, leading to a local minimum for weakly squeezed states, but a global minimum for highly squeezed state. As the modulation is increased the discord approaches a higher level for weakly squeezed states and a lower level for highly squeezed states. At the same time in Fig. 3.8 b) we see that the quantum mutual information is monotonically increasing, so the initial drops must be due to more information being classical when the states go from pure to slightly mixed. One could imagine these correlations to be more robust to

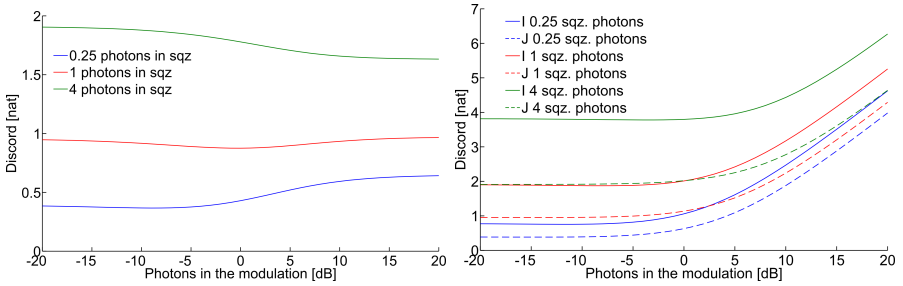

Figure 3.8: Theoretical comparison of the discord a) and informations I (solid) and J (dashed) b) for states containing fixed two-mode squeezing containing 0.25 (blue), 1(red) and 4 (green) photons on average and varied coherent modulation with $\det\gamma < 0$.

loss than any correlations without entanglement, hence we made the simulations shown in Fig. 3.9. We see that the combined state have higher discord for all attenuation than the same state with no EPR correlations and further it is more robust than the EPR states with no modulation from Fig. 3.5. However comparing to the coherent mixture with $\det\gamma > 0$, we see that the relative strength of the correlations after dissipation depends on the strength of the EPR correlations.

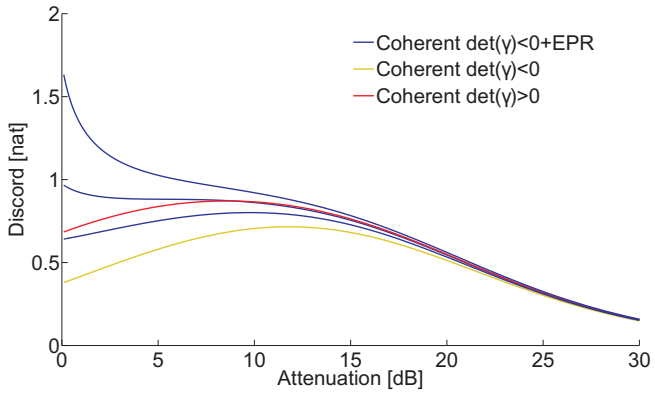

Figure 3.9: Theoretical comparison of the discord of coherent mixtures and coherent mixtures with EPR correlations. The three blue lines are with EPR correlations, from the bottom containing 0.25, 1 and 4 photons on average respectively and 20 dB of coherent modulation with $\det\gamma < 0$. For reference we plot the yellow line showing the performance of 20 dB of coherent modulation with $\det\gamma < 0$ and the red line 20 dB of coherent modulation with $\det\gamma > 0$.

3.4.5 Single-mode squeezing

Similarly to modulating EPR states we can also modulate squeezed states. There are many possible combinations but the one with same squeezing in both modes and $\det\gamma < 0$ seems particularly interesting. This state can be generated by amplitude squeezing two seeds, modulate the one along the squeezing direction and the other along the direction of the antisqueezing before coupling them on a beamsplitter. We made simulations for these states shown in Fig. 3.10.

We see that both I and J are higher than for the state with no squeezing, however their difference is no longer monotonic. It is not completely obvious why the shown dip emerges, however it relates to the size of the modulation relative to the squeezing (anti-squeezing).

3.5 Summary and outlook

Gaussian quantum discord is a measure of quantum correlations in Gaussian systems. We used Gaussian discord to quantify the quantum correlations of a bipartite entangled state and a separable two-mode mixture of coherent states. We experimentally analyzed the effect of noise addition and dissipation on the

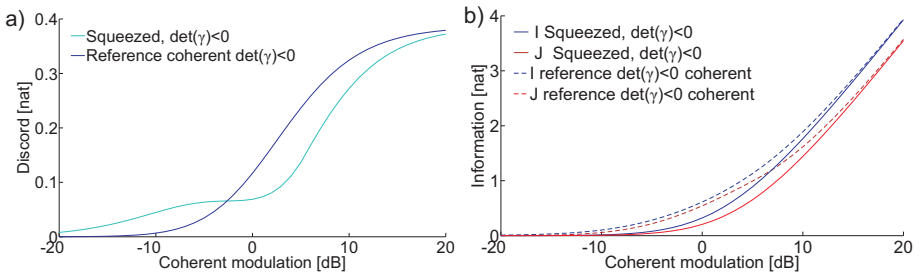

Figure 3.10: Theoretical comparison of the discord a) and informations I and J b) when both modes are 5.7 dB squeezed states and coherent modulation is added with $\det(\gamma) < 1$.

Gaussian discord of mixtures of coherent states and EPR states. We saw that the former noise degrades the discord while the latter noise can lead to an increase in discord for mixtures of coherent states. For the mixtures of coherent states we observe the transition to classical states with the corresponding near-death of discord by noisy evolution and the revival of the discord through dissipation.

Next we turned our attention to a wider range of simulations. We compare the robustness of the discord in EPR states and mixtures of coherent states and see that EPR states always carry more discord under energy constraint. We saw that phase conjugate mixtures of coherent states can have exactly the same properties except for a different discord, making them good candidates for test states. We added extra modulation to EPR-states testing the robustness of the resulting combined correlations to attenuation. We observed that although the resulting discord always was higher than for the $\det(\gamma) > 0$ mixture of coherent states, it could be both higher and lower than the $\det(\gamma) > 0$ mixture of coherent states depending on the strength of the entanglement in the system. Finally we observed non-monotonic behavior of the discord when adding modulation to two-mode squeezed separable states.

There are several candidates for protocols where the discord might be the best quantifier, and with the above toolbox of states for testing it should be possible to discriminate if a Gaussian protocol is discord based or not, before trying to do a detailed mathematical proof.

We have no doubt that both the separable and entangled quantum correlations will continue to attract much attention as they form the basis of quantum information technology. As an example we will see in the next chapter, that quantum correlations can be used to guarantee the security of secret communication. Inspired by quantum cryptography the difference between the Holevo bound and the quantum mutual information would be an interesting quantity to investigate in detail.

Chapter 4

Quantum key distribution

There is a tremendous demand for secure communication of data in commerce, finance and government affairs. Unconditional security is promised by the use of a one-time pad strategy where two parties, Alice and Bob, share a pre-established secret key which they use for encoding and decoding the message. The confidentiality of the communication therefore falls back on the generation of a secret key between Alice and Bob [1, 47]. Such a key can be generated with quantum key distribution which was first proposed by Bennett and Brassard in 1984 (BB84) for single photons and discrete variable measurements [21]. The technology has later been extended to also include coherent states and continuous variable measurements known as CV-QKD [22, 48–56].

A generic CV-QKD protocol between two trusted parties is initiated by Alice who prepares a distribution of Gaussian quantum states of light, e.g., coherent [22, 48–53, 56] or squeezed/entangled states [55, 57–61]. Alice transmits the states through a quantum channel to Bob who performs measurements on the continuous quadrature components of the light field using either a homodyne detector [22, 48, 49, 56] or a heterodyne detector [53] thus measuring conjugate quadratures either randomly or simultaneously, respectively. This results in a set of data that is partially correlated with Alice's data set which she obtained in the process of preparing the distribution of quantum states. Alternatively, a two-way quantum communication scheme can be formulated [54], but we will restrict our discussion to one-way quantum communication. To estimate the secrecy of the transmission, Alice and Bob compare a subset of their data using classical communication. Provided that the security threshold for channel loss and excess noise has not been crossed the resulting set of raw data can then be mapped onto a shared secret key using classical reconciliation and post-processing techniques [49, 62, 63].

There are two major hurdles in CV-QKD that limits the distance for secure communication. The first one is the presence of excess noise combined with high losses in the optical channel [22, 48, 49, 53, 56] and the second one is the limited classical reconciliation efficiency. For example, in the realistic CV-QKD scheme based on coherent states, the maximal secure distance is in theory limited to around 140 km if the channel excess noise is 4% of vacuum noise, the loss is 0.2 dB/km and the post-processing efficiency is 96.9% [63]. To enlarge the secure distance, one obvious strategy is to reduce the channel loss and noise, and to increase the post-processing efficiency. However, present CV-QKD systems are

already working with state-of-the-art optical channels and the post-processing efficiency is also reaching its limit. Therefore, to go beyond the currently achievable distances, a fundamentally different approach must be followed.

In this chapter we propose and, as a proof-of-principle, experimentally demonstrate two CV-QKD protocols based on entangled states and single mode squeezed states respectively, that are more tolerant to channel excess noise, channel loss and limited post-processing efficiency than the coherent state based protocols [1].

4.1 CV-QKD with modulated entangled states

The concept of the protocol is illustrated in Fig. 4.1. Alice prepares a Gaussian entangled state, and measures one of the modes using a homodyne detector that randomly detects the amplitude or the phase quadrature. This measurement projects the EPR state onto a Gaussian distribution of conditionally squeezed states [64]. Such alphabet of squeezed states could in principle be used to outperform the coherent state protocol under the condition of pure and strong entanglement [55]. To release these stringent requirements, we propose to enlarge the Gaussian distribution in phase space by a controlled modulation using two random and independent Gaussian variables. The final Gaussian distribution of states is then transmitted through a potentially lossy and noisy quantum channel the action of which may be ascribed to an eavesdropper (Eve). Finally, the states are measured by Bob who randomly measures one of the two conjugate continuous quadratures using homodyne detection.

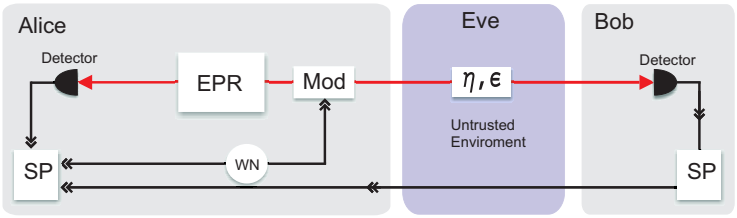

Figure 4.1: Conceptual diagram of our QKD protocol. Alice prepares a conditionally squeezed state by randomly measuring the amplitude or the phase quadratures of one mode of an EPR state using a homodyne detector. The conditionally squeezed state is modulated further by a modulator (Mod) fed with a Gaussian white noise (WN) source controlled by Alice. The homodyne data and the white noise data are stored for signal processing (SP) and the gain between them is optimized. The modulated conditionally squeezed state is transmitted through an untrusted quantum channel where Eve is allowed to perform any attack that mimics the channel transmission η and the channel excess noise ϵ. After the channel Bob performs quadrature measurements using a homodyne detector and the classical post-processing can begin.

After the transmission Alice holds two sets of data; one set obtained from the homodyne measurements, $\{x_{HD}\}$, and one from the Gaussian modulation,

[1] The work in this chapter has been a collaboration with Mikael Lassen and the theoreticians Vladyslav C. Usenko and Radim Filip from Palacký University, Olomouc, Czech Republic

$\{x_M\}$. To maximize the performance of the protocol, we suggest to weight the homodyne data with a gain factor, $g \in [0,1]$, and subsequently add the two sets to yield the optimized set: $A_x = \{x_M + g x_{HD}\}$. The optimal gain factor depends on the strength and the purity of the EPR state. In the limit of no squeezing Alice only keeps the data from the Gaussian modulation and thus the protocol reduces to the standard coherent state protocol [22, 48]. On the other hand for very high antisqueezing, $g = 1$ and the values of the resulting data set are equally constructed from the two subsets. However, in a real life scenario squeezing is limited and thus an intermediate gain will optimize the generation of a secret key. The rest of the classical part of the protocol follows the common recipe of the generic protocols.

4.1.1 Secret Key

After obtaining the two-mode covariance matrix the security analysis of our protocol follows the well established security proofs for the Gaussian CV-QKD protocols, which are based on the extremality of Gaussian states [65] and consequently the optimality of Gaussian collective attacks [66, 67] under certain symmetries of the protocol [68].

For collective attacks and using the classical technique of reverse reconciliation [22], the achievable key rate (in the asymptotic limit of an infinitely long raw key) is given by

$$I = \beta I_{AB} - \chi_{BE}, \tag{4.1}$$

where I_{AB} is the Shannon mutual information between the data of Alice and Bob, χ_{BE} is the Holevo bound on the information available between Bob and Eve and β is the post-processing efficiency [2].

The Shannon mutual information between Alice and Bob only comes from one quadrature and is calculated as [69]

$$I_{AB} = \frac{\mathrm{var}(A_x)}{\mathrm{var}(A_x|B_x)} = \frac{\mathrm{var}(A_x)}{\mathrm{var}(A_x) - \frac{\mathrm{cov}(A_x,B_x)^2}{\mathrm{var}(B_x)}} \tag{4.2}$$

where A_x is Alice's normalized data and B_x is Bob's normalized x-quadrature data.

The calculation of the Holevo bound is a bit more complicated. The Holevo quantity is expressed through the von Neumann entropies ($S(\cdot)$) in Eq. 2.58

$$\chi_{BE} = S(\sigma_E) - S(\sigma_{E|B_x}). \tag{4.3}$$

Hence we need to know the entropy of Eve's state and Eve's state conditioned on Bob's measurement. To obtain these quantities we define a theoretical preparation scheme [70–72] where the actual two-mode state of Alice and Bob is part of a pure multi-mode state [73]. This purification is generated by using pure sources and accounting for all modes. We therefore define a theoretical preparation scheme (see Fig. 4.2)) that can generate any two-mode Gaussian state between Alice and Bob as part of a pure four-mode state.

If untrusted noise is present in the system, Eve is assumed to be able to purify the system of Alice and Bob so that $S(\sigma_E) = S(\tilde{\sigma}_{AB})$ and $S(\sigma_{E|B_x}) =$

[2] Note that I in this chapter refers to the key rate, where it referred to the von Neumann mutual information in the chapter on Gaussian quantum discord.

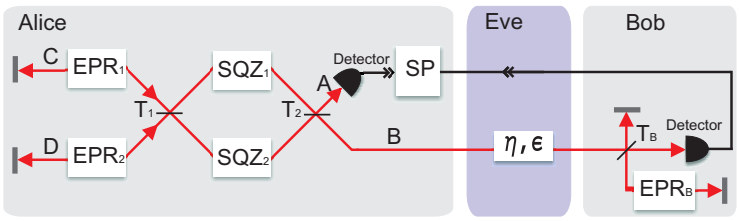

Figure 4.2: Purification scheme for an arbitrary Gaussian QKD protocol. Two quadrature squeezers (SQZ_1 and SQZ_2) are placed inside a Mach-Zehnder interferometer with beam splitters of transmittances T_1 and T_2 and fed with modes from two independent EPR sources (EPR_1 and EPR_2) . The resulting 4-mode state (A,B,C and D) is pure, while the six free parameters can be set so that the two modes A and B can simulate any Gaussian two-mode state (up to a local unitary transformation) including the states produced in our experimental setup. One mode of the state is measured by an ideal detector at Alice while the other travels through the channel which has transmission η and excess noise ϵ. Finally Bob's noisy detection is purified by placing a beamsplitter with an EPR input and a transmission mimicking his electronic noise, detection efficiency and the noise he adds to his data, before an ideal detector.

$S(\tilde{\sigma}_{AB|B_x})$, where $\tilde{\sigma}_{AB}$ is the pure state shared between Alice and Bob [49]. These covariance matrices we know and hence the von Neumann entropies can be calculated from the symplectic eigenvalues.

4.1.2 Theoretical results

To reach large distances for which key distribution can be attained, one must develop a protocol that maximizes the key rate in Eq. (4.1). We start by considering the standard coherent state protocol assuming unity post-processing efficiency. It is known that the key rate for this protocol can be maximized by using an infinitely large Gaussian modulation and by adding white noise to Bobs data which are obtained by homodyne detection [55]. Using the above mentioned analysis for collective attacks, we calculate the secure key rate and the maximally tolerable excess noise, and the results are illustrated by the solid curves in Fig. 4.3 a) and b) . These two curves represent the coherent state benchmarks. Employing the squeezed state protocol suggested in ref. [55] these benchmarks can be beaten but only for strongly squeezed states that is, 5.6 dB noise suppression below the shot noise limit as illustrated by the dotted curves in Fig. 4.3 a) and b).

Now by considering our protocol (Fig. 4.1), the key rate and the tolerable excess noise are increased even further as shown by the bold dashed lines in Fig. 4.3. Comparing the previous squeezed state protocol [55] with ours, we see that the maximal secure distance attainable for 3dB squeezed states is increased by a factor of about 19 and the required squeezing for surpassing the coherent state protocol is lowered from 5.6 dB to 0 dB for pure two-mode squeezed states. For highly impure two-mode squeezed states we need 3 dB of two-mode squeezing as shown with the dot-dashed curve. Our protocol thus has the remarkable property that any conditionally squeezed state improves the performance beyond the

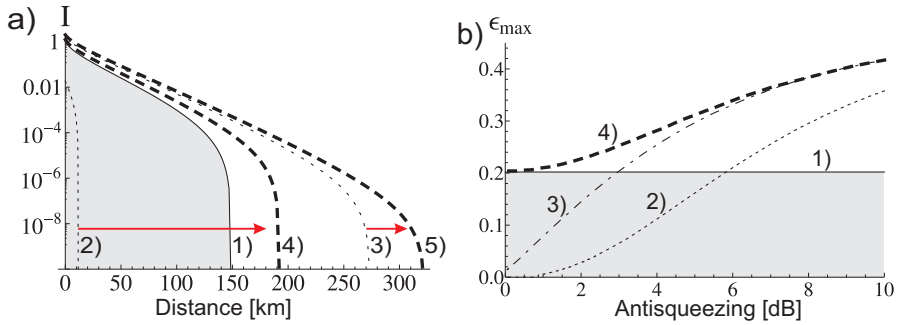

Figure 4.3: Theoretical comparison between the performance of different CV-QKD protocols. a) Secret key rate as a function of distance (corresponding to a loss of 0.2 dB per km) for a fixed excess noise of 0.1 SNU. 1) Ideal coherent state protocol with 100 SNU modulation. The shaded region illustrates the regime accessible with coherent state protocols. 2) and 3): Squeezed state protocol with 3 dB and 10 dB squeezing respectively (without additional modulation). 4) and 5): Our proposed protocol with 3 dB and 10 dB of squeezing respectively and 100 SNU modulation. For all protocols, the added noise to Bob's data is optimized and $\beta = 1$. b) Maximal tolerable channel noise versus the initial antisqueezed variance. The channel loss is set to 10 dB (corresponding to a distance of 50 km). 1) Ideal coherent state protocol with asymptotically large modulation. The shaded region illustrates the regime accessible with coherent state QKD. 2) Squeezed state protocol without additional modulation. 3) New combined squeezed state protocol with 100 SNU of coherent modulation without the gain. This is also the performance obtained for highly impure squeezed states. 4) Our proposed optimized protocol with 100 SNU coherent modulation and optimized gain factor. For all protocols, the added noise to Bob's data is optimized and $\beta = 1$.

optimized coherent state protocol. Moreover, another important feature of our protocol is that the squeezed states need not be pure; arbitrary mixedness can be tolerated as long as the state is conditionally squeezed. Therefore, the main resource for increased performance is conditional squeezing. We note however that the performance saturates for high degrees of squeezing (see. Fig.4.3 b).

4.1.3 Experimental setup

The experimental setup is sketched in Fig. 4.4. We start by generating EPR entanglement between two modes of light [64]. The quadrature of one of the EPR modes is measured by means of high efficiency homodyne detection at Alice's station. In addition to the measurement, we induce a random but known coherent modulation to the second EPR mode. After the channel we measure the second mode using a high efficiency homodyne detector at Bob's station, to access either the amplitude quadrature or the phase quadrature. We use laser light at 1064 nm for the seeds and local oscillators and 532 nm for the pump for the Optical Parametric Oscillators (OPOs), which are operated below threshold. The EPR state has 3.5 dB $\pm$0.2 dB of two-mode squeezing and 8.2 dB $\pm$0.2 dB of antisqueezing and the coherent modulation depth is sequentially varied between 0 and 15 dB. All measurements are performed at the sideband frequency of 4.9 MHz with a bandwidth of 90 kHz. The system is initially calibrated to ensure that the correlation between conjugate quadratures of Alice is negligible and that the quadratures of Alice are in phase with Bob.

The experiment was carried out sequentially for conjugate quadratures; the amplitude quadrature was first conditionally squeezed, displaced and measured, and the procedure was then repeated for the phase quadrature. We add the homodyne and modulation data with an optimized gain. For technical reasons we multiply the modulation data with the inverse of the gain factor. This results in two large data strings, one for Alice and one for Bob which are strongly correlated as shown for three different modulation depths in Fig. 4.5 a1)-a3). The correlations arise partly from the quadrature entanglement and partly from the coherent modulation. From the correlated data we compute the covariance matrices as illustrated in Fig. 4.5 b1)-b3), from which we can estimate the security limits for our system.

4.1.4 Data analysis and results

The measurement and the subsequent data processing (including numerical gain optimization) resulted in a set of covariance matrices for different values of modulation. The security analysis was carried out according to the above described purification method. Since the explicit trusted mode structure of the experimentally obtained states was not known, the measured covariance matrices were purified using the Bloch-Messiah reduction theorem [73] as illustrated in Fig. 4.2. For each of the measured covariance matrices the 4-mode pure state (ABCD on Fig. 4.2) was constructed and used to calculate the Holevo quantity and the resulting secure key rate.

In parallel, the theoretical estimation of the expected protocol performance was calculated from the experimental parameters of our setup. The covariance matrices were constructed from the experimentally measured EPR states. All the respective transmittances and efficiencies were applied in both EPR modes

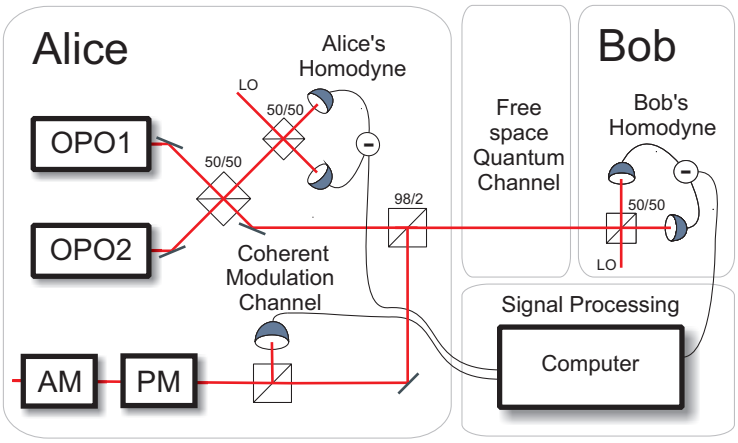

Figure 4.4: Experimental setup. A squeezed state is generated in each of the two optical parametric oscillators (OPOs), operated below threshold. The squeezed states interfere at a beam splitter to form a two-mode squeezed state. The amplitude or the phase quadrature of the one mode is measured by Alice's homodyne detector. The other mode is carefully phase locked to a coherently modulated auxiliary mode. The auxiliary state is generated using a phase modulator (PM) and an amplitude modulator (AM), each of which are driven by a white noise generator. Alice acquires information about the modulation by measuring a part of the auxiliary state. The coherent state is purified by the highly asymmetric beamsplitter all of this in order to minimize the harmful preparation noise [70]. The modulated and conditionally squeezed state is transmitted through the channel to Bob's homodyne detector where one of the conjugate quadratures is measured. The resulting measurement outcomes are fed via a fast AD card to a computer for signal processing.

(as beamsplitter transformations) and the coherent modulation was added atop. The resulting covariance matrices were tested against given channel transmittance and excess noise.

In the laboratory the channel transmission is 95% and the excess noise can be continuously varied by unbalancing the generated data at Alice and Bob. As an example we set the excess noise to 0.45 shot noise units (SNU) and the total modulation depth to 23.4 SNU. For these settings of the experiment we generate a raw key with a rate of 0.004 ± 0.001 bit per state. We note that neither the coherent state based protocols nor the standard squeezed state based protocol (with 3.5 dB squeezing) could have generated a key in such a channel.

We now investigate the security performance of our protocol in longer channels based on the experimentally measured covariance matrices assuming perfect post-processing and channel estimation. The matrices are used in a model that includes the trusted losses and noise sources of the detectors, and in which arbitrary channel loss and excess noise can be simulated. As an example we assume a channel transmission of 10% and find the tolerable excess noise for six different realizations of the covariance matrices illustrated on Fig. 4.6. Finally, on Fig. 4.7 we plot the maximum distance and loss as a function of the tolerable

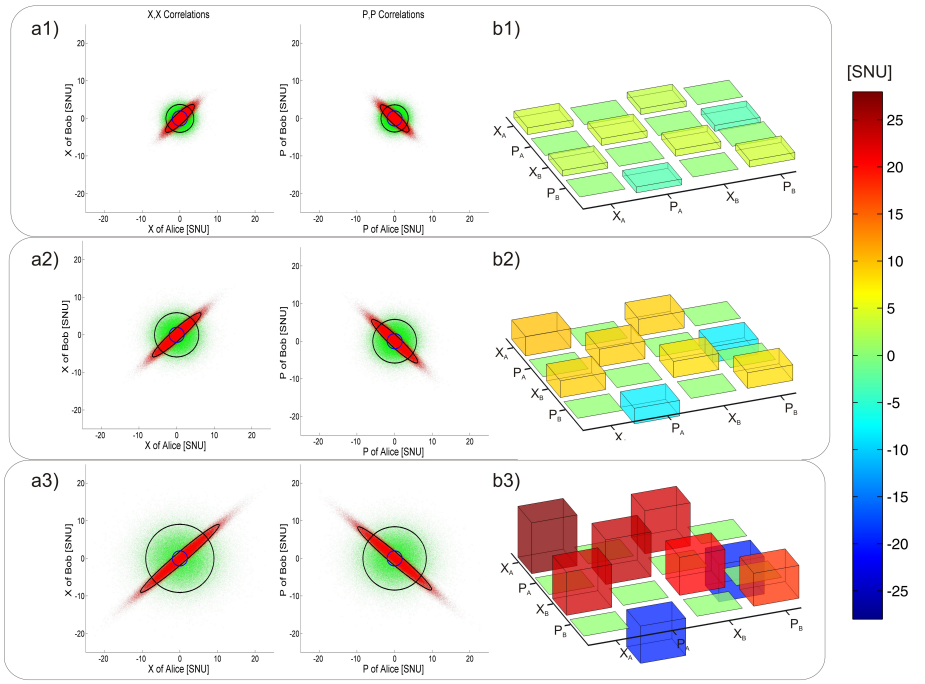

Figure 4.5: QKD measurement results. a1-3) The red points represent the normalized and weighted quadrature data of Alice and Bob for three different depths of coherent modulation 1) 0 SNU, 2) 3.6 SNU and 3) 23.8 SNU all having 3.6 SNU modulation from the EPR source. These correlated data are contrasted with a set of uncorrelated data points (green) with identical total energy. Solid black ellipse and outer circle correspond to two standard deviations of these two respectively, inner blue circle is two standard deviations of shot noise. b1-3) Illustrations of the covariance matrices for the three modulation depths.

noise associated with the experimentally realized covariance matrix in Fig. 4.5 b3). We clearly see that by combining squeezed states with coherent modulation we beat the performance of any coherent state protocol (limited to the shaded region). The supremacy of the squeezed state protocol relative to the coherent state protocol is best seen by equalizing the amount of energy used in the two protocols. In this case the states entering the channel are identical and Eve cannot tell the difference between the two protocols. The relative improvement is illustrated by the dot-dashed curve relative to the dashed curve in Fig. 4.6.

4.1.5 Discussion

In our implementation we measure the quadratures sequentially, which is in principle not secure. The conjecture from earlier protocols is that some sort or switching between the conjugate variables has to take place. Surprisingly Alice does not have to change anything (neither in an EPR implementation nor in a direct squeezing implementation). If she knows what she sends into the channel (by calibrating her system) there is no reason for Alice to change anything in

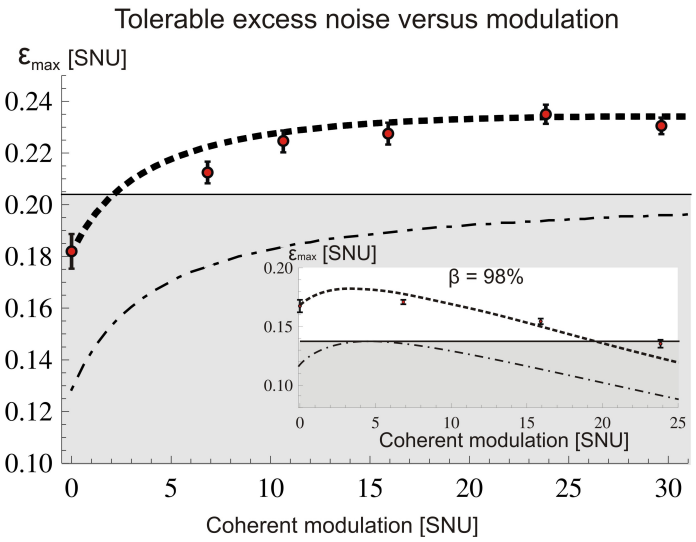

Figure 4.6: Tolerable excess noise as a function of the modulation depth for a simulated transmission of $\eta = 0.1$. The uncertainty represent the actual measurements with compensation for $85 \pm 5\%$ quantum detection efficiency as the dominating source of uncertainty. The theoretical estimates for the ideal coherent state protocol and our protocol with the experimental parameters are given by the solid and dashed curves, respectively. For comparison, we also include the performance of the coherent state protocol with an energy identical to the energy of the two-mode squeezing protocol (dot dashed curve). The shaded region illustrates the regime accessible with coherent state QKD. The inset is the same as the main figure but with limited post-processing efficiency $\beta = 98\%$.

order to estimate the channel parameters. The easiest way to estimate the channel is for Bob to measure part of each quadrature with an unbalanced dual homodyne detector. Hence no movable parts are needed and the protocol can if needed approach homodyne detection of one quadrature only. However as some amount of excess noise is more harmful to Eve than to Alice and Bob pure homodyne detection is not a goal in itself. Rather Bob can optimize the channel estimation or the added noise directly by the balance in the dual homodyne detector.

To use the framework of the security proof we need one covariance matrix at Alice's side. Since we have data both from the modulation and the EPR state we need to merge these data sets. The first way we considered doing this was to modulate both modes of the EPR state, however it seemed inefficient for Alice first to modulate her mode and then measure it without it having been to the channel. This was clearly seen from the low (pure) squeezing limit, were it would simply correspond to adding one unit of vacuum noise to Alice's data. We hence decided to modulate Bob's mode only, but then we had the task of how to add the two sets of data at Alice's side. Adding them directly gives

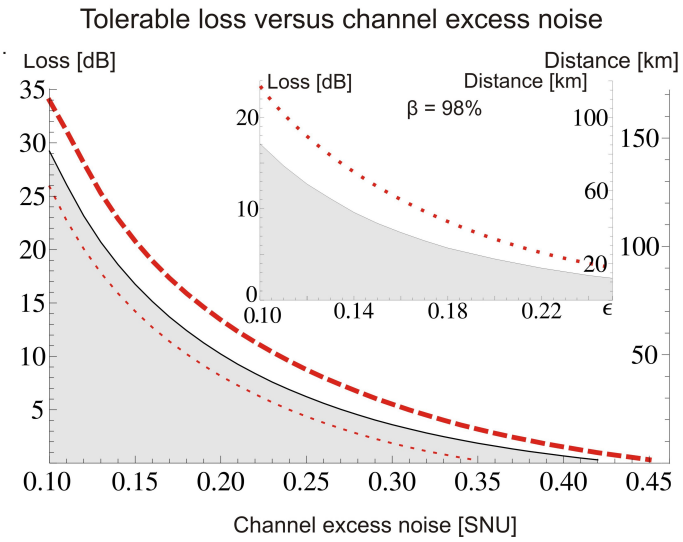

Figure 4.7: The maximally tolerable loss as a function of the channel excess noise. The thick dashed line is for the data set presented in Fig. 4.5 a3) and b3), the solid curve is for the ideal coherent state protocol. The dotted curve corresponds to the two-mode squeezing protocol without additional modulation presented in matrix b1). The insert is the same as the main figure, the dotted curve being the data set presented in Fig. 4.5 a1) and b1) but with limited post-processing efficiency $\beta = 98\%$.

the same problems in the low squeezing limit so we added them with the gain factor. It might be possible for Alice and Bob to get more mutual information by combining the information differently.

In the analysis above we have assumed perfect classical post-processing (corresponding to $\beta = 1$). However, the key rate of real world implementations of CV-QKD is currently limited by the inefficiency of the yet developed classical error codes [63, 74]. We have therefore considered the effect of imperfect post-processing on our protocol corresponding to a security analysis with $\beta < 1$. The results of this analysis for an optimistic $\beta = 0.98$ are illustrated in the insets of Fig. 4.6 a) and Fig. 4.6 b). In figure 4.8 we show the performance of our data as a function of β, the lower the β factor the lower modulation is optimal.

It is evident from the figures that despite inefficient post-processing, our squeezed state protocol remains superior to the coherent state protocol, and remarkably, it is seen that the relative improvement has increased. We also note that the optimal performance occurs for a finite modulation depth.

4.2 β robust protocol

The major issue with the β- factor is when both I_{AB} and χ_{BE} are big relative to their difference. Then, even though the ideal key rate is relatively high, the effective key rate can be zero. This primarily occurs for big modulations. For

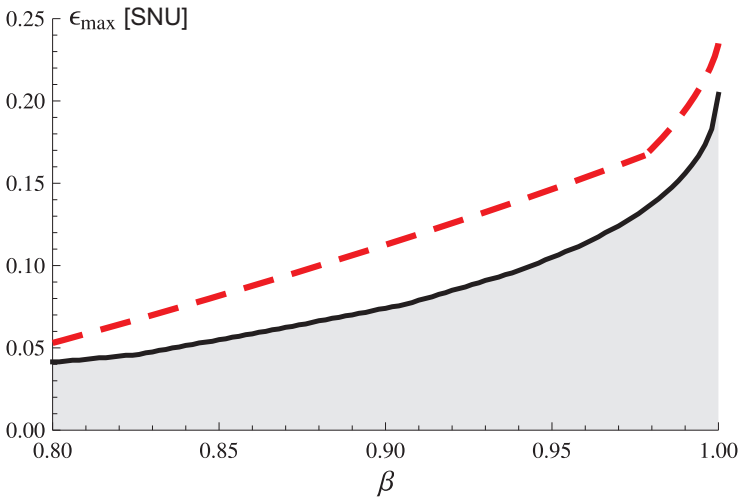

Figure 4.8: Tolerable excess noise as a function the post-processing efficiency β assuming a channel transmission of $\eta = 0.1$. The dashed line corresponds to the performance of the experimentally obtained states; the solid line gives the limit set by the optimally modulated coherent states. The kink of the dashed line is caused by changing to a data set with lower modulation.

smaller modulation, the ratio of I_{AB} to χ_{BE} grows so given the efficiency of the reconciliation there will be an optimum modulation. Improving the classical algorithms is one approach to improve this part of the performance. In [74] the reconciliation efficiencies seems to be close to or above 95% for small signal to noise ratios at Bob's side. A more physical approach to reduce the importance of the problem is mentioned in [69]. The idea is to use a fixed squeezing of a single quadrature and perform modulation in this squeezed quadrature. This modulation can be smaller than the antisqueezing and when the modulation is so small that the total variance is one, the Holevo bound between Eve and Bob goes to zero in the purely lossy channel. This surprising result means that the optimal modulation always will be bigger than or equal to one minus the squeezed quadrature. While previous protocols have aimed at maximizing the absolute ideal key rate given a channel, this protocol aims at minimizing the Holevo bound on Eve's information.

4.2.1 Experiment

We have performed the first experiments on this protocol. The experimental source consists of a single modulator and a single squeezer shown in Fig. 4.9. Unlike the previous experiment in this chapter, the modulation of interest is relatively low. This means that the transfer function of the modulators is of little importance, so the signal of the modulation can be taken directly from the function generator. We have experimentally implemented the purely lossy quantum channel as a variable beamsplitter. After the channel we perform homodyne detection measuring the x and the p quadrature sequentially on both output modes, assigning one to Bob and one to Eve. These measurement hence

give a two-mode density matrix and we have another mode coming from Alice.

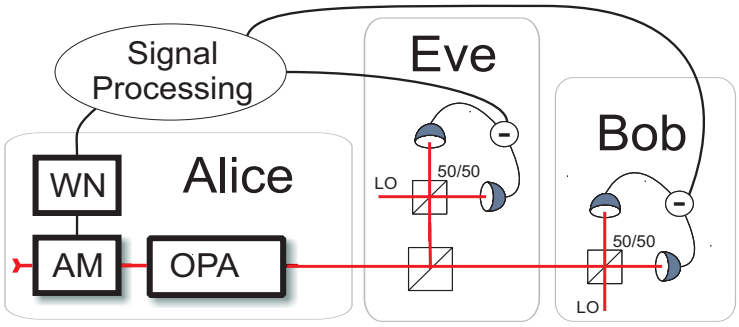

Figure 4.9: The experimental setup. WN white noise.

4.2.2 Data analysis

We normalize the data of Bob and Eve to their respective shot noise. The data of Alice is classical, in the sense that it has very high energy, but limited signal to noise ratio. To treat this in the covariance matrix formalism we normalize the data to a variance of 100 SNU which saturates the key rate of Bob and Alice. Apart from this the calculation of the key rate proceeds as in the previous section.

4.2.3 Results

Using our experimental source and attenuation we obtain the Holevo bound shown Fig. 4.10. The effect is highly pronounced. Eve's information simply drops towards zero when the total variance of Alice's squeezed quadrature with modulation reaches 1 SNU being higher for both higher and lower modulations.

By subtracting this quantity from the mutual information of Alice and Bob we get the key rate shown in Fig. 4.11. We show both the ideal key rate and a very conservative key rate with a $\beta = 0.75$.

Due to the low Holevo bound of the data just around -3dB of modulation (-3dB modulation plus -3dB shot noise) we see the that the key rate scales linearly with β hence being the most robust protocol obtained to date. We note that although more squeezing would give a slightly higher key rate the scaling with β stays the same and hence only what corresponds to a slightly higher optimal modulation is gained. This means that realistic squeezing sources suffice to implement the protocol.

We see that the ideal key rate also drops for higher modulation which is caused by limited signal to noise ratio of the direct modulation. This can be circumvented as was done in the first protocol if higher modulations are desired.

4.2.4 Further analysis

These results are basically the raw data. To proceed we have to consider what the highest uncertainties are, simulate the theory, figure whether we should

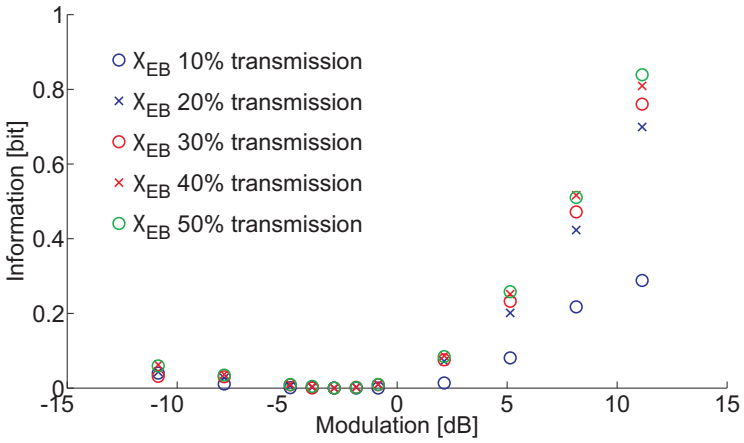

Figure 4.10: The Holevo bound as a function of modulation depth for channel transmission of $50\%, 40\%, 30\%, 20\%$ and 10% (transmission estimated in lab, not from the covariance matrix).

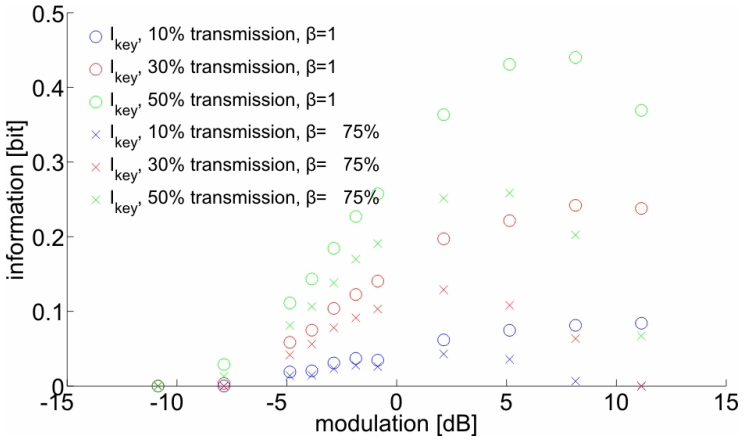

Figure 4.11: The key rate as a function of modulation depth for channel transmission of $50\%, 30\%$ and 10%. Circles indicate $\beta = 1$ and crosses $\beta = 0.75$. (Transmission estimated in lab, not from the covariance matrix)

compensate for Eve's detection efficiency and so forth. Further simulations including channel excess noise would be interesting and it would also be interesting to show the full potential of the protocol.

4.3 Concluding remarks

4.3.1 Measures in QKD

To optimize the information gained over Eve it would be useful to be able to quantify the exact performance of a given type of states. We make these com-

parisons using energy constraints and the key rate. For Gaussian states energy constraints work similar to truncation of the Fock-space for discrete variables. In the corresponding figures 4.3 a), b) 4.6 a) and b) we see that the performance of the different states do not cross, in contrast to earlier comparisons in e.g [55]. It might be possible to find crossing states among the states asymmetrical in phase space.

Finding more stringent and direct quantifiers is an open question. Intuitively the measure has to quantify that the states are hard to copy or clone and yet carry much extractable information. EPR-measures have these properties, however entanglement is not the direct resource as was first experimentally demonstrated in [22].

The discord could be another candidate. States with zero discord cannot be used for QKD as they can be copied noiselessly. However the discord does not work as the direct resource. As we mention entanglement is not needed to increase the performance beyond the coherent states bound, rather single mode squeezing can do the same or better. The regime of discord greater than one can only be reached with entanglement thereby giving a contradiction.

4.3.2 Summary

We have addressed two QKD protocols based on continuous variable squeezed states of light. The first protocol is based on entangled states. The requirement on the purity of the entangled states is relaxed compared with previous protocols. We find that the key rate as well as the robustness against channel noise is improved for any degree of conditional squeezing compared to the idealized and optimized coherent state protocol. We experimentally demonstrate this by generating the first raw key in channel where the coherent state protocol could not work.

The second protocol focuses on the robustness to the reconciliation efficiency. We experimentally demonstrate that by weakly modulating a single mode squeezed state we completely decouple a potential eavesdropper in the purely lossy channel. We show that using this protocol it is easy to reach the 10dB loss benchmark even with a highly limited reconciliation efficiency. Moderate squeezing suffices so in future commercial implementations miniaturized waveguide cavities could be used to make on chip squeezed state QKD.

4.3.3 Outlook

One way forward for Gaussian QKD and QKD in general is to make quantum repeaters which have the purpose of distributing entanglement over long distances using (non-Gaussian) entanglement distillation and entanglement swapping [1]. This would allow for the teleportation of the states hence changing the scaling of the loss and excess noise of the physical channel.

Seen from the quantum information perspective one-way QKD is not using the full potential of the states. If it was possible to use the von Neumann mutual information much greater information would be available. In the two-way protocols one mode of an EPR state is sent to Bob, who modulates it or measures it and then send either it or a new state back to Alice. The EPR mode suffers twice the loss and noise of the channel but a two-mode rotation on the returned state allows Alice to use part of the von Neumann mutual

information. This protocol still needs some development, in the form of security proof and implementation, however it seems like a possible way forward [54]. Comparisons of EPR states, mixtures of coherent states and phase conjugate mixtures of coherent states as resource states in the two-way scenario would be interesting.

Chapter 5

Quantum polarization

This chapter is dedicated to the task of illustrating and quantifying the polarization of quantum states. The task differs from the classical counterpart partly because of the interest in the higher moments of the distributions and partly because of the discreteness of the photon number especially near the vacuum state. It is structured as follows; First we will introduce the concepts of polarization measures in quantum optics and the Poincaré sphere. We will define and experimentally illustrate a second order polarization measure $\mathbb{P}_2$ from the work [75], which is based on the variance of the Stokes operators. We will move on to defining and experimentally illustrating a first order polarization measure $\mathbb{P}_1^{\text{res}}$ which resolves the polarization in the excitation manifolds thereby giving a better polarization measure [1]. Next, we will define a second order manifold resolved polarization measure $\mathbb{P}_2^{\text{res}}$ and experimentally illustrate the transition from small polarization states to highly excited states. In this section we will also introduce the SU_2 Wigner functions which expand the view of the Poincaré sphere [2].

5.1 Introduction

Classical polarization has numerous applications. To mention a few, it is used in thin-film ellipsometry [76], near-field microscopy [77], remote sensing [78] and light scattering [79]. When implementing optical quantum information protocols using the polarization rotations is a convenient way to make single mode phase rotations and two mode rotations such as the variable beamsplitter. In recent years, the concept of quantum polarization has further found a footing in quantum optics and in quantum information science where the information is efficiently encoded in the polarization degree of freedom. This has lead to the demonstrations of polarization entanglement [80], teleportation of the quantum polarization [81] and quantum key distribution based on quantum polarization encoding [82, 83]. The observables giving rise to quantum polarization are the

[1] This work is a collaboration with Christian Kothe and Gunnar Björk from School of Engineering Sciences, Royal Institute of Technology (KTH), Roslagstullsbacken 21, SE-106 91 Stockholm, Sweden

[2] This work is a collaboration with Christian R. Müller from Max-Planck-Institute for the Science of Light Erlangen, Germany

Stokes operators which we have already encountered in Sec. 2.0.5 as the generators of two-mode rotations.

5.1.1 Poincaré sphere

In classical optics a sphere with radius S_0 drawn in the space spanned by the Stokes parameters is called a Poincaré sphere. For fully polarized light modes the spatial Stokes vector ($\mathbf{S} = \{S_1, S_2, S_3\}$) points to some point on this sphere. For partially polarized light the Stokes vector wont reach the surface of the sphere. The polarization rotations Eq. 2.24 simply rotate the direction of this vector, keeping the length fixed.

In quantum optics the Poincaré sphere can also be drawn with mean radius $\langle \hat{S}_0(\hat{S}_0 + 2)\rangle$, see e.g [84]. The states cannot be represented by a point because of Heisenberg's uncertainty relation. Rather the moments of the distribution or the probability amplitude should be plotted. This works both for states where the photon number is well defined, like the single and two photon states, and for the states with one large excitation where the discreteness of the photon number vanishes. In between the picture does not give the full detail of the state as several of the discrete levels are excited with different distributions. We will return to this topic later in this chapter.

5.1.2 The unpolarized states and $\mathbb{P}_1^{\mathbf{sc}}$

Defining the degree of polarization for quantum states has received a lot attention. The definition of the unpolarized state is clear though. It is the states which are invariant under the polarization rotations [85]. For the Gaussian states this means the two-mode vacuum and the two-mode thermal states with equal photon numbers in the two modes.

Classically, the degree of polarization is a simple expression of the mean values of the Stokes parameters [86] which can be straightforwardly measured [87]. In quantum optics the first approach to generalize this measure was simply to replace the Stokes parameters by Stokes operators [88–90].

$$\mathbb{P}_1^{\mathrm{sc}} = \frac{\sqrt{\langle \hat{S}_1\rangle^2 + \langle \hat{S}_2\rangle^2 + \langle \hat{S}_3\rangle^2}}{\langle \hat{S}_0\rangle}. \tag{5.1}$$

The 1 in $\mathbb{P}_1^{\mathrm{sc}}$ refers to the measure considering the first moment of the Stokes vectors and sc refers to semi-classical. It was soon realized that this measure is insufficient to characterize the degree of polarization for many quantum states. States with average photon numbers much smaller than one could appear completely polarized even though the vacuum is invariant under the polarization rotations. States where the different photon number contributions points in different directions on the Poincaré sphere could appear completely unpolarized even though when knowing the total photon number the state would be completely polarized. Furthermore as the measure only considers the first moment it is insufficient to characterize polarization phenomena hidden in the higher moments.

5.1.3 An alternative measuring strategy

Measuring the polarization is another highly discussed problem. For few photon states single photon counters have been used. The promise of photon number resolving detectors (PRND) would allow to measure higher photon number states. However for the polarization squeezed states one of the Stokes operators is highly excited [87]. On the one hand the excitation allows one to perform Stokes based homodyne detection and to write up a canonical commutation relation for the two weakly excited Stokes operators. On the other hand it is impossible to measure, even in the near future with PRND's as the highly excited mode would saturate the detector. This leaves a gap in which many experimentally accessible continuous variable quantum states reside. For these states the mean photon number is too big for photon counters, but the excitation is too small to function as local oscillator in a Stokes homodyne measurement. In this chapter we explore the polarization of weakly excited squeezed and displaced states to fill the gab between the two regimes by using homodyne detection with a separate local oscillator.

A sketch of the experimental setup used in this chapter is shown in Fig. 5.1. To form the two-mode state, the displaced and squeezed outputs from the OPAs are combined on a polarizing beam splitter.

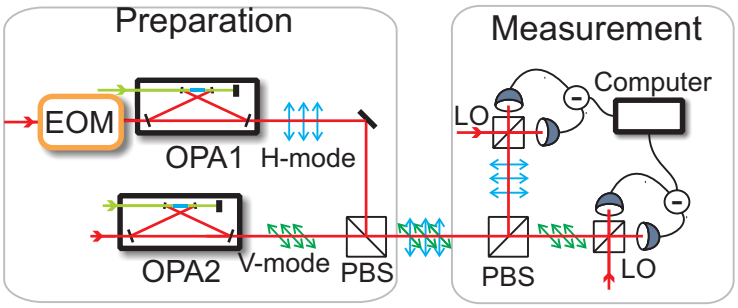

Figure 5.1: Setup for the production of the states in Eq. (5.6). Abbreviations: EOM electro optical modulator. H horizontal. V vertical. PBS polarization beamsplitter. LO local oscillator.

In contrast to previous realizations on CV polarization quantum states, we solely define our state to be residing at a sideband frequency of 4.9 MHz. Such a definition of the polarization state enables us to investigate a large variety of different polarization states from vacuum states to a relatively high excitation. We measure each mode, H and V, by splitting the polarization state on a polarizing beam splitter and using two homodyne detectors. The measured currents of the homodyne detectors are sampled at 500 kHz with a frequency bandwidth of 90 kHz, and subsequently sent to a computer for analysis.

5.2 Defining and illustrating $\mathbb{P}_1^{\mathrm{res}}$

In this section, we suggest a new and simple first order measure of quantum polarization and implement it experimentally. However, in contrast to the semi-classical measure $\mathbb{P}_1^{\mathrm{sc}}$, the new measure accounts for the polarization in each

excitation manifold which leads to a better characterization of the quantum polarization.

$$\mathbb{P}_1^{\text{res}}(\hat{\rho}) = \sum_{N=1}^{\infty} p_N \frac{\sqrt{\langle \hat{S}_{1,N}\rangle^2 + \langle \hat{S}_{2,N}\rangle^2 + \langle \hat{S}_{3,N}\rangle^2}}{\langle \hat{S}_{0,N}\rangle}, \tag{5.2}$$

where $p_N = \text{Tr}(\hat{\mathbb{I}}_N\hat{\rho})$, $\hat{\rho}_N = (\hat{\mathbb{I}}_N\hat{\rho}\hat{\mathbb{I}}_N)/p_N$, $\langle \hat{S}_{j,N}\rangle = \text{Tr}(\hat{S}_j\hat{\rho}_N)$, and $\hat{\mathbb{I}}_N = \sum_{m=0}^{N} |m, N-m\rangle\langle m, N-m|$, so that $\hat{\rho}_N$ is the normalized N-photon projection of the state's density matrix. The polarization degree is quantified by a weighted sum of the semi-classical degree of polarization in each excitation manifold of the state (except for $N = 0$). In other words, every excitation manifold is treated separately.

The measure can be slightly simplified from this pedagogic form and is easily calculated as

$$\mathbb{P}_1^{\text{res}}(\rho) = \sum_{N=1}^{\infty} \frac{\sqrt{\langle \hat{S}_{1,N}\rangle^2 + \langle \hat{S}_{2,N}\rangle^2 + \langle \hat{S}_{3,N}\rangle^2}}{N}. \tag{5.3}$$

As is clear from the definition, $\mathbb{P}_1^{\text{res}}$ coincides with $\mathbb{P}_1^{\text{sc}}$ when the number of photons is a fixed quantity. The two definitions also become approximately equal for classical-like states such as coherent states with $\langle \hat{S}_0\rangle \gg 1$. For many other states the two definitions give different results, and in the following we argue that $\mathbb{P}_1^{\text{res}}$ gives a better assessment of the polarization properties of quantum states than $\mathbb{P}_1^{\text{sc}}$.

The new measure is in principle directly detectable, since $\hat{S}_0$ commutes with all other Stokes operators, the Stokes vectors per excitation manifold and thus $\mathbb{P}_1^{\text{res}}$ can be directly accessed by using a proper waveplate configuration, a polarizing beam splitter and two photon number resolving detectors (PNRDs). Such detectors are currently capable of efficiently detecting more than 6 photons and due to the rapid progress in developing such detectors more advanced versions with increased optical power range might soon become available [91].

5.2.1 Theoretical investigation of $\mathbb{P}_1^{\text{res}}$

First we consider a two-mode state in which one of two orthogonal polarization modes is vacuum whereas the other one is a coherent state; $|\Psi(\alpha)\rangle = |\alpha\rangle_H \otimes |0\rangle_V$, where $\alpha = ae^{i\phi}$ is the complex amplitude of the coherent state ($a \in \mathbb{R}_0^+$, $\phi \in [0; 2\pi)$). For this state, the semi-classical degree of polarization is unity, $\mathbb{P}_1^{\text{sc}}(|\Psi(\alpha)\rangle) = 1$, for all values of α except $\alpha = 0$. On the other hand, using the new measure we find

$$\mathbb{P}_1^{\text{res}}(|\Psi(\alpha)\rangle) = 1 - e^{-|\alpha|^2}. \tag{5.4}$$

which is continuous for all α; $\mathbb{P}_1^{\text{res}}(|\Psi(\alpha)\rangle) \to 0$ when $\alpha \to 0$, and for large amplitudes, $\mathbb{P}_1^{\text{res}}(|\Psi(\alpha)\rangle) \to 1$ when $|\alpha| \gg 1$. Therefore, the classical and quantum limits, respectively corresponding to large and small amplitudes, are smoothly connected. $\mathbb{P}_1^{\text{res}}(|\Psi(\alpha)\rangle)$ is illustrated in Fig. 5.2 by the solid line, $\mathbb{P}_1^{\text{sc}}(\hat{\rho})$ is shown by the dotted line.

Eq. (5.4) can be easily generalized to any two-mode coherent states, $|\alpha\rangle_H|\beta\rangle_V$, which after an appropriate transformation can be written as a one mode coherent state, $|\alpha'\rangle|0\rangle$ in some other polarization basis with $|\alpha'|^2 = |\alpha|^2 + |\beta|^2$. The

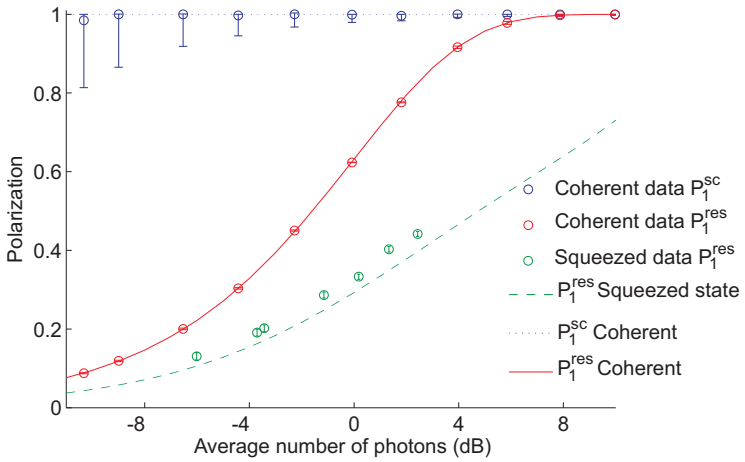

Figure 5.2: Comparison between $\mathbb{P}_1^{\rm res}$ and $\mathbb{P}_1^{\rm sc}$ as a function of the average photon number for the states $|\Psi(\alpha)\rangle_H|0\rangle_V$ and $|\psi(\xi(r))\rangle_H|0\rangle_V$ as defined in the text. The lines represent theoretical predictions while the circles indicate experimental values, see next subsection for experimental description.(-8 dB= 0.16 photons, 0 dB =1 photons, 8 dB=6.3 photons.)

degree of quantum polarization of any two-mode coherent state is therefore given by Eq. (5.4) with $|\alpha|^2 \to |\alpha|^2 + |\beta|^2$.

Next we consider the degree of quantum polarization for single-mode squeezed states; $|\varphi(\xi,\alpha)\rangle = \hat{D}(\alpha)\hat{\mathcal{S}}(\xi)|0\rangle_H \otimes |0\rangle_V$ where $\hat{D}$ is the displacement operator and $\hat{\mathcal{S}}(\xi) = \exp\left[(\xi^*\hat{a}^2 - \xi\hat{a}^{\dagger 2})/2\right]$ is the squeezing operator with $\xi = re^{i\theta}$, $r \in \mathbb{R}_0^+$, $\theta \in [0; 2\pi)$ being the squeezing parameter. For this state we find $\mathbb{P}_1^{\rm sc}(|\varphi(\xi,\alpha)\rangle) = 1$, whereas

$$\mathbb{P}_1^{\rm res}(|\varphi(\xi,\alpha)\rangle) = 1 - \frac{1}{\cosh(r)} \exp\left[-|\alpha|^2 - \frac{1}{2}\left(\alpha^{*2}e^{i\theta} + \alpha^2 e^{-i\theta}\right)\tanh(r)\right]. \quad (5.5)$$

which is illustrated in Fig. 5.2 as a function of the average number of photons for a squeezed vacuum state (that is, $\alpha = 0$ and $\langle n_{sqz}\rangle = \sinh(r)$). We clearly see that $\mathbb{P}_1^{\rm res}$ differs significantly from $\mathbb{P}_1^{\rm sc}$ for basically all practical squeezing values. We note that for the generalized squeezed state in (5.5), the degree of polarization also depends on relative phase between the squeezing angle, θ, and the phase of the displacement, ϕ: It is maximized for amplitude squeezing ($\theta - 2\phi = 0$) and minimized for phase squeezing ($\theta - 2\phi = \pi/2$).

Overall we see that $\mathbb{P}_1^{\rm res}$ behaves as a first order polarization measure should, giving a polarization equal to $1 - \rho_{0,0}$ for all single mode states.

Finally we consider the generalized pure two-mode squeezed state

$$\hat{D}(\alpha_H)\hat{\mathcal{S}}(\xi_H)|0\rangle_H \otimes \hat{D}(\alpha_V)\hat{\mathcal{S}}(\xi_V)|0\rangle_V, \quad (5.6)$$

and plot the degree of polarization (both $\mathbb{P}_1^{\rm sc}$ (upper row) and $\mathbb{P}_1^{\rm res}$ (lower row)) in Fig. 5.3 for three different states. In Fig. 5.3 (left column), a two-mode vacuum state ($\alpha_H = \alpha_V = 0$) is illustrated for different squeezing degrees. Both measures exhibit zero polarization degree for equal squeezing parameters whereas for different squeezing parameters, $\mathbb{P}_1^{\rm res}$ gives lower values than $\mathbb{P}_1^{\rm sc}$.

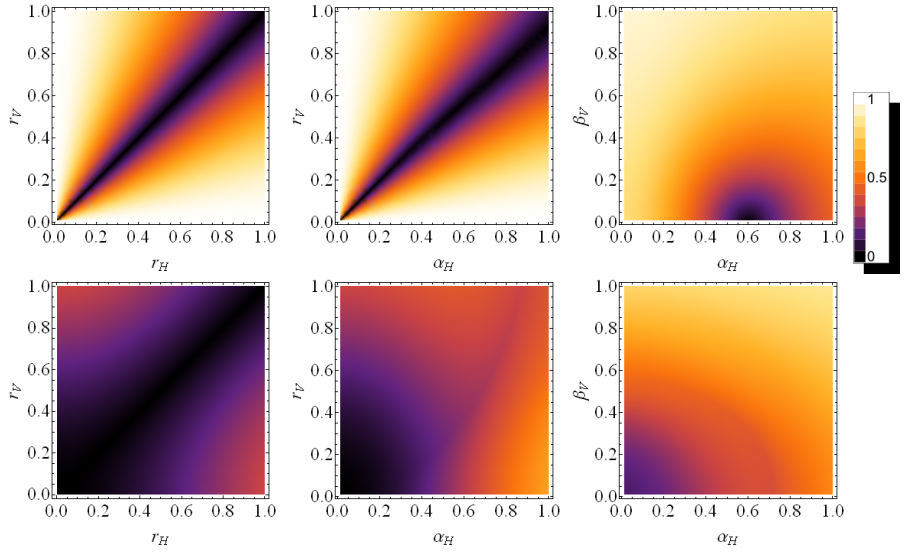

Figure 5.3: Theoretical plots of the degree of polarization. We plot the state $|\psi(\xi_H(r_H), \xi_V(r_V))\rangle$ (left column), $|\alpha_H\rangle_H \otimes |\psi(\xi_V(r_V))\rangle_V$ (middle column) and $\hat{D}(\alpha_H)\hat{\mathcal{S}}(0.2)|0\rangle_H \otimes \hat{D}(\beta_V)\hat{\mathcal{S}}(0.6)|0\rangle_V$ (right column). The upper plots show $\mathbb{P}_1^{\text{sc}}$, whereas the lower plots show $\mathbb{P}_1^{\text{res}}$.

If we now set $\xi_H = 0$ and $\alpha_V = 0$ (corresponding to a coherent state in the H-mode and a squeezed vacuum state in the V-mode), the behavior of the two polarization measures is very different as illustrated in Fig. 5.3 (middle column). Finally, we plot the two-mode displaced squeezed state (with $\xi_H = 0.2$ and $\xi_V = 0.6$) in Fig. 5.3 (right column). The plot for the semi-classical measure once again illustrates its weakness as a measure of polarization: The polarization goes all the way to zero in a point where the state is neither thermal nor vacuum as required for a Gaussian state to be unpolarized, and it is not because the polarization is hidden in the higher moments which can be seen from the lower plot of $\mathbb{P}_1^{\text{res}}$.

5.2.2 Experimental investigation of $\mathbb{P}_1^{\text{res}}$

We use the experimental method discussed in Sec. 5.1.3 with the setup shown in 5.1. Since the generated states have Gaussian wavefunctions, it suffices to estimate the covariance matrix of the state for full characterization [1]. From this we calculate a sufficient number of excitation manifolds of the two-mode density matrix and take the expectation values of the Stokes operators (per manifold) from which the degree of polarization is estimated.

We start our experimental analysis with a single-mode squeezed or single-mode coherent states, with the other mode being in a vacuum state. These states are produced by blocking OPA2 while operating either the EOM (for producing the coherent state) or the OPA1 (for producing the squeezed states). The excitation of the coherent state is controlled by the modulation depth of the EOM whereas the squeezing degree (or the average number of photons associated with the squeezing process) of the squeezed state is controlled by the

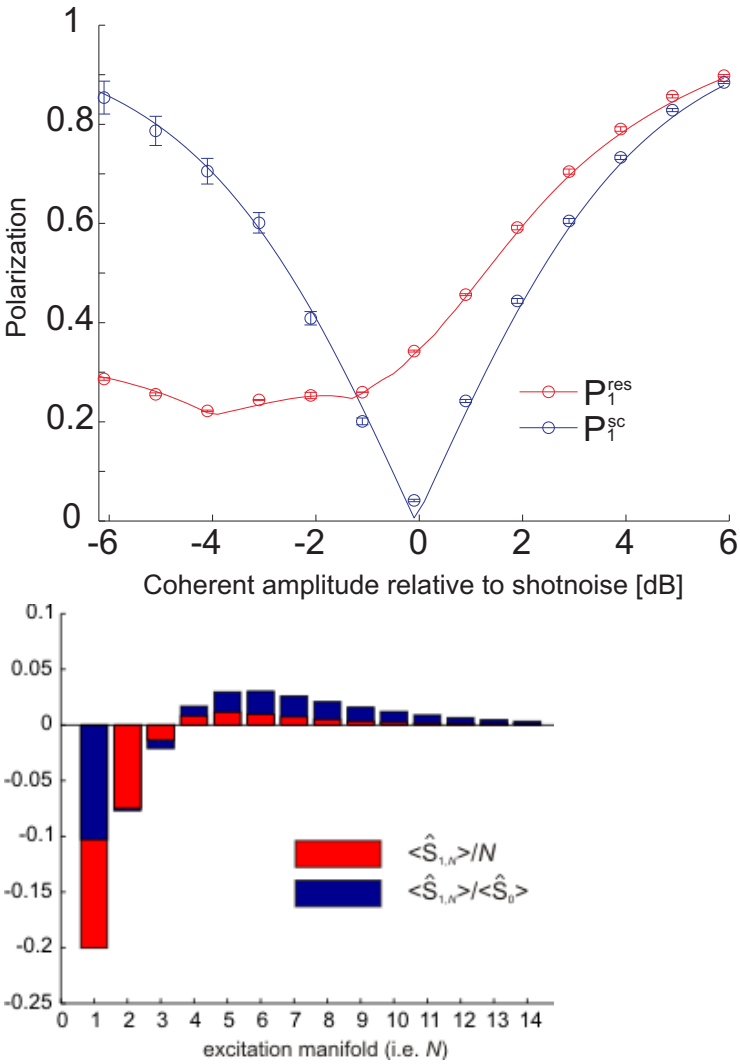

Figure 5.4: Upper figure: Degree of polarization for experimental data of a squeezed state in mode H and a displaced coherent state in mode V. Circles indicate experimental data while lines are simulations. We vary the displacement from -6 dB ($\alpha = 0.25$, 0.0625 photons) to 6 dB ($\alpha = 4$, 16 photons). The squeezed state has a squeezing of 3.2 dB and an antisqueezing of 7.4 dB, corresponding to 1.0 photons. Error bars correspond to 1% uncertainty in the shot noise. Simulations starting from the initial squeezed state are shown with the solid lines. Lower: the polarization contributions of the different manifolds for the 0 dB (1 photon) state. Only $\langle \hat{S}_1 \rangle$ contributes to the polarization of the states produced here (i.e., $\langle \hat{S}_2 \rangle = \langle \hat{S}_3 \rangle = 0$) and therefore one has $\mathbb{P}_1^{\text{sc}} = |\sum \text{blue bars}|$ and $\mathbb{P}_1^{\text{res}} = \sum |\text{red bars}|$.

pump power. Our results for $\mathbb{P}_1^{\text{res}}$ and $\mathbb{P}_1^{\text{sc}}$ are plotted in Fig. 5.2, where the error bars indicate the 1% uncertainty in determining the shot-noise limit. The experimental values for the squeezed state deviates slightly from the theoretical prediction (Eq. (5.5) with $\alpha = 0$) which is a consequence of the small impurity of the generated state. As also predicted by theory, we see that both states become more polarized as the photon numbers from the coherent state or from the squeezed state increases.

Next, we investigate another particularly interesting state in which a coherent state is excited in the H-mode while the V-mode is a squeezed vacuum state. The squeezed state is squeezed by 3.2 dB below the shot noise limit (7.4 dB antisqueezing) and the coherent excitation of the H mode is varied.

We present the experimental results for this state in Fig. 5.4. For a coherent amplitude of -6 dB ($\alpha = 0.25$), $\mathbb{P}_1^{\text{sc}}$ yields a large degree of polarization of 0.88 although this state is very close to the vacuum state. When increasing the coherent modulation, $\mathbb{P}_1^{\text{sc}}$ decreases to zero which occurs when the number of photons in each polarization mode is the same (in this case = 1.0). This result is not desirable for a polarization measure as the state is not invariant to polarization rotations.

In contrast, the new measure displays a more natural behavior: The degree of polarization is reasonably small for low excitations. There is clear signs of interference between the photon distributions of the squeezed state and the coherent state. When the coherent state dominates a more monotonic behavior is observed. These different behaviors can be understood by looking at the contributions of the different manifolds in definition (5.2). $\hat{S}_1$ is the only operator contributing to the polarization and we plot the expectation value of this per manifold in the lower part of Fig. 5.4. Here, we see that it points in opposite directions for the different manifolds which then sum up to zero for the $\mathbb{P}_1^{\text{sc}}$, and thus the polarization becomes hidden. However, for the $\mathbb{P}_1^{\text{res}}$-measure, the polarization is not hidden since in this case the absolute value of the $\langle \hat{S}_1 \rangle$-values from the different manifolds are added.

5.3 Defining and illustrating $\mathbb{P}_2$

The first Stokes based measure to capture (part of) the second moment of the polarization was [92]

$$\mathbb{P}_2' = \frac{\sqrt{\Delta \hat{\mathbf{S}}}}{\langle \hat{S}_0^2 \rangle}, \tag{5.7}$$

where $\Delta \hat{\mathbf{S}} = \sqrt{\langle \hat{S}_1^2 \rangle + \langle \hat{S}_2^2 \rangle + \langle \hat{S}_3^2 \rangle}$. However it does not take fully into account the distribution of noise in phase space assigning different polarizations to the same state rotated by polarization rotations.

The first project we took part in regarding polarization was the definition of a new $\mathbb{P}_2$ measure [75]. The new measure is defined as

$$\mathbb{P}_2(\rho) = \sqrt{1 - \inf_n \frac{(\Delta S_n)^2}{\frac{1}{3}\hat{\mathbf{S}}^2}}, \tag{5.8}$$

where (ΔS_n) is the standard deviation of $\hat{\mathbf{S}} \cdot \mathbf{n}$ and $\mathbf{n}$ is a unit vector. The optimization can be performed by finding the minimal eigenvalue of the positive

covariance matrix between $\hat{S}_1, \hat{S}_2$ and $\hat{S}_3$ and the corresponding eigenvector. This definition solves the problem of $\mathbb{P}_2^{'}$ by assigning a unique value to the polarization.

5.3.1 First experiment for $\mathbb{P}_2$

Our part in the project was to experimentally illustrate the measure. To do this we made an experiment involving only a single OPA and a single homodyne detector of Fig 5.1. By coupling the squeezed seed from the OPA to the vacuum mode in the polarization interferometer we generated a polarization state. After decoupling the two polarization modes spatially we measured them sequentially with full tomography. We verified that the measured vacuum state was a vacuum state (within the statistical error-bars) so we could be certain that there were no correlations between the two beams. After this we reconstructed the single-mode states with a maximum-likelihood algorithm. The reconstructed squeezed state had -3.8 dB of squeezing and 8.6 dB antisqueezing.

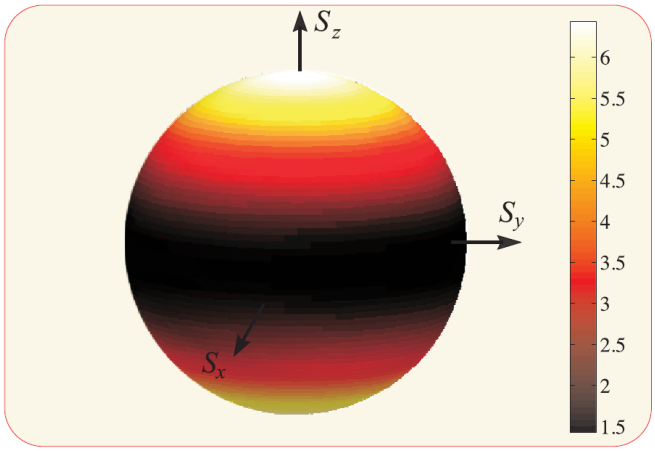

Figure 5.5: The angular distribution of the variance $(\Delta S_n)^2$, linear colorscale.

The measured polarization is $\mathbb{P}_1^{sc} = 0.998 \pm 0.001$ and $\mathbb{P}_2 = 0.79 \pm 0.01$ while $\mathbb{P}_2^{'} = 0.43 \pm 0.01$. We illustrate the difference between $\mathbb{P}_2^{'}$ and $\mathbb{P}_2$ by plotting (ΔS_n) as function of $\mathbf{n}$ in Fig. 5.5.

5.4 Defining and illustrating $\mathbb{P}_2^{res}$

Although taking into account the second moment gives a richer picture of the polarization the measure $\mathbb{P}_2$ suffers from some problems very similar to the original $\mathbb{P}_1^{sc}$. If the polarization of the variance points in different directions in the different manifolds the measure will underestimate the polarization and if taking e.g two pure squeezed states the measure will give 1 independent of the size of the state and the unpolarized vacuum contribution.

To overcome these problems we propose to resolve the manifolds as done for

$\mathbb{P}_1^{\text{res}}$, but for the second order in the Stokes operators. We define

$$\mathbb{P}_2^{\text{res}}(\rho) = \sum_{N=1} p_N \sqrt{1 - \inf_n \frac{3(\Delta S_{n,N})^2}{\mathbf{S}_N^2}}, \tag{5.9}$$

where p_N is the probability of being in the N_{th} manifold, $\mathbf{S}_N^2 = \hat{S}_{0,N}(\hat{S}_{0,N}+2)$ is a normalization factor for the manifold and $\inf_n(\Delta S_{n,N})^2$ is the smallest variance of the given manifold. For each manifold the polarization is calculated as it was for $\mathbb{P}_2$, however now each polarization manifold is weighted with the probability of being in the given state and the absolute value is taken before the summation.

5.4.1 Comparison of the $\mathbb{P}$'s

To compare the measures we have made a series of simulations and experiments. The experiments are carried out as in Sec. 5.2.2, now using both OPA's from Fig. 5.1. To illustrate the difference between $\mathbb{P}_2^{\text{res}}$ and $\mathbb{P}_2$ we start by looking at the degree of polarization when having squeezed states with equal energy in both modes, see Fig. 5.6. The simulation shows that the polarization is hidden for $\mathbb{P}_1^{\text{res}}$ and $\mathbb{P}_1$, while $\mathbb{P}_2$ estimates all the states to be completely polarized.

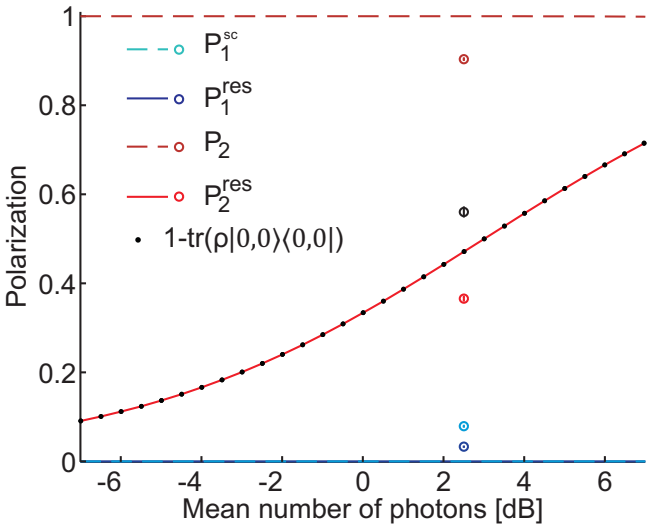

Figure 5.6: Simulation (lines) and experimental data (circles) with squeezing in both modes. For the pure states in the simulation the new $\mathrm{P}_2^{\text{res}}$ exactly follows the vacuum contribution, while none of the other measures can quantify this type of polarization. The data marked with circles are data points for squeezed states with 3.6 dB (7.0 dB) (in H-mode) and 2.4 dB (7.0 dB) (in V-mode) and 0.86 and 0.90 photons on average.

In contrast our proposed measure $\mathbb{P}_2^{\text{res}}$ neatly follows one minus the vacuum. The experimental data shown in Fig. 5.6 has $\mathbb{P}_1 = 0.026$ $\mathbb{P}_1^{\text{res}} = 0.039$ $\mathbb{P}_2^{\text{res}} = 0.39$ $\mathbb{P}_2 = 0.90$ while one minus the vacuum contribution $1 - \rho_{0,0} = 0.44$. In words this mean that the first order measures are unable to detect the polarization in this state. $\mathbb{P}_2$ gives a polarization close to unity even thought there is a

significant vacuum contribution while $\mathbb{P}_2^{\text{res}}$ gives a very reasonable value of the polarization.

Next we displace one of the squeezed modes, first along the squeezing direction shown in Fig. 5.7 a). We see that all the measures gives smooth curves and all but $\mathbb{P}_2$ are below the $1-\rho_{0,0}$ limit. By instead displacing one of the squeezed states along antisqueezing direction, the polarization shown in Fig. 5.7 b) is observed. This is a radically different picture for the second order measures while the first order measures hardly see the difference. The complex sign of the displacement makes the variance of polarization point in different direction in the different manifolds causing destructive interference in similar fashion as was observed in Fig. 5.4 for the first order measures.

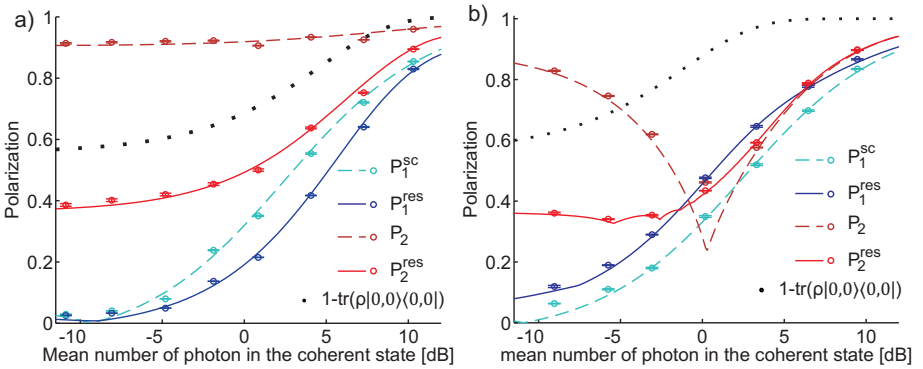

Figure 5.7: Simulation (lines) and experimental data (circles) with fixed 3.6 dB (7.0 dB) and 2.4 dB (7.0 dB) amplitude squeezing (phase antisqueezing) in the two modes. a) Displacement along squeezed direction. b) Displacement along the antisqueezing direction.

The single mode states and the two-mode thermal state are important tests for the new measures. We plot these with energy constraints in Fig. 5.8. We see as expected that the polarization of $\mathbb{P}_1^{\text{res}}$ exactly follow the vacuum contribution of the single-mode states. Further we see that $\mathbb{P}_2^{\text{res}}$ is smaller than the vacuum contribution and smaller than $\mathbb{P}_2$. Only in the case shown in Fig. 5.7 b) where the polarization contributions are pointing in different directions does $\mathbb{P}_2^{\text{res}}$ give a higher polarization than $\mathbb{P}_2$. In general we see that the resolved measures are neither convex nor concave functions of the displacements, when the photon numbers in the two modes are similar and originate from different types of distributions. However when the one mode is dominating the monotonic (classical like) behavior returns.

5.4.2 Hidden polarization

To analyze the mechanism that hides the polarization from the first order measures we plot the first 5 manifolds of the two-mode density matrix of the experimentally generated state in Fig 5.9 a). The block diagonal carries the polarization information. The impurity of the states gives a thermal contribution visible in the $\langle \hat{S}_0 \rangle = 1$ and the $\langle \hat{S}_0 \rangle = 3$ manifolds, which would be zero otherwise. However we see that there are no diagonal elements next to each other in the block diagonal. Furthermore the diagonal elements are ordered so that

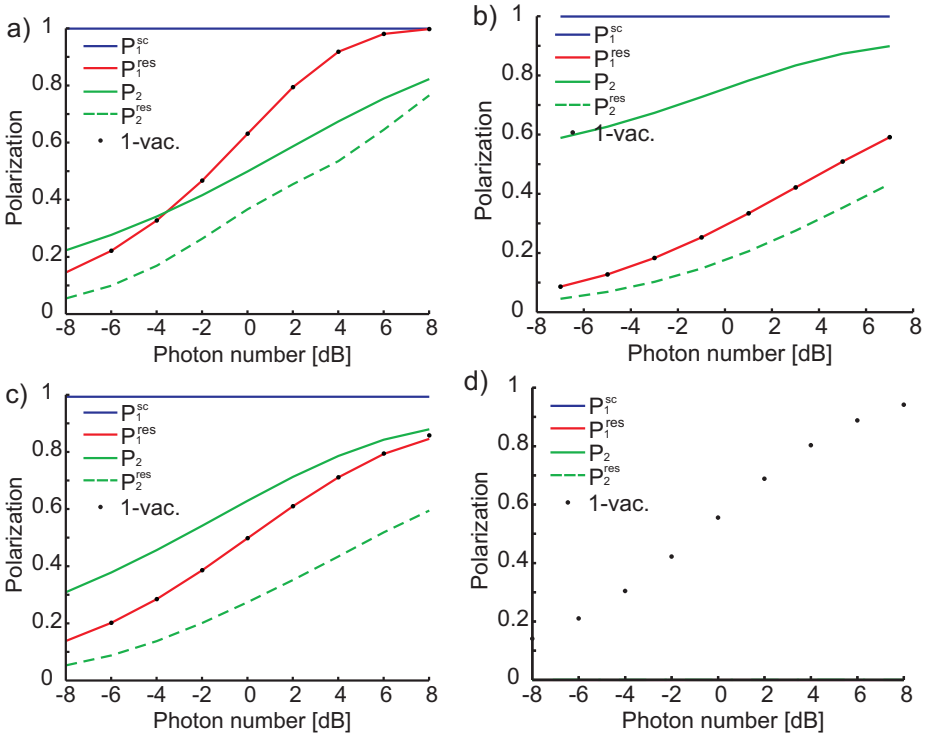

Figure 5.8: a) Coherent state and vacuum. b) Squeezed state and vacuum. c) Thermal state and vacuum. d) Two-mode thermal state (all the measures show the state to be unpolarized as expected). 1-vac is the same as $1 - \rho_{0,0}$

even though they are not uniform within a manifold, they still cancel (e.g. $\rho_{2,0} - \rho_{1,1} = -\rho_{1,1} - \rho_{0,2}$). These two criteria are sufficient to make the first moment of the Stokes operators vanish. However, if we make a polarization rotation (on one of the manifolds) there can be neighboring coherences, but the polarization is still the same.

Inspired by these symmetries we simulate a state that does not have 1st nor 2nd moment of polarization but has a significant 4th moment, see Fig 5.9 b). This state is generated by mixing $\frac{2}{3}$'s of a squeezed state like our experimentally generated state and $\frac{1}{3}$ of the same state rotated $\frac{\pi}{4}$ around $\hat{S}_2$.

Alternatively we can generate hidden polarization by mixing coherent states. To generate a first order hidden polarization state one can e.g. take coherent states with $\alpha_H = 1, \alpha_V = i$ mixed with $\alpha_H = 1, \alpha_V = -i$. A first and second but not 4th order hidden polarization state can be generated by rotating it $\frac{\pi}{4}$ around $\hat{S}_1$, $\hat{S}_2$ and $\hat{S}_3$ and mixing these 3 states with equal parts of each.

5.4.3 SU_2 Wigner functions

With these measures we can quantify the polarization up to second order in the Stokes operators. We will not try to quantify the remaining polarization, however we can illustrate it by plotting the SU_2 Wigner function [93]. Any lack of symmetry will give rise to different statistics when performing polarization

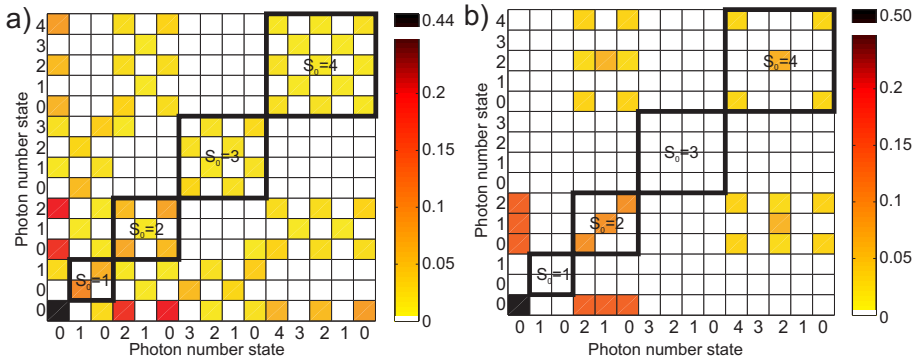

Figure 5.9: a) Reconstructed two-mode density matrix of an experimentally realized first order hidden polarization state. The matrix is written in block diagonal form, in the H-V basis, and we have taken the absolute value of the elements. The color-bar gives the magnitude of the matrix elements. b) Simulation of two-mode density matrix of a second order hidden polarization state, with a non-zero 4th order moment.

rotations.

The SU_2 Wigner functions are quasi probability distribution over operators satisfying an SU(2) algebra. The operators $\hat{S}_i, i \in \{1,2,3\}$ fulfill this algebra with their commutation relation $\left[\hat{S}_i, \hat{S}_j\right] = 2i\epsilon_{ijk}\hat{S}_k$ and hence this formalism can be used. Unlike the normal Wigner function where there is a one to one correspondence between the Wigner function and the full density matrix, the SU_2 Wigner functions have a one to one correspondence with the block diagonal of the two-mode density matrix. The marginal distributions reproduce the distributions of the Stokes operators. In this sense they illustrate exactly what we would expect from the Wigner function of the polarization state.

To obtain explicit formulas we use the Schwinger representation identifying $\hat{J}_i = \hat{S}_i/2$. The eigenstates of $\hat{J}^2$ and $\hat{J}_3$, $|j,m\rangle$, then correspond to a relabeling of the block diagonal of the density matrix (Fock basis) as $j = (n_L + n_R)/2$ and $m = (n_L - n_R)/2$, where n_L and n_R are the left-hand/right-hand circularly polarized photon number. We make a multipole expansion of the density matrix of a subspace j as

$$\hat{\rho}^{(j)} = \sum_{k=0}^{2j} \sum_{q=-k}^{k} \rho_{kq}^{(j)} \hat{T}_{kq}^{(j)} \tag{5.10}$$

where $\hat{T}_{kq}^{(j)}$ are the spherical tensors

$$\hat{T}_{kq}^{(j)} = \sum_{m=-j}^{j} \sum_{m'=-j}^{j} (-1)^{j-m} \sqrt{2k+1} \begin{pmatrix} j & k & j \\ -m & q & m' \end{pmatrix} |j\,m\rangle\langle j\,m'| \tag{5.11}$$

and $\begin{pmatrix} j & k & j \\ -m & q & m' \end{pmatrix}$ is the Wigner-3j symbol and further

$$\rho_{kq}^{(j)} = Tr[\hat{\rho}^{(j)} \cdot \hat{T}_{kq}^{(j)\,\dagger}]. \tag{5.12}$$

The SU_2 Wigner function for an excitation manifold j is then

$$W^{(j)}(\theta,\varphi) = \sum_{k=0}^{2j} \sum_{q=-k}^{+k} \rho_{kq}^{(j)} Y_{kq}(\theta,\varphi), \tag{5.13}$$

where the $Y_{kq}(\theta,\varphi)$ are the Laplace spherical harmonics. The radial distribution is the discrete spheres given by $r(S_0) = \sqrt{\frac{S_0}{2}(\frac{S_0}{2}+1)}$.

In our states there are many excited photon numbers so the SU_2 Wigner functions have probability amplitude in many excitation manifolds in contrast e.g. to the case in reference [94] where only one manifold is excited. To see all the non-trivial parts of the Wigner functions we encode the probability amplitude in the color scale and the absolute of the probability amplitude linearly in the transparency. We start with the two-mode vacuum squeezed state in Fig. 5.10 a). The symmetries of the state is what makes the polarization hidden for the first order measures, however as both the figure and the 2nd order measures show, the state is not invariant under rotations. In Fig. 5.10 b) we illustrate the above mentioned mixture of squeezed states which does not show polarization with neither the first nor the 2nd order polarization measure. It is however clear from the figure that this state is not polarization rotation invariant and as argued from the density matrices a fourth order polarization measure should show the polarization of this state. In Fig. 5.11 a) we displace one of the two squeezed states in the squeezing direction as was done in Fig. 5.7 a) and see that the shape resembles that of a disk by looking in the three planes Fig. 5.11 b) c) d). If we instead of displacing along the squeezing direction displace along the antisqueezing Fig. 5.12 a) as was done in Fig. 5.7 b) we see that we get something which resembles a cigar shown in 5.12 b) c) d).

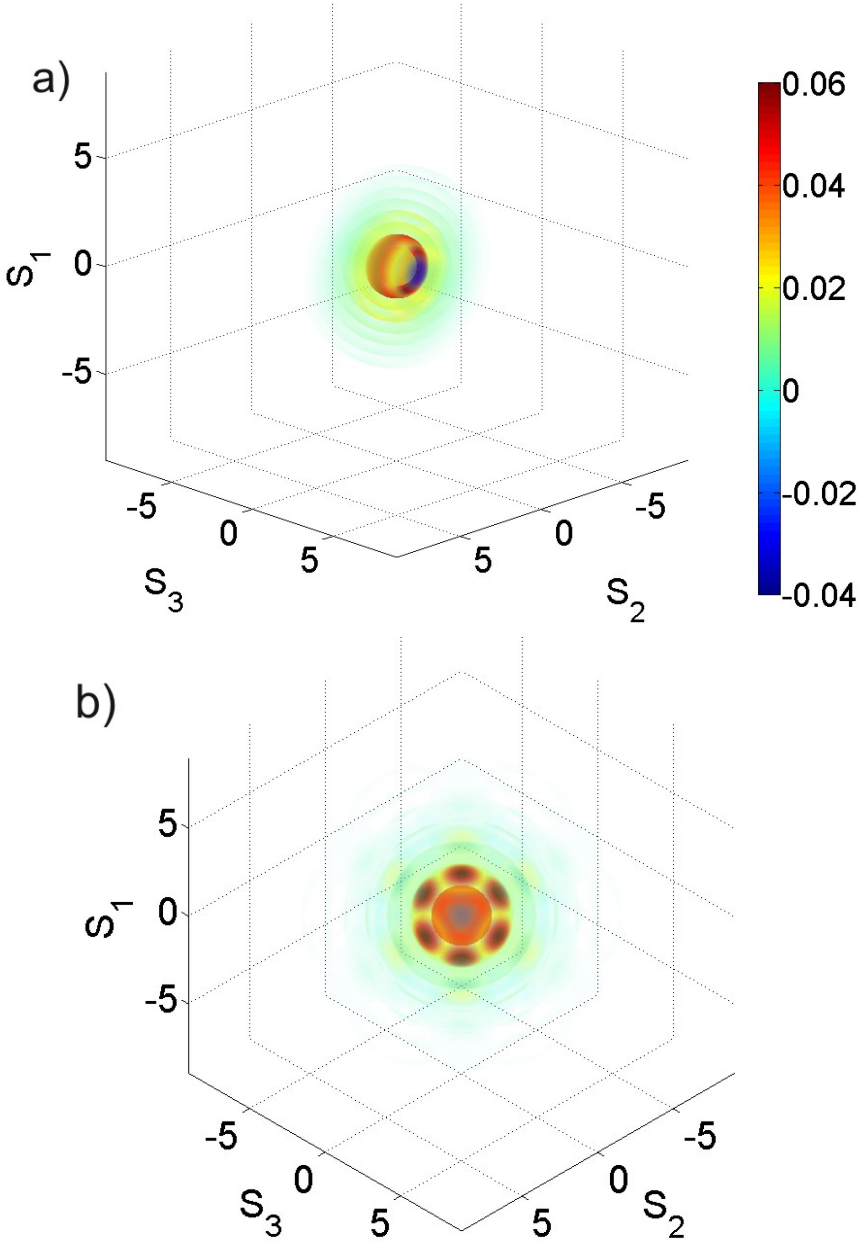

Figure 5.10: Reconstructed SU2 Wigner functions. a) Experimental data for two-mode vacuum squeezed states (same state as Fig. 5.9 a)). b) Simulation of mixture of vacuum squeezed states the polarization is hidden from both first and second order polarization measures (same state as Fig. 5.9 b)). Same colorbar for a) and b).

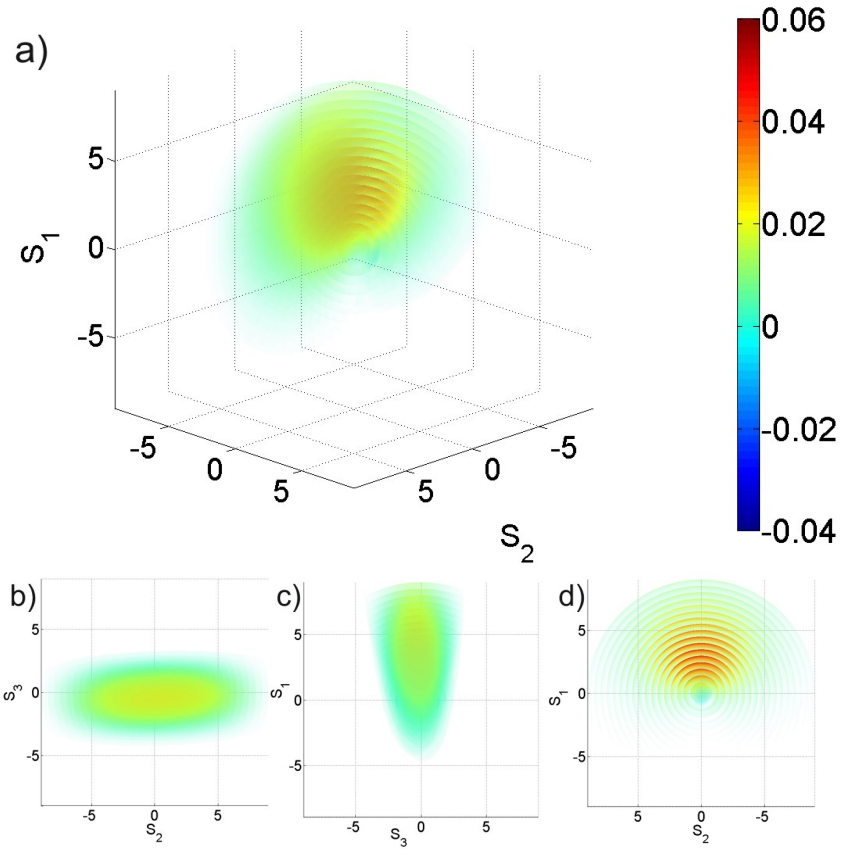

Figure 5.11: a) Experimental data: A small displacement is added to one of the squeezed states along the squeezing direction. b) c) d) Viewing a) from S_1-, S_2- and S_3- direction respectively. Same colorbar for all figures.

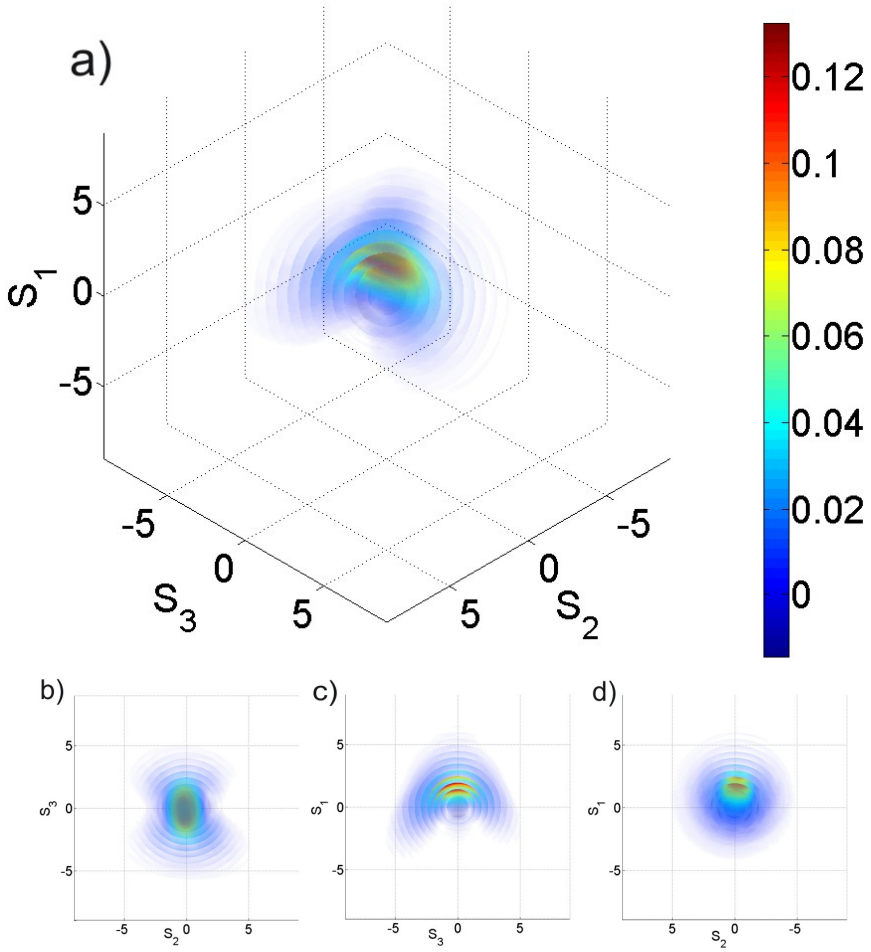

Figure 5.12: a) Experimental data: Small displacement is added along the anti-squeezing direction. b) c) d) Viewing a) from S_1-, S_2- and S_3- direction respectively. Same colorbar for all figures.

Chapter 6

Concluding remarks

6.1 Summary

The thesis is built up around a versatile optical experimental setup based on a laser, two optical parametric amplifiers, a few sets of modulators and two sets of homodyne detectors, which together with passive linear optics generate, process and characterize various types of Gaussian quantum states. Using this setup we have experimentally and theoretically investigated Gaussian quantum discord, continuous variable quantum key distribution and quantum polarization.

The Gaussian discord broadens the definition of non-classical correlations from entanglement, to all types of correlations which cannot be extracted by local measurements due to the limitations dictated by the Heisenberg's uncertainty principle. We experimentally characterize the evolution of the discord of EPR states and mixtures of coherent states in an attenuating channel. We demonstrate that the discord can grow by local dissipation in the mixture of coherent states. Further we investigate the robustness of the discord of a broader range of states and suggest a toolbox of states which can be used to test if a protocol is discord based, before performing a rigid proof.

Gaussian quantum key distribution can be implemented with current commercially available equipment. However the performance in terms of achievable distance is highly limited. We first experimentally demonstrate that the boundaries of coherent states can be surpassed using modulated entangled states. A simplified experiment is also presented where the modulation of a single-mode squeezed state gives a very reconciliation efficiency robust protocol. All of this is done to achieve higher key rates at the current limits of the coherent state protocols and to extend the boundaries for tolerable channel noise, loss and reconciliation efficiency. As any degree of squeezing improves the performance the extra effort of implementing squeezing in commercial devices is overshadowed by the extended range and increased security margin achieved.

Still using the same experimental setup, but now in the context of polarization we have experimentally bridged the gab between the states with very low photon numbers and the states where one of Stokes parameters is highly excited. To describe the polarization of these state we introduce several new polarization measures which take into account the covariance of the polarization and resolve the polarization manifolds. We experimentally demonstrate states for which the

polarization is hidden in the unresolved measures and as well a state which is unpolarized for both first order polarization measures. Finally we illustrate the polarization with SU_2 Wigner functions to give a richer picture, not only of the degree of polarization but also its distribution among the manifolds.

6.2 Outlook

Quantum information science is still a young research field. The discrete variable formalism and experiments have dominated the early history of the field, however in recent years the continuous variables have gained a footing. In this thesis we have been focused on the continuous variable Gaussian states. The power of the Gaussian state formalism has allowed theoretical result which we have used, such as the general security framework for Gaussian quantum key distribution and the optimization of measurements which lead to the closed formulas for the Gaussian discord.

The Gaussian formalism has however also demonstrated several no-go theorems for all Gaussian (that is Gaussian states, Gaussian unitaries and Gaussian measurements) protocols including error correction, entanglement distillation and quantum computation. Advancing in these subjects would hence require non-Gaussian operations e.g. in the form an optical hybrid schemes based on Gaussian states but non-Gaussian measurements, a breakthrough within new stronger 3rd order non-linearities or coupling to other quantum resources such as solid oscillators, atomic clouds, BECs or other novel media.

These tasks are however not the only ones of interest in quantum optics. Especially the squeezed states have a bright future as a resource in energy constrained metrology and information, it being gravitational wave detection in facilities such as LIGO [95], measurements on microtoroids [96] or quantum key distribution as we have seen here and maybe the entangled states could prove beneficial as well if smartly applied [54].

Bibliography

[1] Christian Weedbrook, Stefano Pirandola, Raúl García-Patrón, Nicolas Cerf, Timothy Ralph, Jeffrey Shapiro, and Seth Lloyd. Gaussian quantum information. *Reviews of Modern Physics*, 84(2):621–669, May 2012. 4, 7, 8, 13, 19, 45, 58, 66

[2] Ulrik L. Andersen, Gerd Leuchs, and Christine Silberhorn. Continuous Variable Quantum Information Processing. *Laser & Photonics Reviews*, 4:337–354, August 2010. 4, 34

[3] Samuel L Braunstein and Peter van Loock. *Reviews of Modern Physics*, October. 4

[4] M. O. Scully and M. S. Zubairy. *Quantum optics*. Cambridge University Press, 1997. 7

[5] U. Leonhardt. *Measuring the Quantum State of Light*. Cambirdge University Press, 1997. 7, 15

[6] Gerardo Adesso and Fabrizio Illuminati. Entanglement in continuous-variable systems: recent advances and current perspectives. *Journal of Physics A: Mathematical and Theoretical*, 40(28):7821–7880, July 2007. 7, 8

[7] J.J. Sakurai. *Modern Quantum Mechanics*. Addison-Wesley Publishing Company, 1994. 7

[8] A. Einstein, B. Podolsky, and N. Rosen. Can Quantum-Mechanical Description of Physical Reality Be Considered Complete? *Physical Review*, 47(10):777–780, May 1935. 11

[9] A. Ferraro, S. Olivares, and M. G. A. Paris. *Gaussian States in Quantum Information*. Bibliopolis, Napoli, 2005. 13

[10] M. A Nielsen and I. L. Chuang. *Quantum Computation and Quantum information*. Cambirdge University Press, 2000. 13, 17, 19, 33

[11] Alessio Serafini, Fabrizio Illuminati, and Silvio De Siena. Symplectic invariants, entropic measures and correlations of Gaussian states. *Journal of Physics B: Atomic, Molecular and Optical Physics*, 37(2):L21–L28, January 2004. 19

[12] BEA Saleh and MC Teich. *Fundamentals of photonics*. 1991. 22

[13] R. W. P. Drever, J. L. Hall, F. V. Kowalski, J. Hough, G. M. Ford, A. J. Munley, and H. Ward. Laser phase and frequency stabilization using an optical resonator. *Applied Physics B Photophysics and Laser Chemistry*, 31(2):97–105, June 1983. 24

[14] G. D. Boyd and Kleinman D. A. Parametric Interaction of Focused Gaussian Light Beams. *Journal of Applied Physics*, 39(8):3597, 1968. 25

[15] Yuishi Takeno, Mitsuyoshi Yukawa, Hidehiro Yonezawa, and Akira Furusawa. Squeezed light at 1550 nm with a quantum noise reduction of 12.3 dB. *Optics Express*, 15:4321–4327. 27

[16] Moritz Mehmet, Stefan Ast, Tobias Eberle, Sebastian Steinlechner, Henning Vahlbruch, and Roman Schnabel. Squeezed light at 1550 nm with a quantum noise reduction of 12.3 dB. *Optics Express*, 19:25763–25772. 27

[17] E. Knill and R. Laflamme. Power of One Bit of Quantum Information. *Physical Review Letters*, 81(25):5672–5675, December 1998. 33

[18] C. A. Ryan, J. Emerson, D. Poulin, C. Negrevergne, and R. Laflamme. Characterization of Complex Quantum Dynamics with a Scalable NMR Information Processor. *Physical Review Letters*, 95(25), December 2005. 33

[19] B. P. Lanyon, M. Barbieri, M. P. Almeida, and A. G. White. Experimental Quantum Computing without Entanglement. *Physical Review Letters*, 101(20), November 2008. 33

[20] Animesh Datta, Anil Shaji, and Carlton M. Caves. Quantum Discord and the Power of One Qubit. *Physical Review Letters*, 100(5), February 2008. 33

[21] C Bennett and C Brassard. Quantum Cryptography: Public key distribution and coin tossing. In *Proceedings of the International Conference of Computer Systems and Signal Processing*, page 175. IEEE, New York, 1984. 33, 45

[22] Frédéric Grosshans, Gilles Van Assche, Jérôme Wenger, Rosa Brouri, Nicolas J Cerf, and Philippe Grangier. Quantum key distribution using gaussian-modulated coherent states. *Nature*, 421(6920):238–41, January 2003. 33, 34, 45, 47, 58

[23] Harold Ollivier and Wojciech H. Zurek. Quantum Discord: A Measure of the Quantumness of Correlations. *Physical Review Letters*, 88(1):15–18, December 2001. 33

[24] L Henderson and V Vedral. Classical, quantum and total correlations. *Journal of Physics A: Mathematical and General*, 34(35):6899–6905, September 2001. 33

[25] Francesco Ciccarello and Vittorio Giovannetti. Local-channel-induced rise of quantum correlations in continuous-variable systems. *Physical Review A*, 85(2), February 2012. 33, 34

[26] Francesco Ciccarello and Vittorio Giovannetti. Creating quantum correlations through local nonunitary memoryless channels. *Physical Review A*, 85(1), January 2012. 33, 34

[27] S. Campbell, T. Apollaro, C. Di Franco, L. Banchi, A. Cuccoli, R. Vaia, F. Plastina, and M. Paternostro. Propagation of nonclassical correlations across a quantum spin chain. *Physical Review A*, 84(5), November 2011. 33, 34

[28] Alexander Streltsov, Hermann Kampermann, and Dagmar Bruß. Behavior of Quantum Correlations under Local Noise. *Physical Review Letters*, 107(17), October 2011. 33, 34

[29] Jin-Shi Xu, Xiao-Ye Xu, Chuan-Feng Li, Cheng-Jie Zhang, Xu-Bo Zou, and Guang-Can Guo. Experimental investigation of classical and quantum correlations under decoherence. *Nature communications*, 1:7, January 2010. 33

[30] Bo Wang, Zhen-Yu Xu, Ze-Qian Chen, and Mang Feng. Non-Markovian effect on the quantum discord. *Physical Review A*, 81(1), January 2010. 33

[31] F. F. Fanchini, T. Werlang, C. A. Brasil, L. G. E. Arruda, and A. O. Caldeira. Non-Markovian dynamics of quantum discord. *Physical Review A*, 81(5), May 2010. 33

[32] R. Dillenschneider and E. Lutz. Energetics of quantum correlations. *EPL (Europhysics Letters)*, 88(5):50003, December 2009. 33

[33] M. Sarandy. Classical correlation and quantum discord in critical systems. *Physical Review A*, 80(2), August 2009. 33

[34] Vaibhav Madhok and Animesh Datta. Interpreting quantum discord through quantum state merging. *Physical Review A*, 83(3), March 2011. 33

[35] D. Cavalcanti, L. Aolita, S. Boixo, K. Modi, M. Piani, and A. Winter. Operational interpretations of quantum discord. *Physical Review A*, 83(3), March 2011. 33

[36] Marco Piani, Pawe Horodecki, and Ryszard Horodecki. No-Local-Broadcasting Theorem for Multipartite Quantum Correlations. *Physical Review Letters*, 100(9), March 2008. 33

[37] Gerardo Adesso and Animesh Datta. Quantum versus Classical Correlations in Gaussian States. *Physical Review Letters*, 105(3), July 2010. 33, 34

[38] Paolo Giorda and Matteo Paris. Gaussian Quantum Discord. *Physical Review Letters*, 105(2), July 2010. 33, 34

[39] Richard Tatham, Ladislav Mišta, Gerardo Adesso, and Natalia Korolkova. Nonclassical correlations in continuous-variable non-Gaussian Werner states. *Physical Review A*, 85(2), February 2012. 33

[40] Ling-An Wu, H. Kimble, J. Hall, and Huifa Wu. Generation of Squeezed States by Parametric Down Conversion. *Physical Review Letters*, 57(20):2520–2523, November 1986. 34

[41] Ulrik Andersen, Vincent Josse, and Gerd Leuchs. Unconditional Quantum Cloning of Coherent States with Linear Optics. *Physical Review Letters*, 94(24), June 2005. 34

[42] A. Furusawa. Unconditional Quantum Teleportation. *Science*, 282(5389):706–709, October 1998. 34

[43] Rémi Blandino, Marco G. Genoni, Jean Etesse, Marco Barbieri, Matteo G. A. Paris, Philippe Grangier, and Rosa Tualle-Brouri. Homodyne estimation of Gaussian quantum discord. March 2012. 34

[44] Mile Gu, Helen M. Chrzanowski, Syed M. Assad, Thomas Symul, Kavan Modi, Timothy C. Ralph, Vlatko Vedral, and Ping Koy Lam. Operational Significance of Discord: Theory and Experiment. page 10, February 2012. 34

[45] W. P. Bowen, R. Schnabel, and P. K. Lam. Experimental Investigation of Criteria for Continuous Variable Entanglement. *Physical Review Letters*, 90(4), January 2003. 35

[46] Ryszard Horodecki, Micha Horodecki, and Karol Horodecki. Quantum entanglement. *Reviews of Modern Physics*, 81(2):865–942, June 2009. 38

[47] Valerio Scarani, Helle Bechmann-Pasquinucci, Nicolas Cerf, Miloslav Dušek, Norbert Lütkenhaus, and Momtchil Peev. The security of practical quantum key distribution. *Reviews of Modern Physics*, 81(3):1301–1350, September 2009. 45

[48] Frédéric Grosshans and Philippe Grangier. Continuous Variable Quantum Cryptography Using Coherent States. *Physical Review Letters*, 88(5), January 2002. 45, 47

[49] Jérôme Lodewyck, Matthieu Bloch, Raúl García-Patrón, Simon Fossier, Evgueni Karpov, Eleni Diamanti, Thierry Debuisschert, Nicolas Cerf, Rosa Tualle-Brouri, Steven McLaughlin, and Philippe Grangier. Quantum key distribution over 25km with an all-fiber continuous-variable system. *Physical Review A*, 76(4):1–10, October 2007. 45, 48

[50] Ch. Silberhorn, T. Ralph, N. Lütkenhaus, and G. Leuchs. Continuous Variable Quantum Cryptography: Beating the 3 dB Loss Limit. *Physical Review Letters*, 89(16), September 2002. 45

[51] Stefano Pirandola, Samuel Braunstein, and Seth Lloyd. Characterization of Collective Gaussian Attacks and Security of Coherent-State Quantum Cryptography. *Physical Review Letters*, 101(20), November 2008. 45

[52] S. Lorenz, N. Korolkova, and G. Leuchs. Continuous-variable quantum key distribution using polarization encoding and post selection. *Applied Physics B*, 79(3):273–277, June 2004. 45

[53] Christian Weedbrook, Andrew Lance, Warwick Bowen, Thomas Symul, Timothy Ralph, and Ping Lam. Quantum Cryptography Without Switching. *Physical Review Letters*, 93(17), October 2004. 45

[54] Stefano Pirandola, Stefano Mancini, Seth Lloyd, and Samuel L. Braunstein. Continuous-variable quantum cryptography using two-way quantum communication. *Nature Physics*, 4(9):726–730, July 2008. 45, 59, 80

[55] Raúl García-Patrón and Nicolas Cerf. Continuous-Variable Quantum Key Distribution Protocols Over Noisy Channels. *Physical Review Letters*, 102(13), March 2009. 45, 46, 48, 58

[56] Christian Weedbrook, Stefano Pirandola, Seth Lloyd, and Timothy Ralph. Quantum Cryptography Approaching the Classical Limit. *Physical Review Letters*, 105(11), September 2010. 45

[57] T. Ralph. Continuous variable quantum cryptography. *Physical Review A*, 61(1), December 1999. 45

[58] Mark Hillery. Quantum cryptography with squeezed states. *Physical Review A*, 61(2), January 2000. 45

[59] N. Cerf, M. Lévy, and G. Assche. Quantum distribution of Gaussian keys using squeezed states. *Physical Review A*, 63(5), April 2001. 45

[60] Daniel Gottesman and John Preskill. Secure quantum key distribution using squeezed states. *Physical Review A*, 63(2), January 2001. 45

[61] Xiaolong Su, Wenzhe Wang, Yu Wang, Xiaojun Jia, Changde Xie, and Kunchi Peng. Continuous variable quantum key distribution based on optical entangled states without signal modulation. September 2011. 45

[62] Matthieu Bloch, Andrew Thangaraj, Steven McLaughlin, and Jean-marc Merolla. LDPC-based secret key agreement over the Gaussian wiretap channel. In *2006 IEEE International Symposium on Information Theory*, pages 1179–1183. IEEE, July 2006. 45

[63] Paul Jouguet, Sébastien Kunz-Jacques, and Anthony Leverrier. Long-distance continuous-variable quantum key distribution with a Gaussian modulation. *Physical Review A*, 84(6), December 2011. 45, 54

[64] M. D. Reid, P. D. Drummond, E. G. Cavalcanti, P. K. Lam, H. A. Bachor, U. L. Andersen, and G. Leuchs. Colloquium: The Einstein-Podolsky-Rosen paradox: From concepts to applications. *Reviews of Modern Physics*, 81(4):1727–1751, December 2009. 46, 50

[65] Michael Wolf, Geza Giedke, and J. Cirac. Extremality of Gaussian Quantum States. *Physical Review Letters*, 96(8), March 2006. 47

[66] Raúl García-Patrón and Nicolas Cerf. Unconditional Optimality of Gaussian Attacks against Continuous-Variable Quantum Key Distribution. *Physical Review Letters*, 97(19), November 2006. 47

[67] Miguel Navascués, Frédéric Grosshans, and Antonio Acín. Optimality of Gaussian Attacks in Continuous-Variable Quantum Cryptography. *Physical Review Letters*, 97(19), November 2006. 47

[68] R. Renner and J. Cirac. de Finetti Representation Theorem for Infinite-Dimensional Quantum Systems and Applications to Quantum Cryptography. *Physical Review Letters*, 102(11), March 2009. 47

[69] Vladyslav C Usenko and Radim Filip. Squeezed-state quantum key distribution upon imperfect reconciliation. *New Journal of Physics*, 13(11):113007, November 2011. 47, 55

[70] Vladyslav C. Usenko and Radim Filip. Feasibility of continuous-variable quantum key distribution with noisy coherent states. *Physical Review A*, 81(2), February 2010. 47, 51

[71] Yujie Shen, Xiang Peng, Jian Yang, and Hong Guo. Continuous-variable quantum key distribution with Gaussian source noise. *Physical Review A*, 83(5), May 2011. 47

[72] F. Grosshans, N. J. Cerf, J. Wenger, R. Tualle-Brouri, and Ph Grangier. Virtual entanglement and reconciliation protocols for quantum cryptography with continuous variables. *Quant. Inform. Comp.*, 3:535–552, 2003. 47

[73] Samuel Braunstein. Squeezing as an irreducible resource. *Physical Review A*, 71(5), May 2005. 47, 50

[74] Paul Jouguet, Sébastien Kunz-Jacques, and Anthony Leverrier. Long-distance continuous-variable quantum key distribution with a Gaussian modulation. *Physical Review A*, 84(6), December 2011. 54, 55

[75] A. B. Klimov, G. Bjork, J. Soderholm, L. S. Madsen, M. Lassen, U. L. Andersen, J. Heersink, R. Dong, Ch. Marquardt, G. Leuchs, and L. L. Sanchez-Soto. Assessing the Polarization of a Quantum Field from Stokes Fluctuation. page 4, April 2010. 61, 68

[76] R. M. A. Azzam and N. M. Bashara. *Ellipsometry and Polarized Light*. Elsevier, Amsterdam, 1987. 61

[77] S. Werner, O. Rudow, C. Mihalcea, and E. Oesterschulze. Cantilever probes with aperture tips for polarization-sensitive scanning near-field optical microscopy. *Applied Physics A: Materials Science & Processing*, 66(7):S367–S370, March 1998. 61

[78] J. R. Schott. *Fundamentals of Polarimetric Remote Sensing*. SPIE Press, 2009. 61

[79] L. D. Barron. *Molecular Light Scattering and Optical Activity*. Cambridge University Press, Cambridge, 2004. 61

[80] Paul Kwiat, Klaus Mattle, Harald Weinfurter, Anton Zeilinger, Alexander Sergienko, and Yanhua Shih. New High-Intensity Source of Polarization-Entangled Photon Pairs. *Physical Review Letters*, 75(24):4337–4341, December 1995. 61

[81] Dik Bouwmeester, JW Pan, and Klaus Mattle. Experimental quantum teleportation. *Nature*, pages 575–579, 1997. 61

[82] A Muller, J Breguet, and N Gisin. Experimental Demonstration of Quantum Cryptography Using Polarized Photons in Optical Fibre over More than 1 km. *Europhysics Letters (EPL)*, 23(6):383–388, August 1993. 61

[83] C.H. Bennett, F. Bessette, G. Brassard, L. Salvail, and J. Smolin. Experimental quantum cryptography. *Journal of Cryptology*, 5(1):3–28, 1992. 61

[84] Natalia Korolkova, Gerd Leuchs, Rodney Loudon, Timothy C. Ralph, and Christine Silberhorn. Polarization squeezing and continuous-variable polarization entanglement. *Physical Review A*, 65(5), April 2002. 62

[85] Hari Prakash and Naresh Chandra. Density Operator of Unpolarized Radiation. *Physical Review A*, 4(2):796–799, August 1971. 62

[86] G. G. Stokes. On the composition and resolution of streams of polarized light from different sources. *Trans. Cambridge Philos Soc.*, 9:399–416, 1852. 62

[87] Warwick P. Bowen, Roman Schnabel, Hans-A. Bachor, and Ping Koy Lam. Polarization Squeezing of Continuous Variable Stokes Parameters. *Physical Review Letters*, 88(9), February 2002. 62, 63

[88] U. FANO. Remarks on the Classical and Quantum-Mechanical Treatment of Partial Polarization. *Journal of the Optical Society of America*, 39(10):859, October 1949. 62

[89] Edward Collett. Stokes Parameters for Quantum Systems. *American Journal of Physics*, 38(5):563, 1970. 62

[90] D.N. Klyshko. Multiphoton interference and polarization effects. *Physics Letters A*, 163(5-6):349–355, March 1992. 62

[91] Daiji Fukuda, Go Fujii, Takayuki Numata, Kuniaki Amemiya, Akio Yoshizawa, Hidemi Tsuchida, Hidetoshi Fujino, Hiroyuki Ishii, Taro Itatani, Shuichiro Inoue, and Tatsuya Zama. Titanium-based transition-edge photon number resolving detector with 98% detection efficiency with index-matched small-gap fiber coupling. *Optics Express*, 19(2):870, January 2011. 64

[92] A. P. Alodjants and S. M. Arakelian. Quantum phase measurements and non-classical polarization states of light. *Journal of Modern Optics*, 46(3):475–507, March 1999. 68

[93] G. Agarwal. Relation between atomic coherent-state representation, state multipoles, and generalized phase-space distributions. *Physical Review A*, 24(6):2889–2896, December 1981. 72

[94] L K Shalm, R B A Adamson, and A M Steinberg. Squeezing and over-squeezing of triphotons. *Nature*, 457(7225):67–70, January 2009. 74

[95] The LIGO Scientific Collaboration (LSC). A gravitational wave observatory operating beyond the quantum shot-noise limit: Squeezed light in application. *arXiv:1109.2295*, 2011. 80

[96] T. J. Kippenberg, R. Holzwarth, and S. A. Diddams. Microresonator-Based Optical Frequency Combs. *Science*, 332(6029):555–559, 2011. 80